Impact of Temperature and Pressure on CO2 Mineral Trapping in Arkosic Reservoir with CaCl2 – type Formation Water

CAO, XU

Impact of Temperature and Pressure on CO_2 Mineral Trapping in Arkosic Reservoir with $CaCl_2$ – type Formation Water

Xu Cao

Department of Earth Sciences

Durham University

Thesis submitted in accordance with the regulations for the degree of Master of Science by Research in Durham University, Department of Earth Sciences, 2020

Xu Cao

Abstract

The feasibility of CO_2 geological storage in arkosic sandstones has been investigated by short-term physical simulation experiments using six sandstones samples from the Eocene sandstone reservoir in the Bonan Subsag, Bohai Bay Basin, East China, under a range of temperature and pressure conditions. The aqueous solution used in the experiment mimics the elemental compositions of the present oilfield formation water. The reservoir sandstone samples were ground to powders prior to the experiment. Amount of 10mL aqueous solution and 2g sandstone powders were fully mixed and assembled in a high pressure, high temperature (HPHT) batch reactor. The experimental temperatures and corresponding pressures were set to 50°C/4 MPa, 100°C/6 MPa and 140°C/9 MPa, respectively. All experiments were carried out for 96 hours. Scanning Electron Microscopy (SEM) and energy dispersive spectroscopy (EDS) analysis of the samples after experiments shows calcite precipitated whilst feldspar partly dissolved. Feldspar dissolution is likely to promote the calcite precipitation by continuously consuming acid in the aqueous solution. To rationalize the mechanism of mineral changes in the experiments, a three-stage chemical reaction process of CO_2 geological storage is proposed. In **Stage Ⅰ**, CO_2 dissolved and saturated in saline aqueous solution due to high pCO_2, producing $CO_{2(aq)}$, H^+, HCO_3^- and CO_3^{2-} for the subsequent reactions. In **Stage Ⅱ** the original calcite cement was dissolved rapidly due to a decreasing pH, while the dissolution rate of ankerite and feldspar remained relatively slow. As acid was consumed in this stage and pH gradually became conducive to calcite reprecipitation. In **Stage Ⅲ**, feldspar continued to be dissolved while calcite and kaolinite precipitated from aqueous solution. Results of Thermal Gravimetric Analysis (TGA) and Scanning Electron Microscopy (SEM) of the experiments indicates that the sample YX981 obtained the greatest amount of carbonates precipitation, which was identified that increased at high temperatures and high content of original silicates minerals, while pressure has no obvious effect on CO_2 mineral trapping. In summary, $Es3^2$ member layer where sample YX981 was collected, was evaluated as a favorable CO_2 mineral trapping site in Bonan Subsag.

Keywords: CO_2 mineral trapping; arkosic sandstone; physical simulation experiments (HPHT).

Declaration

No part of this thesis has been previously submitted for a degree at this or any other institution. The work described here is entirely that of the author, except where reference is made to previously published or unpublished work.

Acknowledgment

Supervisory Team

I would like to appreciate my supervisory team, primarily Prof. Fred Worrall. He was the first supervisor in my academic career. In the past two years, he has given me great help and encouragement. Whether in experimental design or thesis guidance, he has given the most valuable suggestions to keep me on track. Under his careful guidance, I wrote my first English dissertation. I would like to thank Prof. Jon Gluyas for being the second supervisor and for particular help on the side of water-rock interactions. I would like to thank Prof. Andy Aplin for very useful advice on my research plan. I would also like to thank my internal progress reviewers Prof. Chris Greenwell and Prof. Richard Hobbs for the constructive review process.

Technical and Admin staff at Department of Earth Sciences

Thanks Ian Chaplin and Sophie Edwards for help with rock cutting and thin section preparation. Thanks Paula Elliot and Karen Atkinson for helping with experiment cost. Thanks Jo Banner and Louise Bowron for the demonstrating and daily admin.

Friends

I would like to thank Chris Ward for very important guidance in instrument operation. I would like to thank Oluwafemi Aro for useful help in optical microscopic analysis. And I would particularly thank all the friends live in and out Ustinov College, as you are my source of happiness every day.

Scientific Community

Outside of the department I would like to thank Dr. Guanghui Yuan and Nianmin Zan for providing crucial ideas for my thesis writing. I would like to thank Gary Oswald and Ling Song for useful help in minerology analysis.

Family

Finally, I would like to thank my parents for supporting me in all aspects during my master studies. I have always known that no matter what, you will be my strongest backing.

Contents

List of Figures

List of Tables

1. Introduction

Global CO_2 emissions are made up of land-use change and direct anthropogenic CO_2 sources including use of fossil fuels and emissions from industry (IPCC, 2017). The CO_2 sinks comprise a land sink, an atmospheric sink and an ocean sink. The total annual global CO_2 emissions reached about 39.2 Gt in 2017 (Jackson et al., 2017; Peters et al., 2017), whereas the total amount of land and ocean sinks of CO_2 reached about 19.8 Gt in 2017 (Global Carbon Budget 2017; Elmabrouk et al., 2017). The imbalance between source and sink of CO_2 resulted in global surface temperatures increasing of 1.5℃ above pre-industrial levels (IPCC, 2017). Many strategies are needed to control and reduce CO_2 emissions, including enhancement of energy efficiency, energy conservation, usage of clean fuels and substantial development of low-carbon, renewable energy plus further development of nuclear power.

Carbon capture and storage (CCS) is a practical technology to create new and sustainable CO_2 sinks (Gluyas and Mathias, 2013; Leung et al., 2014; Elmabrouk et al., 2017). Geological CO_2 storage is currently considered to be the most viable for the permanent storage of the large quantities of CO_2 (Celia and Nordbotten, 2009; Zwaan and Semkens, 2009; Yang et al., 2010; Myer, 2011). Geological CO_2 storage mainly involves injection of a dense CO_2 phase into depleted oil and gas reservoirs, deep saline aquifers and possibly mined and unmined coal seams (Wigand et al., 2008; Yu et al., 2015, 2017). The geological CO_2 storage potential in depleted oil and gas reservoirs can reach 920 GT in the largest 155 petroleum provinces that encompass 32,000 known oil and gas fields (Klett et al., 1997; Masters et al., 1998; *International Energy Agency Report, 2004*; Stevens et al., 2010). Therefore, injection of CO_2 into depleted oil and gas fields with good sealing conditions, high porosity and permeability has become a major research theme for geological CO_2 storage. At present, studies of CCS are conducted across various scales, from core scales to industrial scales, with methods of physical fluid-rock interactions simulated in batch reactors in the laboratory, numerical simulations, and some industrial projects. Physical simulations in the laboratory were generally conducted on scales of mm to cm using core samples from subsurface reservoirs or mineral grains in a short time (generally several days) (Sorai et al., 2007; Lu et al., 2013; Farquhar et al., 2014; Tutolo et al., 2015). In these laboratory studies, scanning electron microscope (SEM) were used to

identify the change of mineral textures, X-ray diffraction (XRD) to analyze mineral composition changes, and inductively coupled plasma mass spectrometry (ICP-MS) were used to test the fluid composition before and after experiments. Studies using numerical simulation have been conducted on different scales from meters to regional field scales. Of these simulations, many studies of CO_2 injection in saline formations have been done on a small scale assuming a modest injection rate over a limited area (Kumar et al., 2005; Pruess et al., 2003; Taku Ide et al., 2007; Anchliya et al., 2012; Yamamoto and Doughty, 2011; Chasset et al., 2011; Lengler et al., 2010), and a significant amount of simulation studies have been done on a regional scale (Ghomian et al., 2008; Yang, 2008; Nicot, 2008; Person et al., 2010; Birkholzer and Zhou, 2009; Yamamoto et al., 2009; Akinnikawe and Ehlig-Economides, 2016). Besides the physical and numerical simulation studies, there have also been several CCS projects in the field worldwide in the last 20 years. As of today, there are some commercial projects to sequester industrial scale anthropogenic carbon dioxide (Akinnikawe and Ehlig-Economides, 2016) including Weyburn operation in Canada (IEAGHG, 2005); Sleipner west project and Snohvit project in Norway, and in Salah CO_2 injection in Algeria (Eiken et al., 2011).

The geological CO_2 storage mechanisms include: physical trapping (or structural/stratigraphic trapping), residual saturation trapping, solubility trapping and mineral trapping (Bachu et al., 2007; Matter and Kelemen, 2009; Shukla et al. 2010; Li et al., 2016; Li et al., 2018). The physical structural/stratigraphic trapping is the most dominant trapping mechanism. Once injected, the CO_2 that is more buoyant than other liquids will percolate up through the porous rocks until it reaches the top of the formation where it meets and is trapped by an impermeable layer of cap-rock. Residual trapping -the injected CO_2 into the formation displaces fluid as it moves through the porous rock. As the CO_2 continues to move, fluid again replaces it, but some of the CO_2 will be left behind and preserved as disconnected and immobile residual droplets in the pore spaces. Solubility trapping – The CO_2 dissolves into the salt water (or brine) already present in the porous rock its gaseous and supercritical state. The salt water containing CO_2, which is denser than the surrounding fluids will sink to the bottom of the rock formation over time, trapping the CO_2 even more securely. Mineral trapping – the CO_2 dissolves in water to forms a weak carbonic acid which react with minerals in the surrounding rock to form solid carbonate minerals. This process can be rapid or very slow (depending on the chemistry of the rock and water in a specific storage site) but it effectively binds

the CO_2 to the rock. The mineral trapping is the safest and most stable geological CO_2 storage mechanism in the long term (He et al., 2015; Munz et al., 2012; Alia et al., 2015; Yang et al., 2017). These different trapping processes take place over many years at different rates from days to years to thousands of years, but in general, geologically stored CO_2 becomes more securely trapped with time. Mineral trapping, however, can lead to porosity and permeability reduction with the precipitation of carbonate minerals and clays even in short experiments of tens of hours (Tutolo et al, 2015), which may affect the injection and migration process of CO_2 in the reservoirs. Demonstrations of various geological storage of CO_2 are already being carried out in a range of projects of varying scale. However, most research on geological CO_2 storage mechanisms in depleted oil and gas fields are currently focused on physical trapping and solubility trapping (Gilfillan et al., 2009).

Mineral trapping of CO_2 in depleted oil and gas fields is important for permanent storage (Gunter et al., 2000; Kirsch et al., 2014). Mineral trapping of CO_2 primarily refers to reaction of CO_2 to form carbonate minerals including calcite, ferrocalcite, dolomite, ankerite and dawsonite in the subsurface rocks (Li et al., 2009; Li and Pang et al., 2017). In subsurface rocks, the dissolution of aluminosilicate minerals is crucial for the long-term fate of the injected CO_2 because it consumes acidity to produce alkalinity, thereby increasing the saturation index of the carbonate phases, and potentially resulting in a permanent storage of CO_2 in carbonate minerals (Yuan et al, 2019; Bickle, 2009; Wigley et al., 2013). For example, after injection of CO_2 into anorthite-rich clastic rocks, the injected CO_2 reacts with the calcium from anorthite dissolution at low pH to form calcite (Hitchon et al., 1999; Xu et al., 2004; Gilfillan et al., 2009; Matter and Kelemen, 2009; Gaus, 2010; Liu et al., 2011; Munz et al., 2012). Most clastic rocks in depleted oil and gas fields, however, lack calcium-containing minerals. Besides the rock compositions, the water compositions, specifically the cations in the pore water including Ca^{2+}, Mg^{2+}, Na^{+}, K^{+} that are relevant to secondary mineral formation are also key factors for reaction of CO_2 (Gilfillan et al., 2009; Matter and Kelemen, 2009). For example, (i) the presence of a K^{+}-rich solution promotes the precipitation of illite and muscovite, (ii) the presence of a Na^{+}-rich aqueous fluid enables paragonite precipitation, and (iii) the presence of a Ca^{2+} (Mg^{2+})-rich solution may promote the precipitation of carbonate minerals (Yuan et al, 2019; Hangx and Spiers, 2009). The precipitation of dawsonite in subsurface reservoirs is generally

relevant to CO_2 charging relevant to deep hot fluid with high pressure (Hellevant et al, 2013; Li et al, 2016), however, dewsonite was scarely formed in laboratory experiments under CO_2 storage conditions. In addition, the pore space in the rocks also affect capture capability of CO_2. At present there are trials in which CO_2 is injected into igneous rocks and anorthite-rich clastic rocks. The injected CO_2 reacts with divalent cations of Ca^{2+} and Mg^{2+} from dissolution of olivine, pyroxene, and anorthite in igneous rocks to form magnesium/calcium carbonates (Mcgrail et al., 2006; Aradóttir et al., 2011; Kumar et al., 2017; Li and Li et al., 2017; Wolff-Boenisch and Galeczka, 2018). However, the quantity of mineral trapping of CO_2 in igneous rocks is only ever likely to be very small due to small volumes of fractures in such rocks upon which permeability depends (Van Pham et al., 2012).

Previous studies suggested that solubility trapping is the major mechanism of geological CO_2 storage in clastic rocks without calcium-containing minerals like anorthite (Gilfillan et al., 2009; Matter et al., 2009; Hellevang et al. 2014), and carbonate minerals are not likely to occur extensively in these rocks. Whilst Ca^{2+}-bearing silicate minerals are relatively rare in sandstones, pore water chemistry suggests that Ca^{2+}-rich connate brines (pore water) are relatively common in the subsurface reservoirs in petroliferous basins. Therefore, the geological CO_2 storage by mineral trapping in clastic rocks without Ca^{2+}-containing minerals but with Ca^{2+}-rich pore water needs to be further investigated because of the vast pore volume available for storage.

In the oilfields of the Bohai Bay Basin, eastern China, the Eocene sandstone reservoirs are rich in K-feldspar and plagioclase with little anorthite (Li et al., 2009; Yuan et al., 2015a), and the formation waters are rich in $CaCl_2$ (Yuan et al., 2015a, 2015c; Li and Pang et al., 2017). These depleted oil and gas reservoirs with relative high porosity and permeability, and with large amount of geological data in the Eocene layers of the oilfields in eastern China are potentially good locations for study of geological CO_2 storage because they have good seals as they have held oil and gas in the reservoir for millions of years (Li et al., 2016; Yuan et al., 2017a). Thus, six typical Eocene sandstone samples from six different wells in the Bonan Subsag (Fig. 1) were selected to conducted physical CO_2-water-rock interaction simulation experiments with $CaCl_2$ water, under a range of temperature and pressure conditions of 50°C/4 MPa, 100°C/6 MPa and 140°C/9 MPa, respectively. After

experiments, the changes of mineral textures and mineral weights were analyzed using SEM, EDS and TGA, for the purpose of understanding chemical processes of mineral trapping in subsurface feldspar-rich sandstones with $CaCl_2$ formation water and the effects of temperature, pressure and rock composition on the geological CO_2 storage.

2. Geological Setting

The Bohai Bay Basin, an important hydrocarbon-producing province, is located on the eastern coast of China and covers an area of approximately 200, 000 km^2 (Guo et al, 2012; Yuan et al., 2017). It was subdivided into six depressions including the Jizhong, Huanghua, Jiyang, Linqing, Bozhong, and Liaohe depressions by complex tectonic reworking since the late Triassic period (Yuan et al., 2017) (Figure 2.1 A).

The Bonan Subsag, one of the most deeply buried subsags in the Zhanhua Sag, Jiyang Depression, Bohai Bay Basin, covers an area of more than 600 km^2 and is a vital oil production base located in East China. Bonan Subsag (Figure 2.1 B) (Wang et al, 2014). From south to north, the subsag includes the South Gentle Slope Belt, Boshen four Step-fault Zone, Bonan Deep Sag Belt and North Step Slope Belt. The northern part of the Bonan Subsag is separated from the Chengdong Salient by the Chengnan Fault, while the southern part is adjacent to the Chengjiazhuang Salient. The eastern part is next to the Gubei Sag and Gudao Salient near the Guxi Fault, while the western part is bounded by the Yihezhuang Salient (Wang et al, 2014; Liu, 2017*)*.

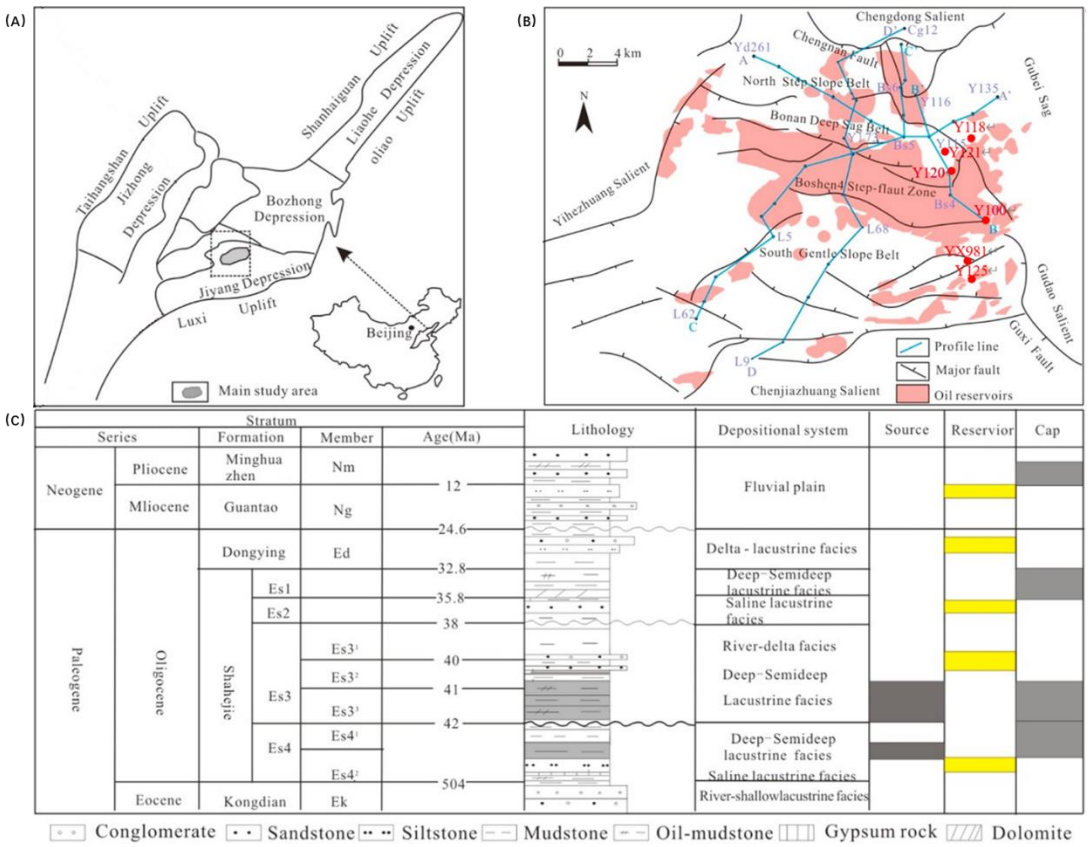

Figure 2.1 - *Bonan Subsag in the Bohai Bay Basin, China. (A) Locationl of the Bonan Subsag. (B) The structural location and tectonic units of the Bonan Subsag. (C) Generalized stratigraphic column for the Bonan Subsag (Liu, 2017).*

The stratigraphy in the Bonan Subsag is made up of Kongdian (Ek), Shahejie (Es), Dongying (Ed), Guantao (Ng), Minhuazhen (Nm) and Pingyuan (Qp) formations from the lower to upper parts. The Eocene Shehejie Formation contains the main source rocks and reservoir rocks in the Bonan Subsag, and is divided into four members, Es1, Es2, Es3 and Es4 (from top to base) (Figure 2.1 C; Figure 2.2).

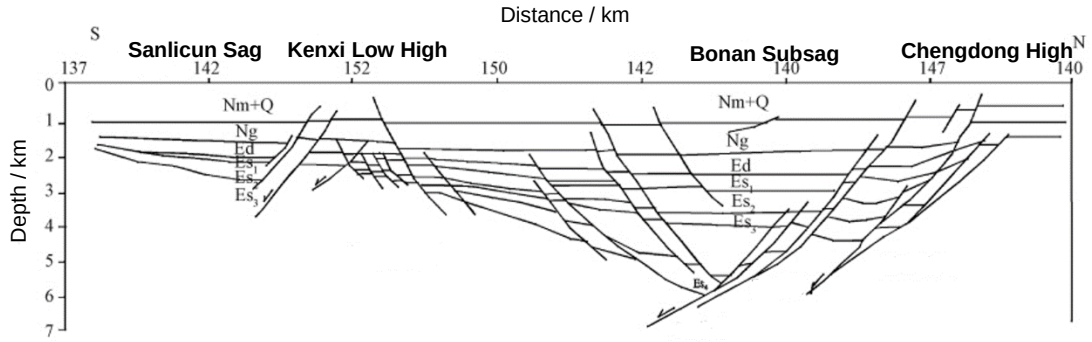

Figure 2.2 - *Profile along N-S-trending seismic section 627.4 in Bonan Subsag (Li, 2010).*

The thickness of Es4 is between 100 and 1300 m and mainly consists of terrigenous clastic rocks. Carbonate rocks and gypsum are also common, the carbonates being mixed with clastic sediments such as mud and sand. It was deposited in a semi-enclosed saline lacustrine setting (Wang et al 2015). Thick sequences of mudstones, shales, sandstones and conglomerates were deposited in the third member (Es3) during the early to middle stage of the lake basin development (Wang et al., 2005), as deep fresh water lake sediments (Wang et al 2015). The thickness of Es3 is between 100 and 1500 m, and Es3 is further divided into three sub-members.

The main objects of this study are the porous sandstones deposited in the Es3 member layers. During the strong rifting period when the third member of Shahejie Formation was deposited, the accommodation space increased rapidly, and the lake became relatively deep, resulting in rapid deposition near the sediment source, forming a deep lake turbidite fan with a short transport distance (Zeng et al, 2019). The turbidite fan can be divided into upper-fan, middle-fan and lower-fan.

According to core and log data, the study area is in the middle-fan, which can be divided into three microfacies-turbidite channel, floodplain and channel-overflow (Zeng et al, 2019). The turbidite channel is mainly composed of massive gravelly sandstone, pebbled sandstone, coarse sandstone and medium sandstone. The floodplain is mainly composed of shale, mudstone, siltstone and argillaceous siltstone. The channel-overflows are primarily composed of fine sandstone and siltstone (Zeng et al, 2019). The sandstones in the turbidite channel are dominated by lithic feldsarenite and arkosic litharenite. The feldspars are mainly K-feldspar and plagioclase without anorthite. Carbonate cements, quartz overgrowth and kaolinite are the main authigenic minerals in the sandstones. The porosity of the reservoir is from 13% to 22%, with an average of 16.1%. The air permeability of the reservoir is from 5 md to 64 md, with an average of 26.5 md (Zeng et al, 2019). These relative high poroperm data and the presence of carbonate cements suggest these reservoirs to be potential good site for geological CO_2 storage.

The present-day formation temperature is approximately 150°C at 4000 m and approximately 80°C at 2000 m (Wang, 2010; Guo et al., 2012), with formation temperature gradient of approximately 35 °C/km. The development of the high formation temperature gradient in the Bohai Bay Basin was probably relevant to the extensive tectonic movement from the Mesozoic to the Neogene Periods (Li et al., 2013). The tested formation pressure and the natural gas composition suggest that the pCO_2 in hydrocarbon reservoirs ranges from 0.25 MPa at 2000m to 4.05 MPa at 4000m (Yuan et al., 2015a). The formation water is highly saline with high concentration of Ca^{2+}, Mg^{2+}, K^+, Na^+ (Yuan et al., 2015a and 2015b).

Compared with the reservoirs in Erdos Basin, where the first CCS project was conducted in China, the reservoir in the Bonan Subsag, Bohai Bay Basin was richer in feldspar (25.0% for Erdos and 31.8% for Bonan, average content) (Wang et al., 2013). Therefore, Bonan Subsag has potential to be selected for research on geological storage in arkosic reservoir. Six samples of arkosic sandstone reservoir were collected from six different wells in the Bonan Subag, Bohai Bay Basin, East China (Table 2.1). Well Y118, well Y121 and well Y120 are all located in the northeast of Boshen four Step-fault Zone, while well Y100, well Y125 and well YX981 are all located in the southeast of Boshen four Step-fault Zone. To obtain samples rich in feldspar, samples selected in this study were

all from Es3 member deeper than 2500 m. All six samples were cut from cores provided by Shengli Oilfield and stored in dry dark space.

Table 2.1-*Well, depth and member of samples.*

WELL	DEPTH, M	MEMBER
Y118	3346.50	$Es3^{2}$
Y120	3360.04	$Es3^{3}$
Y100	2712.10	$Es3^{2}$
YX981	2726.10	$Es3^{2}$
Y125	2544.40	$Es3^{3}$
Y121	3143.00	$Es3^{1}$

3. Methodology

3.1 Sample preparation and storage

Six samples of arkosic sandstone reservoir were collected from six different wells in the Bonan Subag, Bohai Bay Basin, East China (Table 2.1). For following physical simulation experiments and analysis of scanning electron microscope (SEM) and thermogravimetric analysis (TGA), six rock samples were ground to powder by an annular gap-type ball mill, then being transferred into plastic bags for uncontaminated and dry storage. To increase the reaction rate in a following physical simulation (Yuan et al, 2015; Yuan et al, 2017; Steefel et al, 2015), samples were ground to acquire reactive surface area (Equation 3.1; Equation 3.2).

$$R_m = A_m a_{H+}^n k(1 - Q/K_m) \quad \text{Equation 3.1}$$

$$R_m = A_m a_{H+} k[f\Delta G_r] \quad \text{Equation 3.2}$$

A_m - bulk reactive surface area (m^2 mineral/m^3 porous medium);

k - rate constant,

a_{H^+} - activity of H^+, n - pH dependence of the reaction;

Q - ion activity product;

K_m - equilibrium constant (Steefel and Lasaga, 1994; Steefel et al., 2015).

Polished casting thin sections were made from original rock samples, for optical microscopy observation and compositional counting.

3.2 Optical microscopy

To identify the microscopic characteristic of the six sandstone reservoir samples, optical microscopy observation was carried out using a binocular polarizing microscope whose magnification was up to 20x. Following compositions were identified: quartz, K-feldspar, plagioclase, rock fragment, clay minerals, micas, siliceous and carbonate cement and pores. For each sample, photomicrographs were viewed and taken by a computer-driven camera.

3.3 Scanning electron microscopy and energy dispersive spectroscopy (SEM-EDS)

SEM-EDS methods were applied to compare morphology features and mineral constituent of unreacted sample powder with reacted ones. Images of feldspar dissolution before and after physical simulation experiments were captured on a Hitachi SU-70 FEG SEM, a scanning electron microscope with energy dispersive spectroscopy (SEM-EDS). Secondary electron images (SE) provided analysis of mineral surface topography, while backscattered imaging was used to distinguish pores from grains. By the use of Oxford Instruments EDX system (X-MaxN 50 Silicon Drift Detector), the main chemical constitution elements of minerals were detected for minerals identification.

For the SEM analysis, the rock samples were prepared into two forms, two cm diameter pieces and rock powder. To eliminate heterogeneity, rock powder was evenly mixed before SEM. The rock pieces were carbon-coated, while the rock powder was held in a transparent glass container before carbon coating. Then the sample was placed onto an electric carbon strip on a sample mount before being sent into the vacuum chamber. Images were produced at magnification between 400x – 8000x. Microanalysis for identification of elements within minerals was run by the attached EDS system. Each target mineral was tested twice by an EDX system. To avoid interference from adjacent minerals, every data points of elements constitution were obtained from the centre of target mineral.

Quantitative compositional analysis of all six samples (Y100, Y118, Y120, Y121, Y125 and YX981) was conducted by AMICS (Advanced Mineral Identification and Characterization System) on ZEISS Crossbeam 550 FIB-SEM before physical simulation experiments. The materials used were two cm diameter, thin sections of each sample. On each thin section before scanning, an eight milimetre * seven milimetre rectangular area where minerals are evenly distributed was designated. After analyzing the scanning spectrum, contents of sample compositions were obtained.

3.4 X-ray diffraction (XRD)

XRD was performed to identify the mineral composition of the rock samples before and after reactions. For preparation, a thin layer of Vaseline was spread on a 1 mm deep resin disc with a radius of 1.25 mm for sticking before powdered sample was pressed into it. The upper surface of

powder was evened to preserve a smooth surface for diffractions. To eliminate heterogeneity, rock powder was evenly mixed before XRD. After preparation slides were placed onto the sample holder. Each powdered sample was analyzed by a Bruker D8 Advance diffractometer. Minerals analyzed for were: quartz, feldspar, carbonate and clay minerals. Specific types of clay minerals have not been analyzed, as their primary peaks were often between 2 and 20° 2θ while the minimum 2θ available for this instrument is 5°. Diffraction patterns were set as CuKα radiation (λ=1.5406 Å) and for removal of CuKβ a nickel filter was used. A scanning rate was set as 3°/min, under 40 kV, 200 mA, and angle scaled from 5-90° 2θ, step at each 0.02. After diffraction data was transferred into Jade 6.0 software for qualitative analysis. The reference standard is SY/T 5163-2018 Analysis method for clay minerals and ordinary non-clay minerals in sedimentary rocks by the X-ray diffraction, released by the National Energy Administration, China.

3.5 Thermogravimetric analysis (TGA)

TGA was applied to measure the amount of carbonate within samples before and after the experiments. Approximately, 100 mg of rock powder was filled into a crucible, then heated in a high mass thermogravimetric analyzer (1200 iSeries analyzer) under a N_2 atmosphere (flow 30 cc/min), from 25-900 °C, at a rate of 20 °C/min. Before TGA, rock powder was dried at 80 °C for 48 hours to exclude the impact on weight loss led by moisture evaporation as much as possible. To eliminate heterogeneity, rock powder was evenly mixed before TGA. Both recorded weight loss and the first derivative of the weight loss were analyzed by Infinity Pro Software before further data analysis. Weight loss was represented by percentage. For comparison and control, curves of the same samples reacted under different conditions were compared in one graph.

The reason for the weight loss in specific temperature was the decomposition of characteristic minerals or organic material at that specific temperature. But this feature could not be utilized on its own for mineral identification because it is possible that more than one type of mineral can decompose within the same temperature window. Generally, the weight loss below 200 °C can be attributed to loss of moisture; loss of interlayer water from clay minerals; or decomposition of certain minerals, for instance, dawsonite (actually not observed through microscopy). Then kerogen decomposes between 200-600 °C, where clays minerals, for instance, kaolinite and smectite, also

lose structural water. The weight loss within 600-900 °C temperature range was caused by loss of CO_2 produced from the carbonate minerals decomposition (Wang et al., 2009). For the CO_2 mineral trapping research, results from temperature range of 600-900 °C, i.e. where carbonate mineral decomposed, was the focus. Though quartz and feldspar are predominant mineral phases, they cannot be analyzed through TGA. Different reasons of weight loss above are indicated in Table 3.1.

Table 3.1-*Typical temperature range for mineral decomposition by thermogravimetric analysis (Wang et al., 2009).*

Temperature range	Attribution
25-200 °C	Moisture and interlayer water
200-600 °C	Decomposition of kerogen Dehydroxylation of clay minerals
600-900 °C	Decomposition of carbonate minerals

Every sample was replicated to eliminate error. To calibrate results from TGA, arithmetic average deviations of both originals and replications were calculated. For example, as the result of sample *Y100* and its replication each contained 2527 data recording points by TGA, the formula to average the arithmetic average deviation of every data point value is shown as Equation 3.1. Result of $\overline{\Delta x}$ of *Y100* is calculated to be 0.034%. Such a tiny deviation indicates good reliability of TGA data.

$$\overline{\Delta x} = \frac{\sum_{n=1}^{2527}\left(\frac{|x_{n1}-\overline{x_n}|+|x_{n2}-\overline{x_n}|}{2}\right)}{2527} \qquad \text{Equation 3.1}$$

As predominant minerals (quartz, feldspar) cannot be decomposed in TGA analysis, a correlation focused on % mass of carbonates of unreacted samples obtained by FIB AMICS vs % losses of carbonates from temperature range of 600-900 °C through TGA was tested by *CORREL function*. The equation for the correlation coefficient is:

$$Correl(X,Y) = \frac{\sum(x-\bar{x})(y-\bar{y})}{\sqrt{\sum(x-\bar{x})^2\sum(y-\bar{y})^2}} \qquad \text{Equation 3.2}$$

where $\bar{x}$ and $\bar{y}$ are the sample means AVERAGE(FIB) and AVERAGE(TGA) (Table 3.3). The value of correlation coefficient was calculated to be 0.9882 and thus TGA carbonates losses observed in Durham were deemed reliable.

Table 3.2-*% mass of carbonates of unreacted samples obtained by FIB AMICS and % losses of carbonates from temperature range of 600-900 °C through TGA.*

Sample	TGA	FIB
Y100	1.22	0.82
Y118	1.41	1.59
Y120	2.65	5.46
Y121	7.49	12.4
Y125	1.02	1.21
YX981	0.45	0.01

3.6 Physical simulation experiments

For comparison of CO_2 storage effectiveness in arkosic sandstone reservoirs under different conditions, nine groups of physical simulation experiments were conducted (Figure 3.1). To simulate geological conditions, samples were reacted in an almost closed system for the same duration but under different temperature and pressure conditions (Table 3.3). Three different temperature condition were applied and the buried depths corresponding to 50℃, 100℃, and 140℃ are approximately 1000 m, 2500 m and 3500 m respectively. Depth from 2500 m to 3500 m is where original reservoirs of six samples locate, and the temperature condition of 50℃ was applied to explore the effectiveness of CO_2 mineral trapping with low temperature, and its differences compared with higher temperature. Three different designed pressure conditions 4 MPa, 6 MPa, 9 MPa were selected to analyze the impact of pressure on CO_2 mineral storage, and the pressure were fixed according the CO_2 partial pressure pCO_2 in natural oil-gas reservoirs (Smith, 1989), which was actually much lower than the formation pressure. The highest pressure, 9 MPa, was applied to create the supercritical condition for investigating the impact of supercritical CO_2 on mineral trapping.

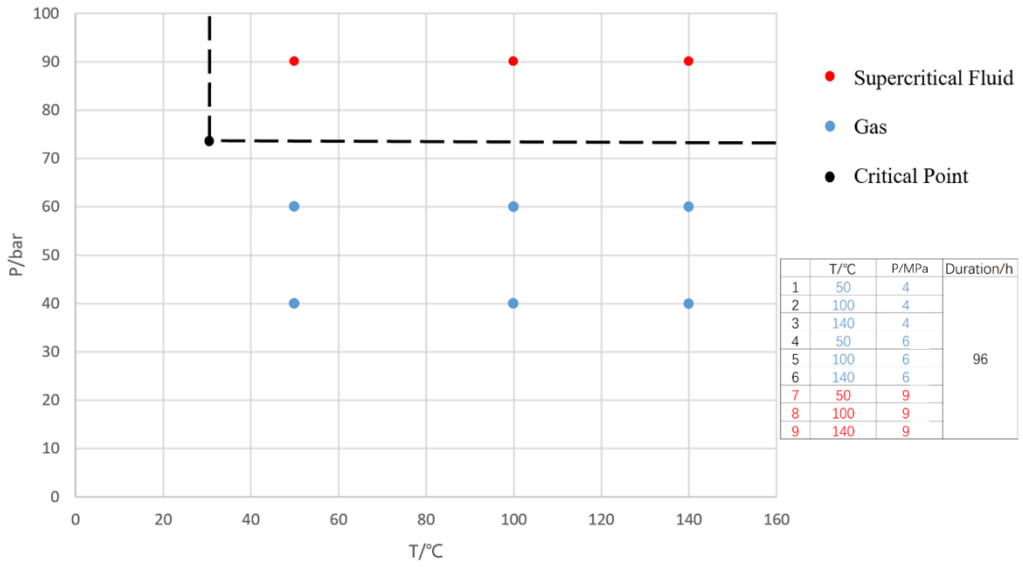

Figure 3.1 - *Physical simulation experiment conditions.*

Experimental apparatus consisted of a high pressure/temperature resistant stainless-steel alloy reactor (rated up to 20 MPa and 225°C); temperature system (heat, control and sensor); and pressure system (deliver, control and sensor). Temperature and pressure were produced by the 4760 Parr 5L external pressure vessel and temperature controller, connected to a Thar CO_2 delivery system, which could pump liquid CO_2 into the reaction chamber containing samples, in which case the pressure that the instrument provided was generally equal to CO_2 partial pressure. Then reaction held for a set amount of time. At the end of the reaction time the reaction vessel was depressurized and samples recovered.

Within each experiment of the nine pressure and temperature conditions all six samples of the arkosic reservoir were considered - leading to 54 experiments. The control for these experiments were the analyses of the unreacted samples, thus giving 60 sets of analyses that allow for the comparison of reacted with unreacted rock samples. For each rock sample approximately two grams of each powdered sample which was evenly mixed were put into a test tube with about 10 mL solution within each. The recipe of solution used in the experiments was from Ca^{2+}-rich formation water in Bohai Bay (Table 3.4). Among all the formation water data provided by Shengli Oilfield, the recipe shown in Table 3.4 was the formula with the highest calcium content.

Table 3.3 – *Classification of samples used in this study.*

Y100	Y100-Unreacted		Y121	Y121-Unreacted	
	Y100-50℃	Y100-50℃-4 MPa		Y121-50℃	Y121-50℃-4 MPa
		Y100-50℃-6 MPa			Y121-50℃-6 MPa
		Y100-50℃-9 MPa			Y121-50℃-9 MPa
	Y100-100℃	Y100-100℃-4 MPa		Y121-100℃	Y121-100℃-4 MPa
		Y100-100℃-6 MPa			Y121-100℃-6 MPa
		Y100-100℃-9 MPa			Y121-100℃-9 MPa
	Y100-140℃	Y100-140℃-4 MPa		Y121-140℃	Y121-140℃-4 MPa
		Y100-140℃-6 MPa			Y121-140℃-6 MPa
		Y100-140℃-9 MPa			Y121-140℃-9 MPa
Y118	Y118-Unreacted		Y125	Y125-Unreacted	
	Y118-50℃	Y118-50℃-4 MPa		Y125-50℃	Y125-50℃-4 MPa
		Y118-50℃-6 MPa			Y125-50℃-6 MPa
		Y118-50℃-9 MPa			Y125-50℃-9 MPa
	Y118-100℃	Y118-100℃-4 MPa		Y125-100℃	Y125-100℃-4 MPa
		Y118-100℃-6 MPa			Y125-100℃-6 MPa
		Y118-100℃-9 MPa			Y125-100℃-9 MPa
	Y118-140℃	Y118-140℃-4 MPa		Y125-140℃	Y125-140℃-4 MPa
		Y118-140℃-6 MPa			Y125-140℃-6 MPa
		Y118-140℃-9 MPa			Y125-140℃-9 MPa
Y120	Y120-Unreacted		YX981	YX981-Unreacted	
	Y120-50℃	Y120-50℃-4 MPa		YX981-50℃	YX981-50℃-4 MPa
		Y120-50℃-6 MPa			YX981-50℃-6 MPa
		Y120-50℃-9 MPa			YX981-50℃-9 MPa
	Y120-100℃	Y120-100℃-4 MPa		YX981-100℃	YX981-100℃-4 MPa
		Y120-100℃-6 MPa			YX981-100℃-6 MPa
		Y120-100℃-9 MPa			YX981-100℃-9 MPa
	Y120-140℃	Y120-140℃-4 MPa		YX981-140℃	YX981-140℃-4 MPa
		Y120-140℃-6 MPa			YX981-140℃-6 MPa
		Y120-140℃-9 MPa			YX981-140℃-9 MPa

Table 3.4 - *Chemical composition of experiment solution.*

Water Type: $CaCl_2$		Mass Concentration: 40777.19 ppm			
Solute	$NaHCO_3$	NaCl	$MgCl_2$	$CaCl_2$	TDS
Mass(mg)	448.92	10132.6	510.63	2500.28	13592.4
Ion	Na^+	Ca^{2+}	Mg^{2+}	HCO_3^-	Cl^-
Concentration (ppm)	12320.05	2702.75	387.07	978.05	24389.27

Before the start of each experiment, the temperature of the reaction vessel was autotuned for one day. Once the expected temperature was reached, a beaker contained six test tubes, one for each rock sample, was placed onto the bottom of the reaction vessel; the reaction vessel sealed; and liquid CO_2 pumped into the reaction chamber for designed pressure. Before closing the valve of cylinder, continuing pumping for 5 minutes to exhaust air even after the indication of the pressure gauge reached the design pressure. Back pressure regulator was started at the same time to ensure control of the pressure of the duration of the experiment. Each group of experiments was held for 96 hours. After four days, reacted samples were then taken out after depressurization and dried for SEM, XRD and TGA. Due to the large sample size and time constraint, experiment design did not include duration as a variable.

3.7 Statistical analysis

Four factors were tested in the experiments. The experiment described above was developed as a complete factorial experiment with respect to three experimental conditions. The factors and their levels are summarized in Table 3.5. For example, Factor *Sample* represented six samples used in physical simulation experiments, namely *Y118, Y120, Y100, YX981, Y125* and *Y121*. Factor *Temperature* represented three temperatures used in physical simulation experiments, namely *50 ℃, 100 ℃* and *140 ℃*. Factor *Pressure* represented three pressures used in physical simulation experiments, namely *4 MPa, 6 MPa* and *9 MPa*. Factor *Temprange* represented eight temperature ranges from 500 ℃ to 900 ℃ in TGA, namely *500-550 ℃, 550-600 ℃, 600-650 ℃, 650-700 ℃, 700-750 ℃, 750-800 ℃, 800-850 ℃, 850-900 ℃*.

Table 3.5 - *Factors tested in the model and the number of levels used.*

	Factor	# of levels	level values
A	Sample	6	Y118, Y120, Y100, YX981, Y125, Y121
B	Temperature	3	50, 100, 140 (℃)
C	Pressure	3	4, 6, 9 (MPa)
D	Temprange	8	500-550, 550-600, 600-650, 650-700, 700-750, 750-800, 800-850, 850-900 (℃)

Minitab 18 was used for statistical analysis of the TGA data. The statistical method used to identify

and confirm the impact of factors within the data was analysis of variance (ANOVA). ANOVA could be used to separate any variation of the defined response caused by altering the controlled factors from the variation caused by random errors. In this case, the responses were defined for *wt%*, i.e. percentage of weight loss of some combination among four factors, and *diff*, i.e. difference between wt% of reacted sample with its respective unreacted sample. By testing whether changing the controlled factors resulted in significant difference, ANOVA could present objective and effective conclusions based on the validity of the physical simulation experiments (Miller and Miller, 2010).

Before using ANOVA the normality of data was tested. The Anderson-Darling test, abbreviated to AD, was used for testing whether a normal distribution adequately describes a set of data (Stephens, 1974). The smaller the value of the AD statistic the closer the distribution of data was to the target distribution and then the more valid the ANOVA was. To assess for non-normality due to the presence of outliers the Q-Q plot was plotted. If necessary, the data were log-transformed and re-tested – it did not prove necessary to use other transformations. In removing outliers never more than 5% of the original data were removed. However, it should be noted that ANOVA is robust against its assumption of data normality. Within the design it was possible to also consider up to four-way interactions but no covariates were considered.

In the ANOVA, the level of significance used was 95 %, indicating that there was a 95% probability that the factor or interaction was not zero. The fit of the model was assessed using R^2 which shows the percentage of data which could be explained by the model. The magnitude of the effects of each significant factor and interaction was calculated using the generalised ω^2 (Olejnik and Algina, 2003) and values were presented as least-square means (otherwise known as marginal means). *Post hoc* assessment of factors and interactions was carried out using the Tukey test. After *Post hoc* assessment, interaction plots were performed to show how the relationship between one categorical factor and a continuous response depends on the value of the second categorical factor. Interaction plot display means for the levels of one factor on the x-axis and a separate line for each level of another factor. Parallel lines indicate that no interaction occurs, while nonparallel lines indicate an interaction occurs. The more nonparallel the lines are, the greater the strength of the interaction.

4. Results

4.1 Lithofacies

Based on 95m cores from ten wells in the Bonan subsag, the rocks in the turbidite fan sediments were divided into six lithofacies (Figure. 4.1) including some pebbly sandstones and coarse sandstones, mainly medium sandstones and fine-grained sandstones, siltstones-shaly sandstones and mudstones. Pebbly sandstones and coarse sandstones account for less than 20% of the sandstone rocks; medium sandstone and fine-grained sandstones, with an account of approximately 60%, dominating the sandstone rocks; siltstones-shaly sandstones account for the left 20% sandstone rocks. The six samples used for physical CO_2-water-rock interaction simulation in this study were selected mainly from medium sandstones, fine-grained sandstones, and shaly sandstones.

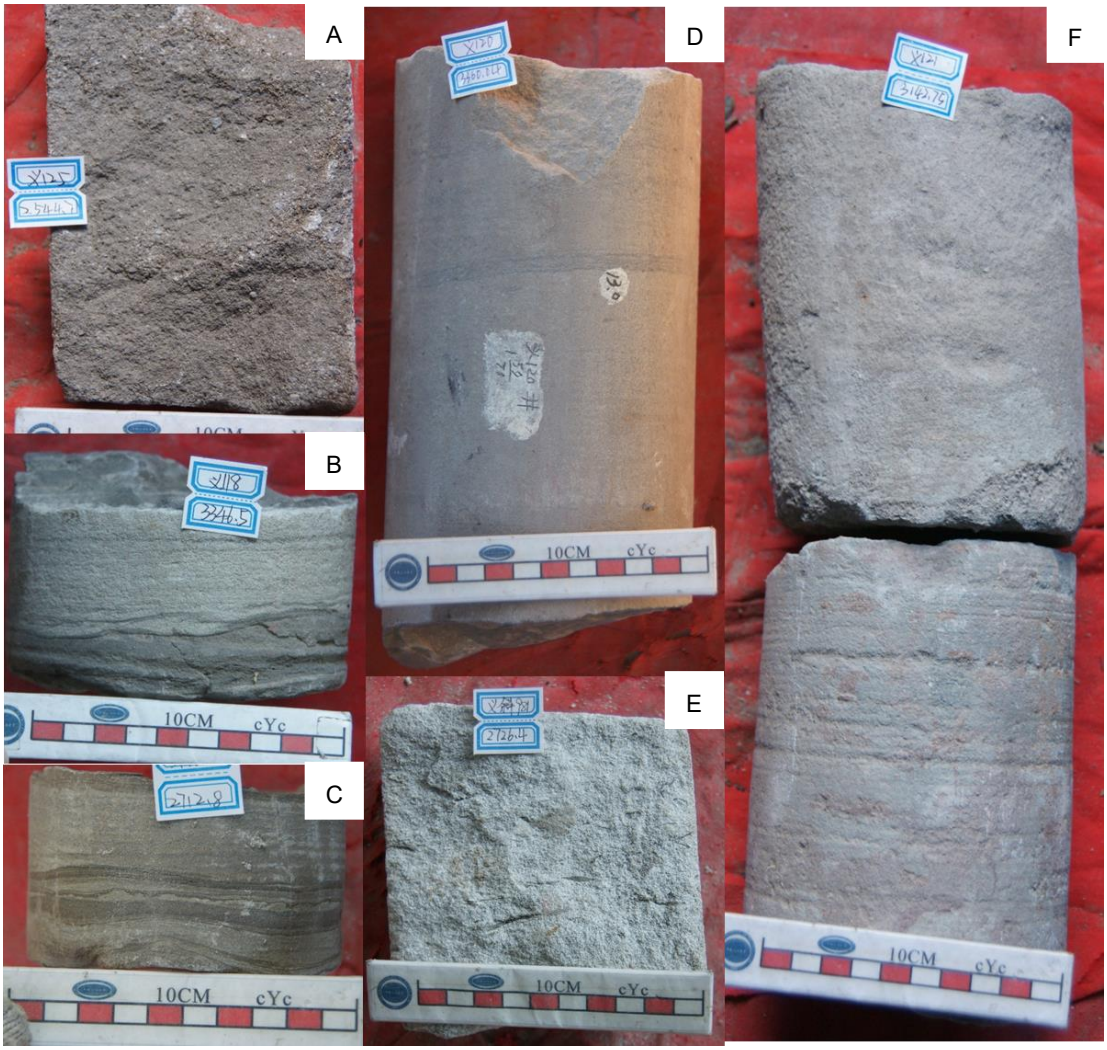

Figure 4.1 - *Different lithofacies in the Es3 turbidites in the Bonan Subsag, Jiyang Depression,*

Bohai Bay Basin. A-Y125, B-Y118, C-Y100, D-Y120, E-YX981, F-Y121.

4.2 Petrography

The rock phases of Es3 member, Bonan Subsag were dominated by lithic arkose and arkose, with a small quantity of feldspathic litharenite and litharenite (Figure 4.2). Data of mineral composition shows that the sandstones in the $Es3^2$ members are rich in K-feldspar and plagioclase (Table 4.1). K-feldspar content was 9 - 40% with an average of 16.1%. Plagioclase content is 10 - 40% with an average of 15.7%, only 0.4% lower than K-feldspar. Quartz content was 15 - 70% with an average of 47.2%. Rock Fragment content was 1 - 76% with an average of 21.0%. Among them, the metamorphic lithic content was the highest, generally 2 - 74%, with an average of 15.1%. Following is igneous lithic content, from 0.5% to 17%, with an average of 5.6%. The sedimentary lithic content was the lowest, generally from 0.5% to 15%, with an average of 2.3%. Sandstones in the $Es3^2$ had low compositional maturity, with an average of 0.886.

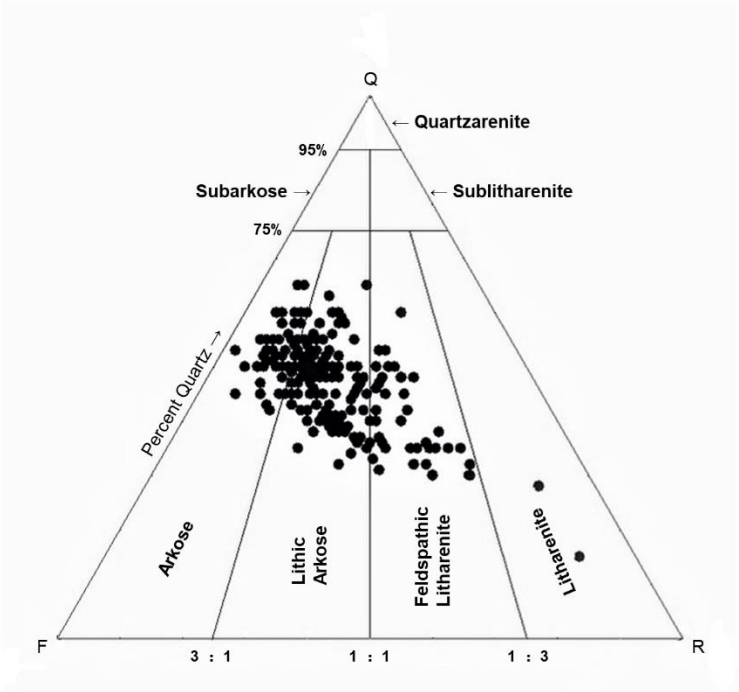

Figure 4.2 – *Ternary plot of sandstones composition in the $Es3^2$ members, Bonan Subsag (Folk classification scheme).*

Table 4.1 - *Mineral composition of the sandstones in the Es3[2] members, Bonan Subsag. Data from 30 wells were collected from Exploration and Development Research Institute, Shengli Oilfield, Sinopec, China.*

Content/%	Quartz	Feldspar	K-Feldspar	Plagioclase	Lithic
Average	47.2	31.8	16.1	15.7	21.0
MAX	70	80	40	40	76
MIN	15	9	9	10	1
Content/%	**Igneous**	**Metamorphic**	**Sedimentary**	**Matrix**	**Cement**
Average	5.6	15.1	2.3	8.7	4.8
MAX	17	74	15	40	40
MIN	0.5	2	0.5	0	0

With the combination of both microscopy and quantitative compositional analysis, the two most common phenomena observed were extensive feldspar dissolution (except sample *Y121*) and carbonate cementation (except sample *YX981*). All six sandstones samples contained K-feldspar and plagioclase (almost all albite), with an average content (after pores removed) of 12.87% and 19.58%, respectively (Table 4.2). The surface porosity of thin section samples in decreasing order were: *Y125* (26.86%), *Y100* (20.18%), *YX981*(16.12%), *Y120* (16.12%), *Y118* (8.97%), *Y121* (5.39%). As the material for physical simulation experiments was rock powder in which case that the rock structures were eliminated, content of sample composition without pores were calculated to reflect the real situation of material composition in physical simulation experiments. Grain size of each sample was estimated visually by microscopy. Samples in decreasing order of grain size were: *Y125* (0.26 mm), *YX981* (0.21 mm), *Y120* (0.20 mm), *Y121* (0.19 mm), *Y100* (0.17 mm), *Y118* (0.12 mm).

Table 4.2 - *Specific mineral composition of sample Y100, Y118, Y120, Y121, Y125 and YX981. Data was obtained by FIB AMICS (Advanced Mineral Identification and Characterization System).*

Sample	*Y100*			*Y118*			*Y120*		
Compositions	**% Mass**	**% Area**	**% Area (no pores)**	**% Mass**	**% Area**	**% Area (no pores)**	**% Mass**	**% Area**	**% Area (no pores)**
Silicas	**49.27**	**39.52**	**49.51**	**43.11**	**39.79**	**43.71**	**44.59**	**37.92**	**45.32**
Quartz	49.27	39.52	49.51	43.11	39.79	43.71	44.59	37.92	45.32
Feldspars	**34.14**	**27.86**	**34.90**	**33.27**	**30.98**	**34.03**	**33.62**	**28.96**	**34.61**
Plagioclase	18.53	14.87	18.63	25.57	23.60	25.93	22.32	18.98	22.68
K-Feldspar	15.61	12.99	16.27	7.69	7.38	8.11	11.30	9.98	11.93
Micas	**5.12**	**3.58**	**4.48**	**15.04**	**12.78**	**14.04**	**7.54**	**5.93**	**7.09**
Biotite	3.59	2.44	3.06	1.55	1.21	1.33	0.41	0.30	0.36
Muscovite	1.53	1.14	1.43	13.49	11.57	12.71	7.13	5.63	6.73
Clays	**9.84**	**7.86**	**9.85**	**6.57**	**5.95**	**6.54**	**7.84**	**6.31**	**7.54**
Kaolinite	4.91	4.13	5.17	4.66	4.51	4.95	1.46	1.30	1.55
Chlorite	0.38	0.25	0.31	1.91	1.44	1.58	1.37	0.95	1.14
Illite	4.55	3.48	4.36	0.00	0.00	0.00	5.01	4.06	4.85
Carbonates	**0.82**	**0.59**	**0.74**	**1.59**	**1.26**	**1.38**	**5.46**	**4.00**	**4.78**
Calcite	0.24	0.19	0.24	0.03	0.03	0.03	0.01	0.01	0.01
Dolomite	0.01	0.01	0.01	0.01	0.01	0.01	0.03	0.03	0.04
Ankerite	0.57	0.39	0.49	1.55	1.22	1.34	5.42	3.96	4.73
Others	**0.81**	**0.42**	**0.53**	**0.42**	**0.27**	**0.30**	**0.95**	**0.56**	**0.67**
Pores	**/**	**20.18**	**/**	**/**	**8.97**	**/**	**/**	**16.12**	**/**
Sample	*Y121*			*Y125*			*YX981*		
Compositions	**% Mass**	**% Area**	**% Area (no pores)**	**% Mass**	**% Area**	**% Area (no pores)**	**% Mass**	**% Area**	**% Area (no pores)**
Silicas	**34.55**	**34.28**	**36.23**	**60.34**	**44.15**	**60.36**	**48.27**	**40.66**	**48.48**
Quartz	34.55	34.28	36.23	60.34	44.15	60.36	48.27	40.66	48.48
Feldspars	**27.23**	**27.39**	**28.95**	**28.83**	**21.53**	**29.43**	**32.10**	**27.49**	**32.78**
Plagioclase	17.43	17.27	18.25	13.74	10.06	13.75	18.16	15.29	18.23
K-Feldspar	9.81	10.12	10.70	15.08	11.47	15.68	13.93	12.20	14.55
Micas	**16.49**	**14.92**	**15.77**	**1.24**	**0.84**	**1.15**	**2.37**	**1.81**	**2.16**
Biotite	3.49	2.94	3.11	0.11	0.07	0.10	0.76	0.55	0.66
Muscovite	12.99	11.97	12.66	1.14	0.77	1.05	1.61	1.26	1.50
Clays	**0.74**	**0.69**	**0.73**	**7.04**	**5.26**	**7.19**	**16.44**	**13.42**	**16.00**
Kaolinite	0.41	0.43	0.45	5.16	3.96	5.41	6.44	5.69	6.78
Chlorite	0.33	0.26	0.28	0.02	0.01	0.01	2.57	1.77	2.11
Illite	0.00	0.00	0.00	1.85	1.29	1.76	7.43	5.96	7.11
Carbonates	**12.40**	**10.59**	**11.20**	**1.21**	**0.79**	**1.08**	**0.01**	**0.00**	**0.00**
Calcite	0.17	0.16	0.17	0.36	0.26	0.36	0.01	0.00	0.00
Dolomite	0.38	0.35	0.37	0.02	0.01	0.01	0.00	0.00	0.00
Ankerite	11.85	10.09	10.66	0.83	0.52	0.71	0.00	0.00	0.00
Others	**8.59**	**6.75**	**7.13**	**1.35**	**0.58**	**0.79**	**0.82**	**0.49**	**0.58**
Pores	**/**	**5.39**	**/**	**/**	**26.86**	**/**	**/**	**16.12**	**/**

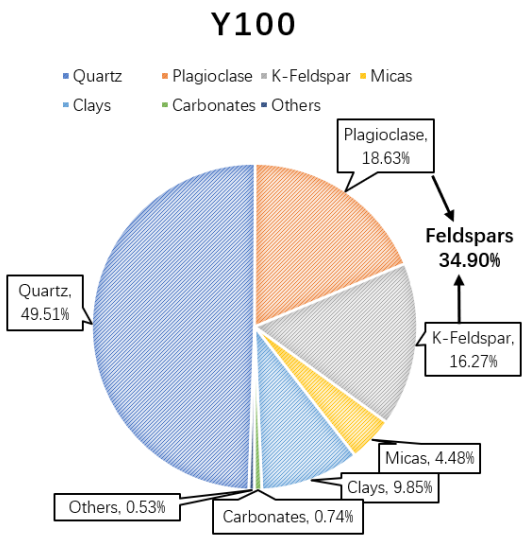

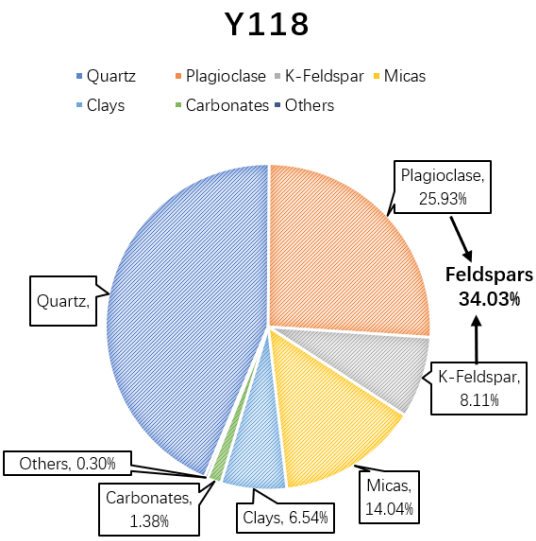

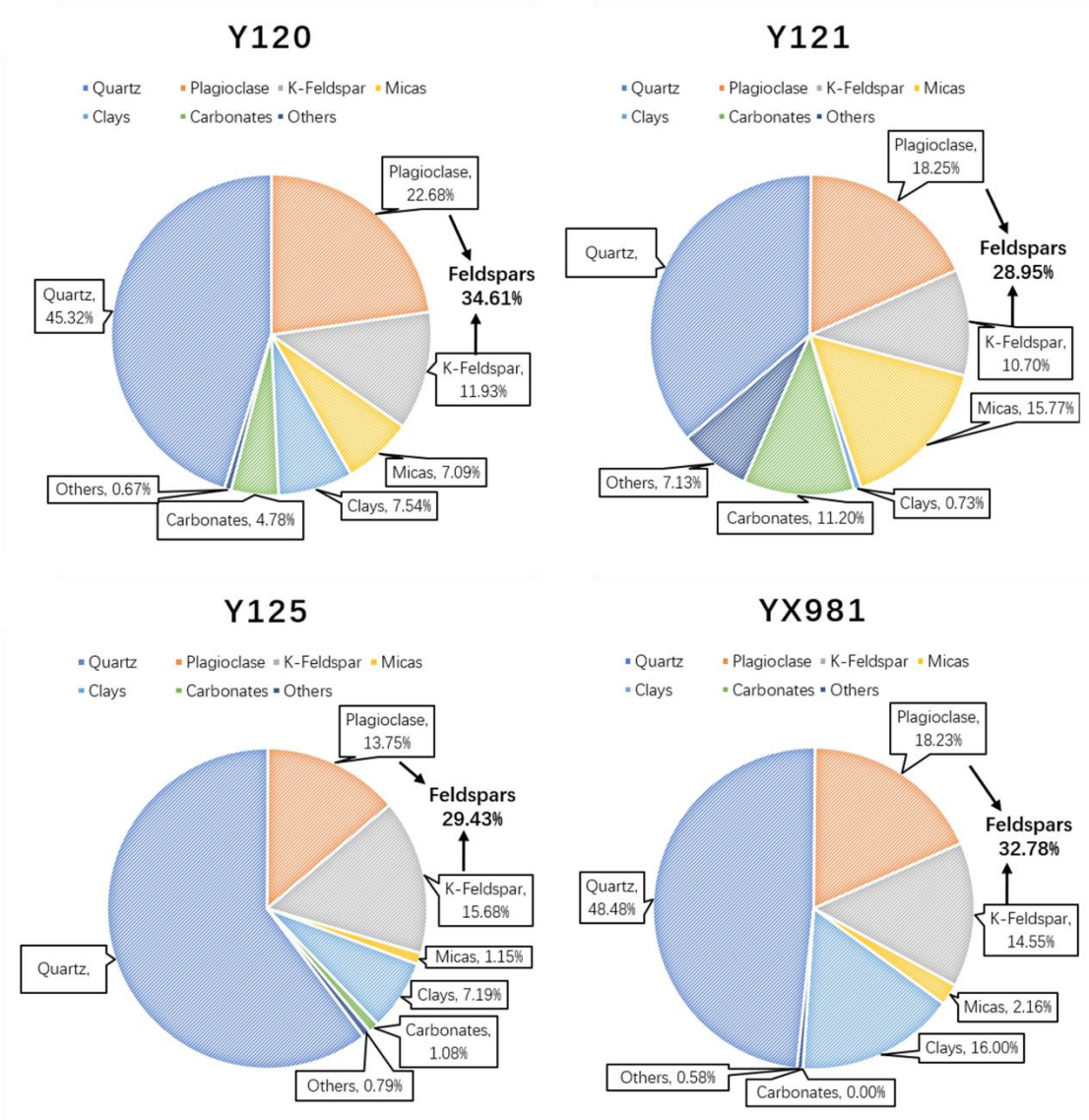

Figure 4.3 – *Mineral compositions of sample Y100, Y118, Y120, Y121, Y125 and YX981. Data was obtained by FIB AMICS.*

Microscopy observation shows that sample *Y125* was moderately sorted, medium sand (grain size 0.26 mm, approximately), in sub-rounded roundness. Photomicrographs by microscopy shows that despite the influence of carbonate cementation, the porosity of sample *Y125* (26.86%) was at relatively high level in comparison to the other samples in the study (Figure 4.4 A, B; Table 4.2). Based on photomicrographs by microscopy, connectivity of pore space in sample *Y125* is good (Figure 4.4). Extensive detrital-grain-size primary intergranular pore and secondary pores caused by extensive feldspar dissolution lead to such a high porosity. Based on FIB AMICS quantitative

compositional analysis, sandstone sample *Y125* was identified as lithic arkose (Figure 4.4 C). Compositional analysis of sample *Y125* shows that sample *Y125* has the highest content of quartz (60.36%) when compared with other the samples in this study, but the lowest content of feldspar (29.43%) (Table 4.2 and Figure 4.3). Though the content of K-feldspar (15.68%) was the second highest among all six samples, the lowest content of plagioclase (13.75%) makes *Y125* the only sample which contains more K-feldspar than plagioclase. Carbonates and micas are both at a low-level amount with 1.08% and 1.15%, respectively.

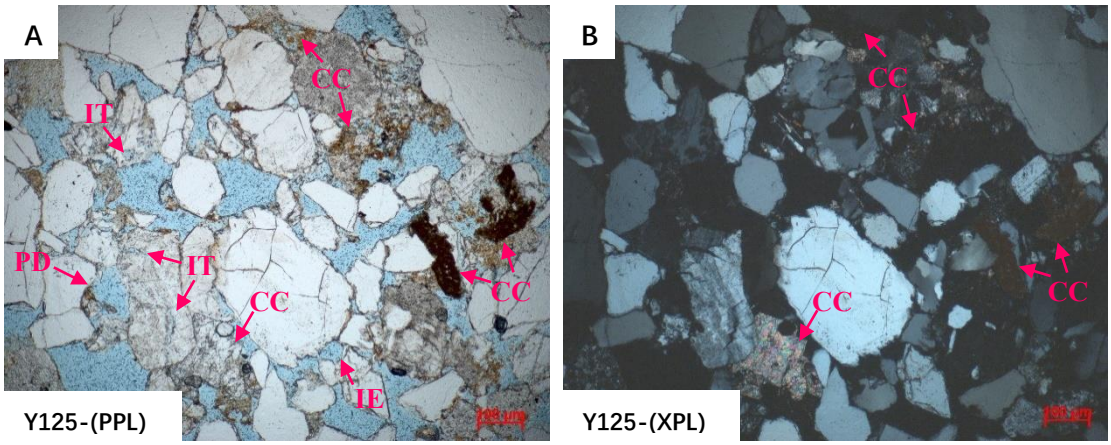

Note: IT = Intragranular, IE = Intergranular, PD = Partial grain dissolution, CC = Carbonate cement; PPL = Plane-polarized light, XPL = Cross-polarized light.

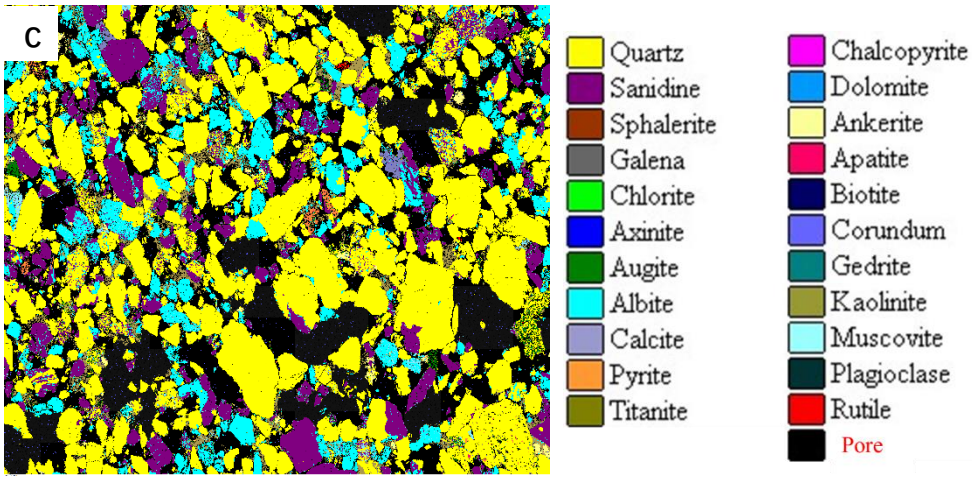

Figure 4.4 – *Photomicrographs by microscopy of carbonate cement and secondary pores led by feldspar dissolution in sample Y125 (A and B); Photomicrograph by FIB AMICS of mineral composition in sample Y125 (C), minerals distinguished by color.*

Microscopy observation shows that sample *YX981* was moderately sorted, fine sand (grain size 0.21 mm, approximately), in sub-rounded roundness. Photomicrographs by microscopy observation

shows that sample *YX981* was the only one without any observable carbonate cement, which was a possible explanation for it having a porosity 16.12% in *YX981*. Based on photomicrographs by microscopy, connectivity of pore space in sample YX981 is good (Figure 4.5). The types of pore included intergranular, partial grain dissolution and grain moudic (Figure 4.5 A, B). Based on FIB AMICS quantitative compositional analysis, sandstone sample *YX981* was identified as lithic arkose (Figure 4.5 C). Quantitative compositional analysis of the *YX981* shows that the content fraction of composition (pores removed) of K-feldspar, plagioclase and quartz was 14.55%, 18.23% and 48.48%, respectively (Table 4.2 and Figure 4.3). Compared with other samples, *YX981* contained the most clay of all the study samples (16.00%) but the least carbonate (0.00%).

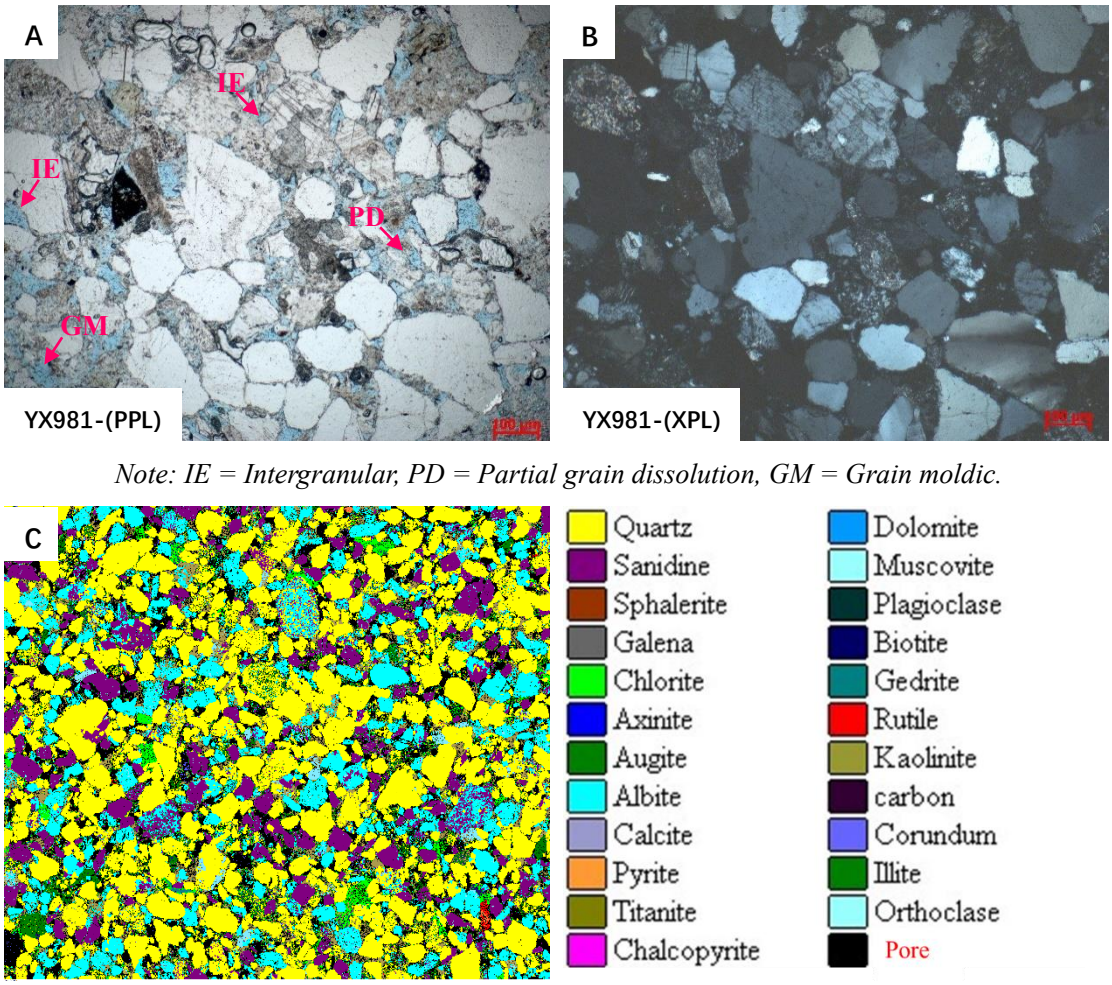

Note: IE = Intergranular, PD = Partial grain dissolution, GM = Grain moldic.

Figure 4.5 – *Photomicrographs by microscopy of carbonate cement and secondary pores led by feldspar dissolution in sample YX981 (A and B); Photomicrograph by FIB AMICS of mineral composition in sample YX981 (C), minerals distinguished by color.*

Microscopy observation shows that sample *Y120* was moderately moderately sorted, fine sand (grain size 0.20 mm, approximately), in sub-angular roundness. Porosity of sample Y120 was 16.12 % (Table 4.2). Based on photomicrographs by microscopy, connectivity of pore space in sample *Y120* was good (Figure 4.6). Besides pores of intergranular and partial grain dissolution, pores of intragranular and grain moldic were also observed in Figure 4.6 A, indicating further feldspar dissolution than observed in samples *Y100* and *Y118*. As for two previous samples, carbonate occurs as cement (Figure 4.6 B). Based on FIB AMICS quantitative compositional analysis, sandstone sample *Y120* was identified as arkose (Figure 4.6 C). Compositional analysis of sample *Y120* showed that the composition (pores removed) of K-feldspar, quartz and clays was 11.93%, 45.32% and 7.54%, respectively (Table 4.2; Figure 4.3). The content of plagioclase (22.68%) and total amount of feldspar (34.61%) in *Y120* were both the second highest when compared with the other samples in the study. The content of carbonates (4.78%) was the second highest as well.

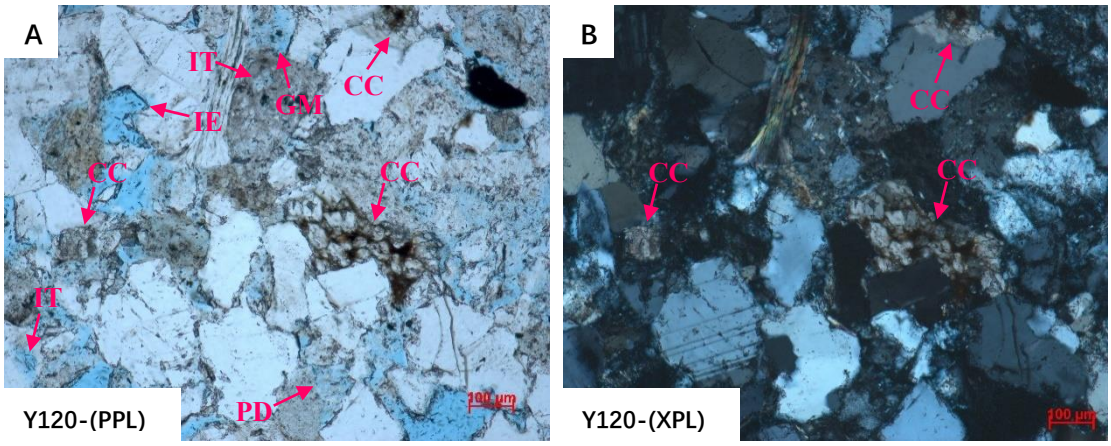

Note: IT = Intragranular, IE = Intergranular, PD = Partial grain dissolution, GM = Grain moldic, CC = Carbonate cement.

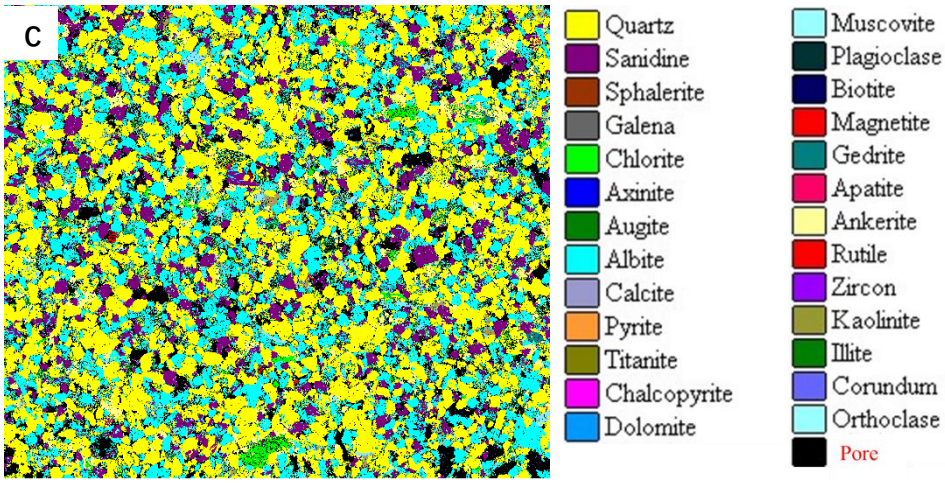

Figure 4.6 – *Photomicrographs by microscopy of carbonate cement and secondary pores led by*

feldspar dissolution in sample Y120 (A and B); Photomicrograph by FIB AMICS of mineral composition in sample Y120 (C), minerals distinguished by color.

Microscopy observation shows that sample *Y121* was very poorly sorted, fine sand (grain size 0.19 mm, approximately), in sub-rounded roundness. Photomicrographs by microscopy shows elarge amount of micrite matrix and carbonate cement almost filled all the space between detrital grains (Figure 4.7 A, B). Porosity of *Y121* was 5.39% (Table 4.2). Based on photomicrographs by microscopy, connectivity of pore space in sample *Y121* is bad (Figure 4.7). Feldspar dissolution was rare in sample *Y121*, as the precipitation of carbonate cements could lead the increase alkalinity of subsurface fluids (Hefferan and O'Brien, 2005), while feldspar dissolution is an acid-consuming process (Yuan et al., 2017). Based on FIB AMICS quantitative compositional analysis, sandstone sample *Y121* was identified as shaly arkose (Figure 4.7 C). Compositional analysis of the *Y121* showed that the composition (pores removed) of K-feldspar, plagioclase and quartz was 10.70%, 18.25% and 36.23%, respectively (Table 4.2 and Figure 4.3). The content of clays (0.73%) in *Y121* was far less than for the other samples, while the content of micas (15.77%) and carbonates (11.20%) was far higher than the other samples. Ankerite with content of 10.66% was the dominates phase among all carbonates (Table 4.2).

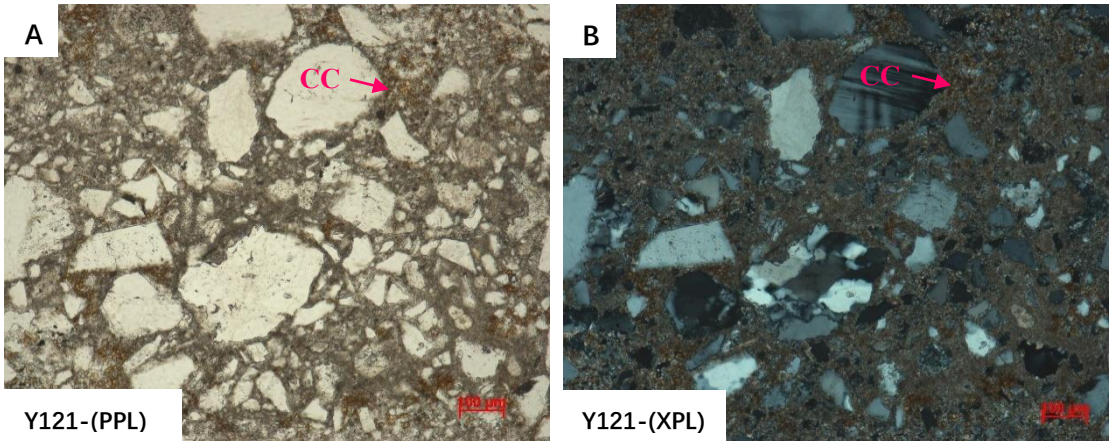

Note: CC = Carbonate cement.

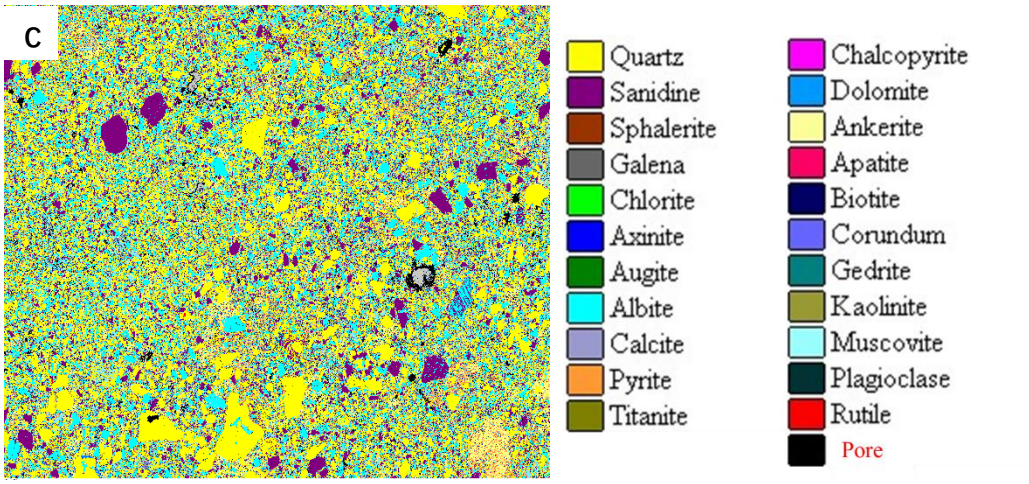

Figure 4.7 – *Photomicrographs by microscopy of carbonate cement and secondary pores led by feldspar dissolution in sample Y121 (A and B); Photomicrograph by FIB AMICS of mineral composition in sample Y121 (C), minerals distinguished by color.*

Microscopy observation shows that sandstone sample *Y100* was moderately moderately sorted, fine sand (grain size 0.17 mm, approximately), in angular roundness. Porosity of *Y100* was 20.18% (Table 4.2). Based on photomicrographs by microscopy, connectivity of pore space in sample *Y100* is good (Figure 4.8). The dominant pore type of sample *Y100* was intergranular, including primary pores and secondary pores created by dissolution along feldspar grain edges (Figure 4.8 A). Figure 4.8 A also indicates secondary pores caused by partial feldspar dissolution. Carbonates occurs as cement (Figure 4.8 B), though the content was at a low percentage. Based on FIB AMICS quantitative compositional analysis, sandstone sample *Y100* was identified as lithic arkose (Figure 4.8 C). Compositional analysis of sample *Y100* showed that the content fraction of carbonate (excluding pore space as below) was only 0.74% (Table 4.2 and Figure 4.3) . The content fraction of K-feldspar, plagioclase, quartz and clays was 16.27%, 18.63%, 49.51% and 9.85%, respectively. The content of the sum of all feldspars in *Y100* (34.90%) was the highest of all samples.

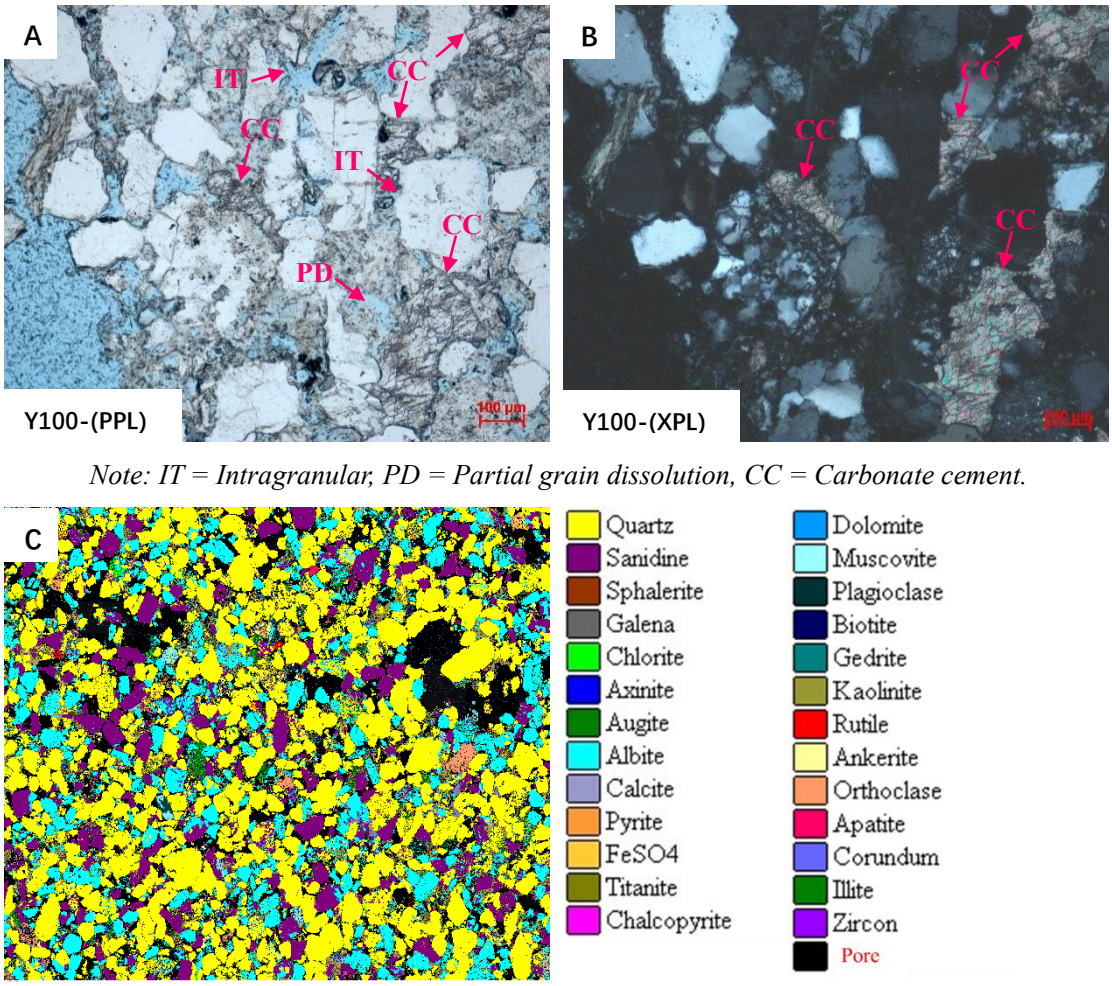

Note: IT = Intragranular, PD = Partial grain dissolution, CC = Carbonate cement.

Figure 4.8 – *Photomicrographs by microscopy of carbonate cement and secondary pores led by feldspar dissolution in sample Y100 (A and B); Photomicrograph by FIB AMICS of mineral composition in sample Y100 (C), minerals distinguished by color.*

Microscopy observation show that sandstone sample *Y118* was poorly sorted, very fine sand (grain size 0.12 mm, approximately), in sub-angular roundness. Porosity of sample *Y118* was only 8.97% (Table 4.2). Based on photomicrographs by microscopy, connectivity of pore space in sample *Y118* is bad (Figure 4.9). Feldspar dissolution created secondary pores of intergranular and partial grain dissolution, but Figure 4.9 A and B show that some carbonate cement could fill pores led by feldspar dissolution, indicating that some carbonate cementation probably happened not earlier than feldspar dissolution. Quantitative compositional analysis shows that the content fraction of composition (pores removed) of K-feldspar, plagioclase, quartz, clays and carbonates was 8.11%, 25.93%, 43.71%, 6.54% and 1.38%, respectively (Table 4.2 and Figure 4.3). Based on compositional analysis, sandstone sample *Y118* was identified as arkose (Figure 4.9 C). The content of the sum of both

feldspars (34.03%) of *Y118* was closed to *Y100*, while the content of plagioclase (25.93%) was the highest of all the samples included in this study. In contrast, the content of K-feldspar (8.11%) was the lowest among six samples.

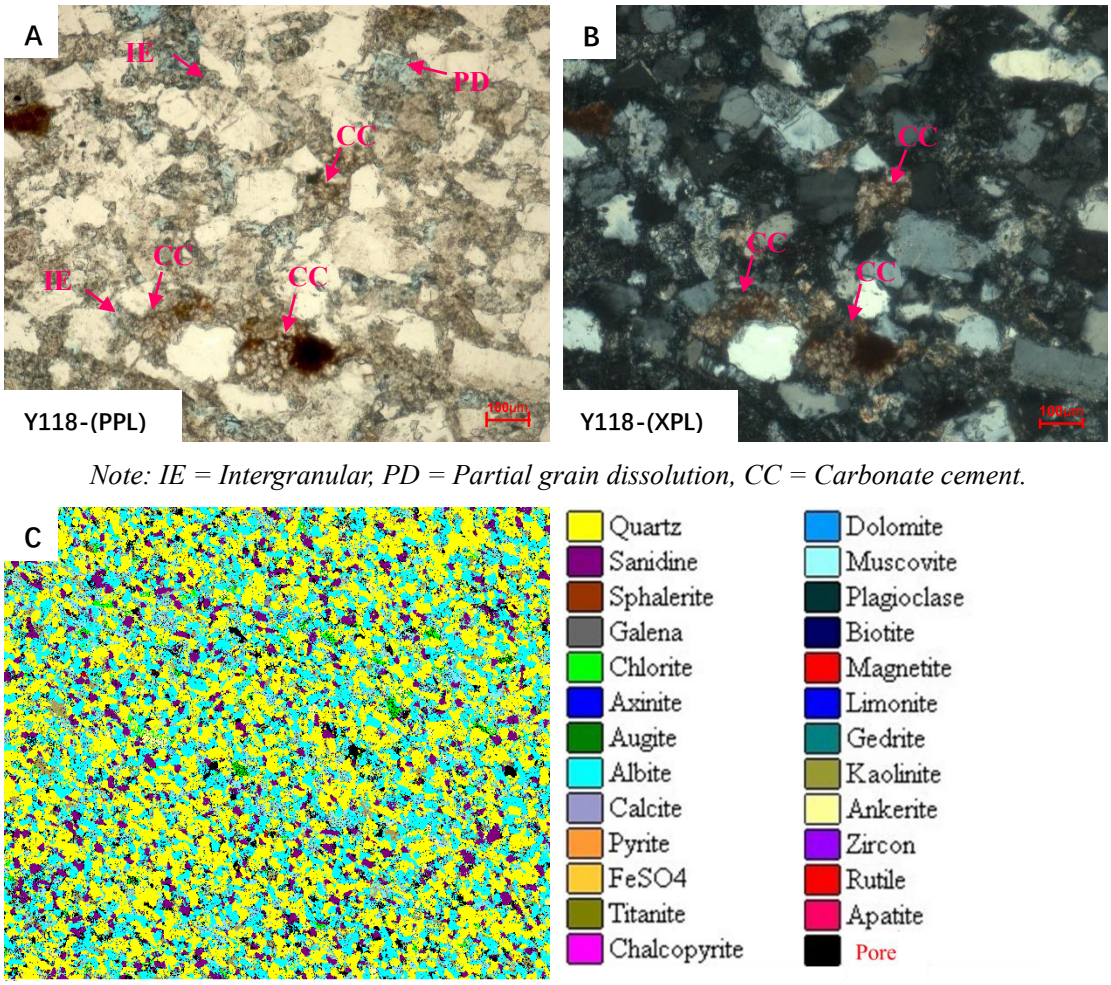

Note: IE = Intergranular, PD = Partial grain dissolution, CC = Carbonate cement.

Figure 4.9 – *Photomicrographs by microscopy of carbonate cement and secondary pores led by feldspar dissolution in sample Y118 (A and B); Photomicrograph by FIB AMICS of mineral composition in sample Y118 (C), minerals distinguished by color.*

Table 4.3 – *Specific content of each other minerals apart from above main mineral phases in Table 4.2.*

Mineral	Average/%	Mineral	Average/%
Apatite	0.03	Pyrite	1.03
Augite	0.08	Rutile	0.11
Axinite	0.17	Zircon	0.01
Corundum	0.16	carbon	0.02
$FeSO_4$	0.02	Gedrite	0.03

Other minerals apart from above main mineral phases (silicas, feldspars, micas, clays and carbonates) are listed in Table 4.3. In five samples, the sum content of these mineral was lower than 1 %, while in sample *Y121*, these minor minerals occupy 7.13 % of the area in total, where 5.48 % was pyrite (Table 4.2).

4.3 SEM and EDS

Both SEM observation and EDS analysis of samples were conducted before and after the physical simulation experiments. Due to the large sample size (60 samples in total) and constraint of time, ten typical samples were selected for SEM and EDS. Analysis of mineral composition shows that *Y121* was rich in carbonates (Table 4.2), therefore sample *Y121-unreacted* and *Y121-140 ℃-4 MPa* were selected to show the potential dissolution of original carbonate led by CO_2 injection in the physical experiment. Analysis of TGA results show that *Y118* and *YX981* had positive performance of carbonate precipitation (Table 4.5 in Section 4.5), so sample *Y118-unreacted, Y118 -50 ℃ - 9 MPa*, *Y118 -100 ℃ - 9 MPa*, *Y118 -140 ℃ - 9 MPa*, and sample *YX981-unreacted*, *YX981-50 ℃ - 4 MPa*, *YX981-100 ℃ - 4 MPa*, *YX981-140 ℃ - 4 MPa*.

According to mineral compositional analysis, *Y121-unreacted* was rich in ankerite cement (content of 11.20%) (Table 4.2). SEM photomicrographs shows that ankerites in *Y121-unreacted* were subhedral in morphology and all surface were coated with flake mineral, i.e. kaolinite (Figure 4.10 A). The ratio of Ca /Mg was nearly one, which was the typical element composition of ankerite. Due to limitation of voltage, Fe element was not able to be detected consistently. Ankerites observed in *Y121-140 ℃-4 MPa* were also coated with kaolinite, but the shape of ankerites were incomplete (Figure 4.10 B), indicating original carbonates in unreacted samples could be dissolved possibly by the injection CO_2. The effect of dissolution of original carbonates is discussed in Section 5.2.

A

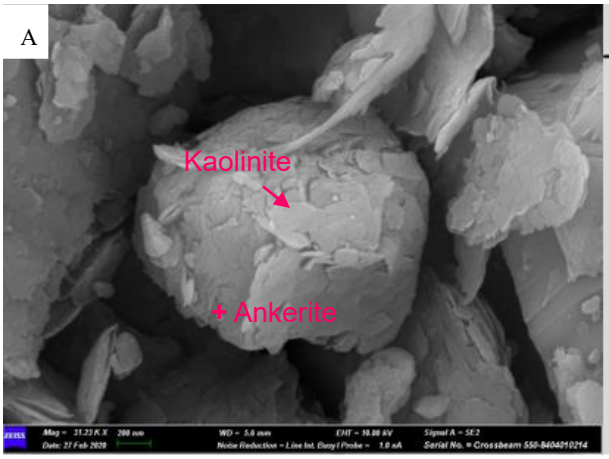

Element	Mass / %	Atom / %
Ca	12.11	5.51
Mg	4.78	3.58
Al	4.52	3.05
K	0.88	0.41
Na	0.80	0.63
C	12.42	18.86
O	53.17	60.60
Si	11.32	7.35

B

Element	Mass / %	Atom / %
O	57.06	74.15
Ca	21.06	10.93
Mg	7.12	6.10
Fe	6.99	2.60
Si	3.78	2.80
Na	2.56	2.32
Al	1.43	1.11

Figure 4.10 – *SEM photomicrographs and EDS analyses of (A) Y121-unreacted and (B) Y121-140 ℃-4 MPa. The red cross represents the location of EDS analysis.*

Unreacted samples were represented by *Y118-unreacted* (Figure 4.11 A), whose content of carbonate was 1.26%, and *YX981-unreacted* (Figure 4.11 B), whose content of carbonate was zero (presented in Section 4.2). Feldspars identified in *Y118-unreacted* and *YX981-unreacted* were found to have signs mainly of mechanically breakage rather than dissolution.

A

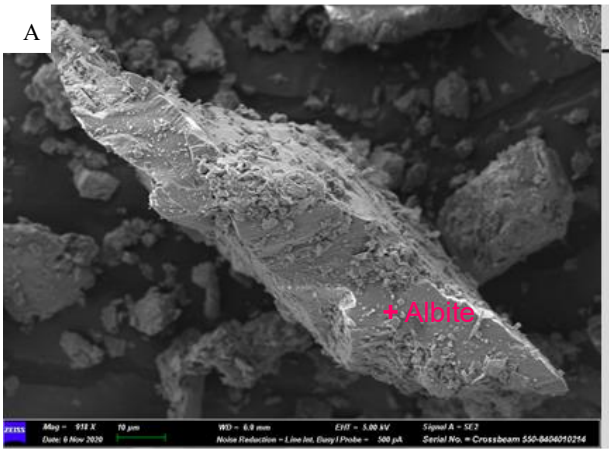

Element	Mass / %	Atom / %
Al	9.35	7.33
O	41.11	54.34
Si	43.34	32.63
Na	6.20	5.70

B

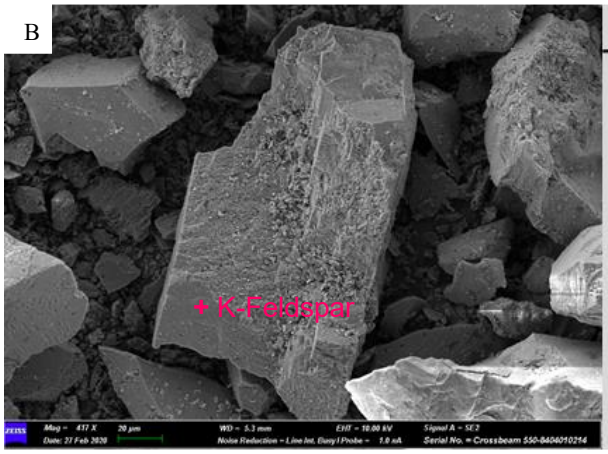

Element	Mass / %	Atom / %
O	29.02	42.89
Na	1.11	1.15
K	13.71	8.29
Si	3.78	37.90
Al	1.43	9.77

Figure 4.11 – *SEM photomicrographs and EDS analyses of (A) Y118-unreacted and (B) YX981-unreacted. The red cross represents the location of EDS analysis.*

Carbonate minerals were not identified through SEM and EDS in sample reacted in lower temperature experiments, *Y118-50 ℃-9 MPa* (Figure 4.12 A)*, YX981-50 ℃-4 MPa* (Figure 4.12 B)*, Y118-100 ℃-9 MPa* (Figure 4.12 C) *and YX981-100 ℃-4 MPa* (Figure 4.12 D), and no obvious evidence of feldspar dissolution was found, except sample *YX981-100 ℃-4 MPa*. In Figure 4.12 D, analysis of SEM and EDS indicate that feldspar was transforming to kaolinite (product of feldspar dissolution) in sample *YX981-100 ℃-4 MPa*.

A

Element	Mass / %	Atom / %
Al	10.32	7.97
O	46.78	60.91
Si	36.17	26.82
Na	1.92	1.74
K	4.81	2.56

B

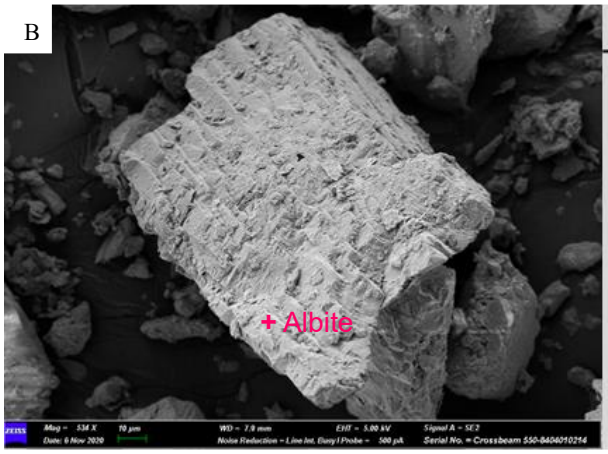

Element	Mass / %	Atom / %
Al	9.18	6.87
O	49.24	62.11
Si	34.43	24.75
Na	7.14	6.27

C

Element	Mass / %	Atom / %
Al	11.08	8.60
O	47.39	62.02
Si	33.22	24.77
Mg	0.50	0.43
K	7.82	4.19

D

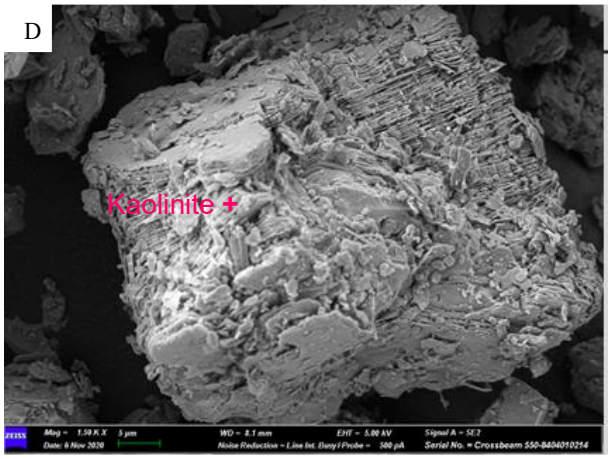

Element	Mass / %	Atom / %
O	41.09	54.61
Si	33.17	25.11
Al	25.73	20.28

Figure 4.12 – *SEM photomicrographs and EDS analyses of (A) Y118-50 ℃-9 MPa, (B) YX981-50 ℃-4 MPa, (C) Y118-100 ℃-9 MPa and (D) YX981-100 ℃-4 MPa. The red cross represents the location of EDS analysis.*

Compare to carbonate mineral in *Y121*, carbonate minerals observed in *Y118 -140 ℃ - 9 MPa* and *YX981-140 ℃ - 4 MPa* were euhedral in morphology (Figure 4.13 A, B and C). Here in complete means that the carbonate mineral surfaces were flat and tidy with few clay coatings, while some clays grew within carbonate. EDS analysis indicates that the ratio of Ca / Mg was over 13, which

was the typical element composition of calcite. Considering that the solution used in physical simulation experiments was rich in Ca^{2+}, the calcite observed in *Y118 -140 ℃ - 9 MPa* was possibly newly formed authigenic mineral as the result of the experiment, while this possibility was even higher in *YX981-140 ℃ - 4 MPa* as no carbonate was found in *YX981-unreacted*. In Figure 4.13 A, B and C, as kaolinite was observed to insert into or attach to calcite, kaolinite was likely to precipitate while calcite was growing at the same time.

A

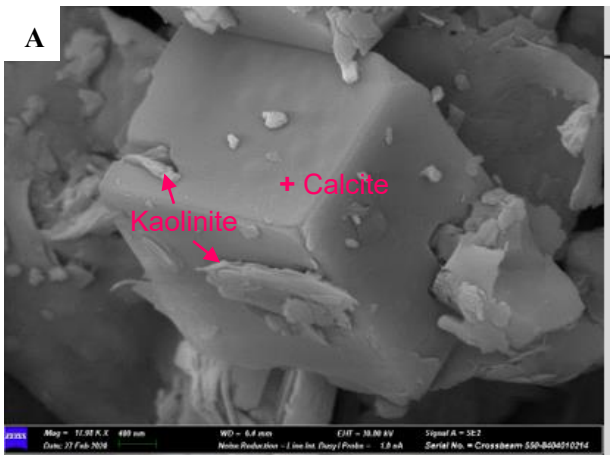

Element	Mass / %	Atom / %
Ca	30.74	14.59
Mg	1.33	1.05
Al	0.94	0.66
K	/	/
Na	0.96	0.79
C	14.67	23.25
O	48.62	57.80
Si	2.74	1.86

B

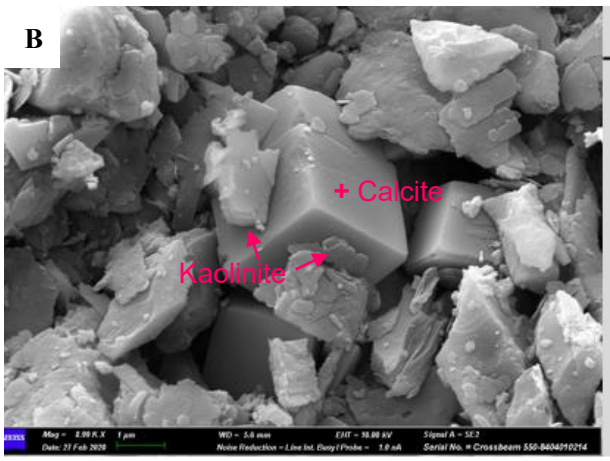

Element	Mass / %	Atom / %
Ca	30.35	14.19
Mg	0.90	0.69
Al	/	/
K	/	/
Na	/	/
C	15.46	24.15
O	50.35	59.01
Si	2.94	1.96

C

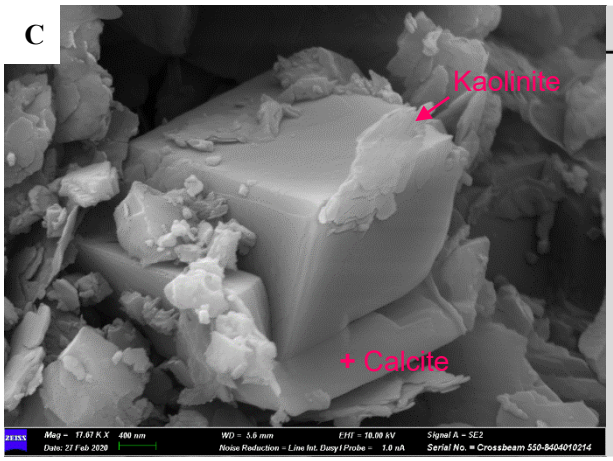

Element	Mass / %	Atom / %
Ca	59.02	40.97
O	24.15	42.00
Si	11.05	10.93
Al	4.43	4.56
Mg	1.35	1.54

Figure 4.13 - *SEM photomicrographs and EDS analyses show new born carbonate mineral from post-experiment samples (A) Y118-140 ℃-9 MPa, (B) and (C) YX981-140 ℃-4 MPa and. The red*

cross represents the location of EDS analysis.

SEM photomicrographs shows that feldspar dissolution was widely developed in samples reacted in high temperature, *YX981-140 ℃-4 MPa* and *Y118-140 ℃-9 MPa*. Three different types of occurrences of feldspar dissolution were identified, namely pores of dissolution along cleavage (Figure 4.14 A), pores of partial grain dissolution (Figure 4.14 B) and pores of intragranular dissolution (Figure 4.14 C), reflecting different stages of feldspar dissolution. As the process of feldspar dissolution continued, pores of dissolution along cleavage can evolve into pores of intragranular dissolution. In Figure 4.14 C, an intragranular pore of a feldspar was filled with kaolinite, indicating that kaolinite was a potential product of feldspar dissolution. The chemical process of feldspar dissolution is discussed in Chapter 6.

A

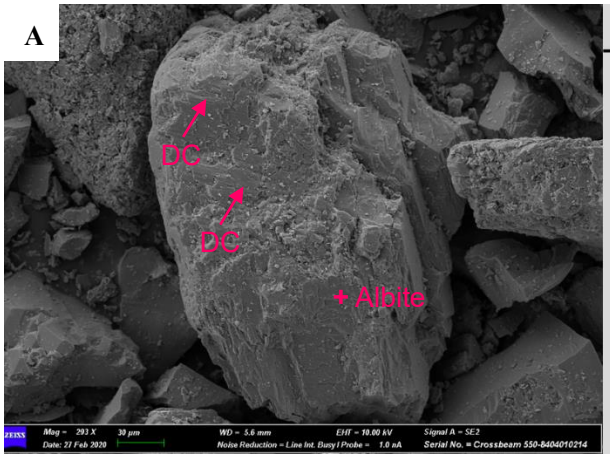

Element	Mass / %	Atom / %
Al	12.16	9.70
O	37.80	50.89
Si	43.91	33.68
Na	6.13	5.74

B

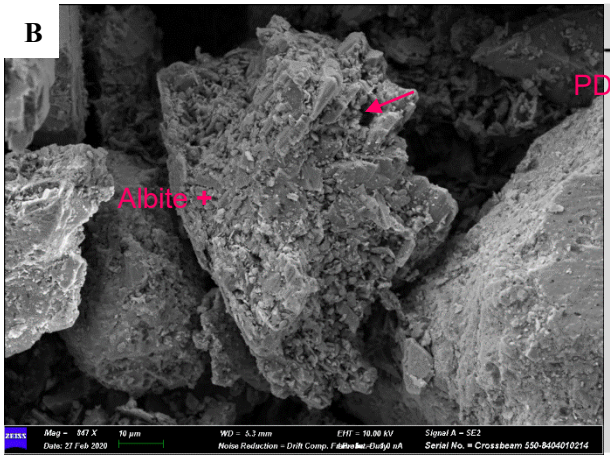

Element	Mass / %	Atom / %
Al	10.41	8.29
O	38.62	51.83
Si	45.53	34.81
Na	5.44	5.08

C

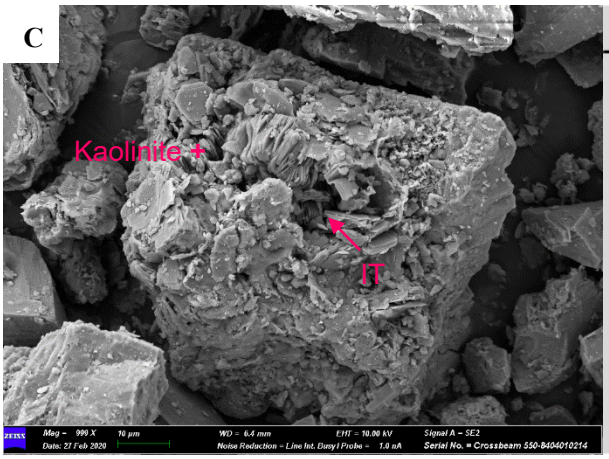

Element	Mass / %	Atom / %
Mg	1.96	1.64
Al	14.00	10.52
O	50.53	64.04
Si	30.35	21.92
Na	0.64	0.58

Note: DC = Dissolution along cleavage, PD = Partial grain dissolution, IT = Intragranular.

Figure 4.14 - *SEM photomicrographs and EDS analyses show feldspar dissolution from post-experiment samples (A) and (B) YX981-140 ℃-4 MPa, (C) Y118-140 ℃-9 MPa. The red cross represents the location of EDS analysis.*

4.4 XRD

All X-Ray diffractograms can be viewed in appendix A. Qualitative analysis of X-Ray diffractograms was performed with reference to SY/T 5163-2018 Analysis method for clay minerals and ordinary non-clay minerals in sedimentary rocks by the X-ray diffraction, released by the National Energy Administration, China (Table 4.4). Results show that quartz, K-feldspar, plagioclase and clay minerals were identified in all samples. Due to the fact that minimum 2θ available for the XRD analysis instrument applied in this study is 5°, specific types of clay minerals have not been analyzed, as their primary peaks were often between 2 and 20° 2θ. Diffraction intensity of carbonates minerals in most samples were in low level, except sample *Y121*. For example, in X-Ray diffractogram of reacted *sample YX981-140 ℃-4 MPa*, the primary and secondary peaks of quartz and feldspar are obviously presented, while the primary peak (2θ = 29.42°) of calcite is not obvious, and the secondary peak is even more so (Figure 4.15). Samples Y121 contained high content of ankerite (10.66%) (Table 4.2), leading the primary peak of ankerite to be easily identified in X-Ray diffractogram (Figure 4.16). This shows that the amount of precipitated carbonate minerals was not very likely over 10% of the total mineral content within 96 hours physical simulation experiments.

Table 4.4 - *2θ of primary / secondary peak of minerals. The reference standard is SY/T 5163-2018 Analysis method for clay minerals and ordinary non-clay minerals in sedimentary rocks by the X-ray diffraction, released by the National Energy Administration, China.*

Mineral	2θ of primary peak	2θ of secondary peak
Quartz	26.64°	20.86°
K-Feldspar	27.46°	26.42°
Plagioclase	27.92°	23.54°
Calcite	29.42°	47.54°
Ankerite	30.84°	41.02°
Dolomite	30.95°	41.15°

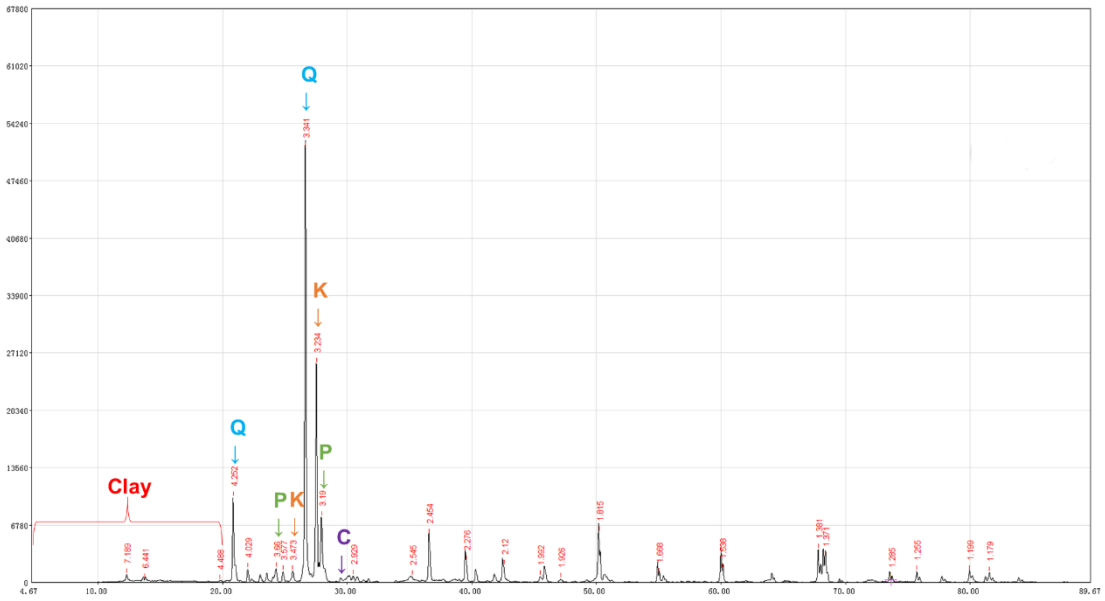

Note: Q = Quartz; K = K-Feldspar; P = Plagioclase; C = Calcite; Clay = Clay minerals.

Figure 4.15 - X-Ray diffractogram *of sample YX981-140℃-4 MPa.*

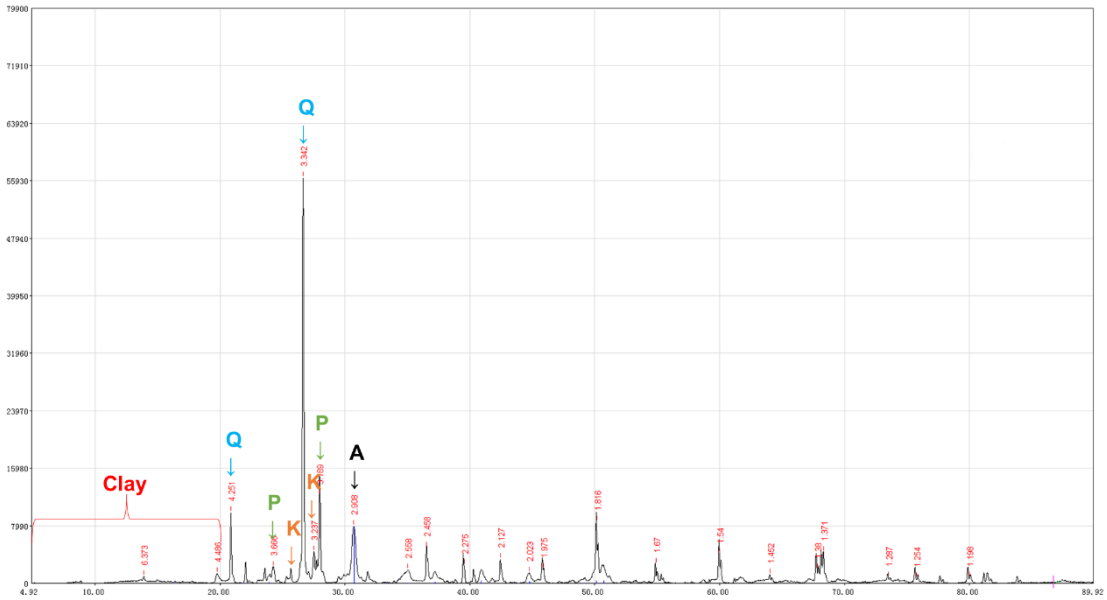

Note: Q = Quartz; K = K-Feldspar; P = Plagioclase; A = Ankerite; Clay = Clay minerals.

Figure 4.16 - X-Ray diffractogram *of sample Y121-Unreacted.*

4.5 TGA

Thermogravimetric Analysis was conducted on all six samples before and after physical simulation experiments (Table 4.5). Average threshold values were selected for volatiles and residual water (0 - 200 ℃), structural water released from clays (200 - 600 ℃) and carbonates (600 - 900 ℃). All sample curves can be viewed in appendix B.

Table 4.5 – *Weight losses of all samples viewed in TGA curves shown in Clay and Carbonate intervals. Orange, i.e. greater than value of unreacted sample; Blue, i.e. less than value of unreacted sample. Note: TGA data of Y125--140℃-4 MPa was error with unknown reason even replicated.*

Sample	TGA Temprange	Unreacted	50 ℃			100 ℃			140 ℃		
			4 MPa	6 MPa	9 MPa	4 MPa	6 MPa	9 MPa	4 MPa	6 MPa	9 MPa
Y100 (loss/%)	200 - 600 ℃ Structural water	0.88	0.97	1.06	0.95	0.79	0.8	0.99	1.27	0.99	0.92
	600 - 900 ℃ Carbonates	1.22	0.74	0.66	0.64	0.83	0.81	0.85	0.77	0.97	0.78
	200 - 900 ℃	2.1	1.71	1.72	1.59	1.62	1.61	1.84	2.03	1.96	1.69
Y118 (loss/%)	200 - 600 ℃ Structural water	1.43	1.72	1.33	1.74	1.5	1.4	1.58	1.98	1.39	3.21
	600 - 900 ℃ Carbonates	1.41	1.18	1	1.21	1.59	1.44	1.47	1.38	1.38	4.39
	200 - 900 ℃	2.84	2.9	2.33	2.95	3.09	2.84	3.05	3.36	2.77	7.59
Y120 (loss/%)	200 - 600 ℃ Structural water	0.84	1.18	1.31	1.09	0.95	0.84	1.03	2.36	0.79	0.9
	600 - 900 ℃ Carbonates	2.65	2.49	2.14	2.45	2.72	2.72	2.62	1.99	3.01	2.63
	200 - 900 ℃	3.49	3.67	3.45	3.54	3.67	3.55	3.64	4.36	3.81	3.53
Y121 (loss/%)	200 - 600 ℃ Structural water	2.44	2.74	2.34	2.46	2.2	2.28	2.22	4.51	2.37	1.82
	600 - 900 ℃ Carbonates	7.49	7.23	7.48	7.32	7.63	7.54	7.96	5	7.66	7.93
	200 - 900 ℃	9.92	9.97	9.82	9.78	9.83	9.82	10.18	9.51	10.02	9.75
Y125 (loss/%)	200 - 600 ℃ Structural water	1.18	1.79	1.33	1.36	1.66	1.26	1.33	11.58	1.56	1.48
	600 - 900 ℃ Carbonates	1.02	0.94	0.81	0.89	1.02	1	0.92	1.47	0.99	0.78
	200 - 900 ℃	2.2	2.73	2.14	2.25	2.68	2.25	2.25	13.05	2.55	2.26
YX981 (loss/%)	200 - 600 ℃ Structural water	0.77	0.89	0.61	0.75	0.89	0.7	0.74	0.91	0.75	0.78
	600 - 900 ℃ Carbonates	0.45	0.57	0.4	0.44	0.57	0.53	0.53	0.77	0.64	0.59
	200 - 900 ℃	1.22	1.46	1.01	1.2	1.46	1.22	1.27	1.68	1.39	1.37

TGA results of sample *Y100* show that weight losses of reacted samples for clay structural water in both *Y100-50℃* (i.e. sample *Y100* reacted in 50℃, including *Y100-50℃-4 MPa, Y100-50℃-6 MPa, Y100-100℃-9 MPa*) and *Y100-140℃* series were greater than *Y100-Unreacted* (0.88 %). While in *Y100-100℃* series, only *Y100-100℃-9 MPa* (0.99 %) loses more structural water than *Y100-Unreacted*. For the 600 - 900 ℃ interval, weight losses of all reacted samples for carbonate were from 0.64 % to 0.97 %, with an average of 0.78 %. Between 200 - 900 ℃ interval, weight losses of all reacted samples for the sum of clays and carbonate were from 1.61 % to 2.03 %, with an average of 1.75 %.Weight losses of *Y100-unreacted* in 600 - 900 ℃ interval (carbonate) and 200 - 900 ℃ interval (clay and carbonate) were 1.22 % and 2.10 %, respectively, greater than weight losses of any other reacted sample *Y100*.

TGA result of sample *Y118* shows that weight losses of most reacted samples for the sum of clay and carbonate were greater than *Y118-Unreacted*, except *Y118-50℃-6 MPa* and *Y118-140℃-6 MPa*. Weight losses for the sum of clay and carbonate of another 6 MPa reacted sample, i.e. *Y118-100℃-6 MPa* (2.84 %), was the third lowest among all reacted sample *Y118*. In clay interval (200 – 600 ℃), weight losses of most reacted samples were greater than unreacted sample, especially *Y118-140℃-9 MPa,* which lost 3.21 %, over twice than *Y118-Unreacted* (1.43%). Similar pattern occurs in carbonate interval (600 – 900 ℃), weight losses of *Y118-140℃-9 MPa* were over three times more than *Y118-Unreacted* (1.41 %).

TGA results of sample *Y120* shows that only *Y120-100℃-6 MPa* and *Y120-140℃-6 MPa* lost more clay structural water than *Y120-Unreacted*. While in carbonate interval, only three reacted samples lost more weight, two from 100℃ series, *Y120-100℃-4 MPa* (2.72%) and *Y120-100℃-6 MPa* (2.72%), and one from 140℃ series, *Y120-140℃-6 MPa* (3.01%). Carbonate weight losses of reacted samples from 50℃ series were all less than *Y120-Unreacted*.

TGA results of sample *Y121* show that though only three reacted samples lost more weight than *Y121-Unreacted* in structural interval, while in carbonate interval three reacted samples from 100℃ series and two from 140℃ (*Y120-140℃-6 MPa* and *Y120-140℃-9 MPa*) lost more weight than *Y121-Unreacted*. Similar to sample *Y121*, in the carbonate interval, weight losses of reacted sample *YX981-100℃* and *YX981-140℃* series were more than *YX981-Unreacted*.

In contrast, *Y125 unreacted* lost more carbonate than *Y125-Unreacted*, except TGA data for *Y125-140℃-4 MPa* which was error with unknown reason. According to TGA curves for *Y125-140℃-4 MPa* presented in Figure 5 in Appendix-TGA Curves, weight percentage decreased by about 4% from 25 ℃ to 100 ℃ and about 7% from 300 ℃ to 400 ℃, respectively. First order derivative of weight change was also variable from 300 ℃ to 400 ℃. Given that these abnormal phenomena were not in line with other normal TGA patterns and still existed even replicated, they were considered being error caused by improper handling of sample after physical simulation experiments.

TGA curve of *Y100-Unreacted* shows that two decomposition peaks occur in the carbonate interval, the first one at approximately 665 ℃ and the second at approximately 843 ℃ (Figure 4.17 A, B, C). However, no curve of reacted sample *Y100* indicate the second peak at approximately 843 ℃ in carbonate interval as *Y100-unreacted.* Differences between the peak position (temperature at which peaks occur) of unreacted and reacted samples are shown in curves of sample *Y125* as well (Figure 4.17 D, E, F). The peak positions of reacted samples in carbonate interval were all at approximately 700 ℃, while the peak position of *Y125-Unreacted* was after 700 ℃ and the peak width was approximately twice more than reacted samples. TGA curve pattern of *Y125-140℃-4 MPa* (Figure 4.17 F) was abnormal even in replication. As it is an obvious error, this curve was excluded from consideration. For TGA curves of sample *Y118, Y120, Y121* and *YX981*, no important difference was observed between the peak position of unreacted and reacted samples. According to mineral compositional analysis of unreacted samples, both sample *Y100* and *Y125* contained calcite, while sample *Y118, Y120, Y121* and *YX981* were almost calcite-free (Figure 4.18). It is possible that the difference of TGA curves between sample *Y100* and *Y125* and sample *Y118*, *Y120*, *Y121* and *YX981* was resulted by calcite.

Generally, though weight losses of sample *Y100* and *Y125* in carbonate interval (600 – 900 ℃) were less than *Y100-Unreacted* and *Y125-Unreacted*, respectively. Samples *Y118*, *Y120*, *Y121*, *YX981* from 100℃ and 140℃ physical simulation experiments lost more weight in carbonate interval (600 - 900 ℃) than those samples from the 50℃ physical simulation experiments, indicating that high temperature was possible to promote carbonate growing in this physical experiment.

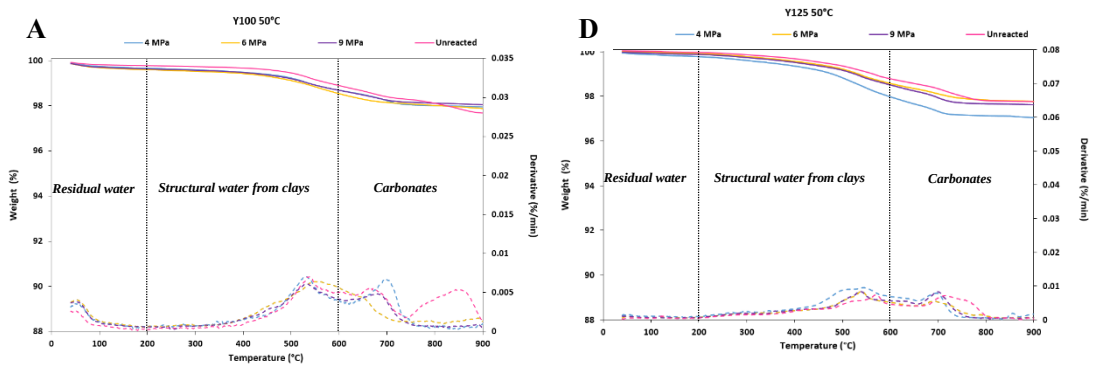

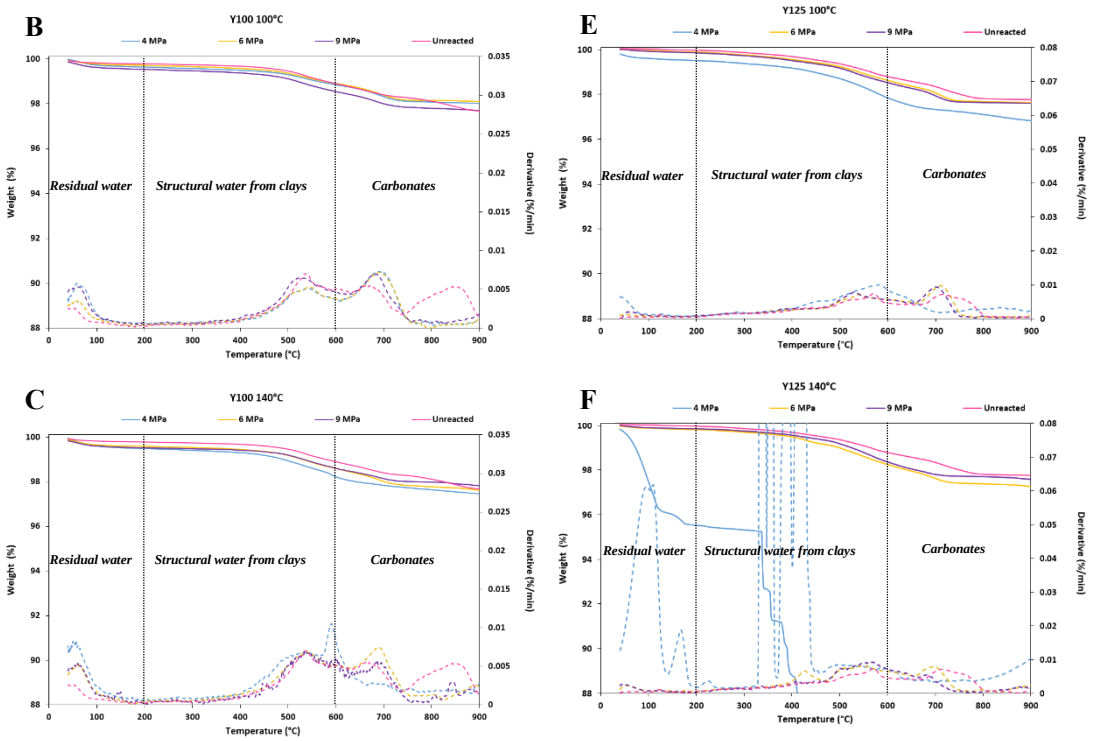

Figure 4.17 –*TGA curves of Samples Y100 and Y125, including both unreacted samples and reacted samples at all temperature * pressure conditions.*

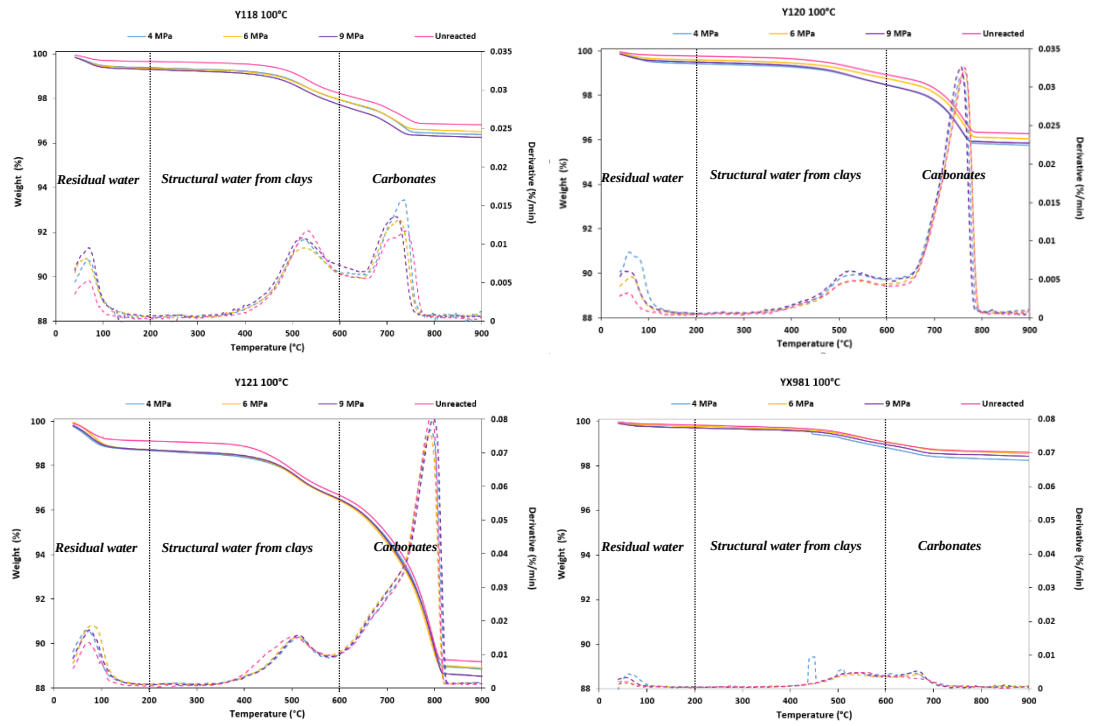

Figure 4.18 – *TGA curves of Samples Y100 and Y125, including both unreacted samples and reacted samples at 100 °C * 4 MPa / 6 MPa / 9 MPa.*

4.6 Further analysis based on TGA - Statistic analysis

diff – the difference between reacted and unreacted samples

Data obtained from TGA was used for ANOVA to identify three variables, sample composition, temperature and pressure, which was statistically significant for carbonation in physical simulation experiments. Details of level of each factor used were listed in Table 4.6. Given the nature of the TGA data it would be meaningless to consider *Temprange* as a variable. But *Temprange* can be included as a factor rather than a variable, to analyze the interaction effects of temperature with other factors (i.e. *Sample*, *Temperature* and *Pressure*). The levels of factor *Temprange* were every 50℃ equally divided temperature range from 500 ℃ to 900 ℃ (temperature range of carbonation decompostition) in TGA analysis. Analysis of interaction effects with temperature could possibly help in identifying the specific temperature when the carbonate decomposed between 600 ℃ and 900 ℃.

The normality test of the data suggested that there were 16 outliers to be removed and so this analysis was based on 471 data points of *diff*. Note that in analyzing *diff* the data for the controls samples has already been included. Then ANOVA GLM was used to investigate the influence of each factor and level on carbonation.

This ANOVA explained 89.5% of the original variance in the dataset. All four factors are found to be significant. In reducing order of importance they are: *Temprange, Sample, Temperature*, and *Pressure*. Of the 10 interactions that could be assessed, eight were also found to be significant - in reducing order of variance explained, they are: *Sample*Temprange, Sample*Temperature*Pressure, Sample*Pressure, Sample*Temperature*Temprange, Sample*Temperature, Temperature*Temprange,* and *Pressure*Temprange, Temperature*Pressure*.

Table 4.6 - *ANOVA model for the GLM design, showing for each factor and interaction the degrees of freedom (DF), the probability (significant if P < 0.05), and the % variance (ω^2).*

Source	DF	P-Value	%ω^2
Sample	5	0	5.43
Temperature	2	0	2.87
Temprange	7	0	9.17
Pressure	2	0.001	0.98
Sample*Temperature	10	0	3.32
Sample*Temprange	35	0	12.22
Temperature *Temprange	14	0	2.43
Sample*Temperature*Temprange	70	0.008	3.60
Sample*Pressure	10	0	7.11
Temperature *Pressure	4	0.002	1.14
Pressure*Temprange	14	0.017	1.20
Sample* Temperature *Pressure	20	0	12.17
Sample*Pressure*Temprange	70	0.197	1.06
Temperature *Pressure*Temprange	28	0.15	0.72
R^2	89.48%		
N	471		
S	0.082		

The five most responsive factors/interactions were: *Sample*Temprange, Sample*Temperature* Pressure, Temprange, Sample*Pressure* and *Sample* (Table 4.7). By integrating the information conveyed in Table 4.2, the effect of *Sample* and interactions with *Sample* played the most important role with the contribution of 71% to the model (Figure 4.19). The *Y118* and *Y120* were two most responsive samples from all six. *Diff* of sample *Y118* was even greater at 9 MPa and 140 ℃*9 MPa, showing high temperature and high pressure (supercriticality) might promote carbonate growth. The initial temperature of carbonate minerals, 600-650 ℃, was the most significant level in *Temprange* factor.

Table 4.7 - *The highest mean of level in five most responsive factors / factor groups, indicating the greatest response.*

Term	N	Mean
Sample*Temprange		
Y120*600-650 ℃	9	0.122088
Sample*Temp*Pressure		
Y118*140 ℃*9 MPa	8	0.4529
Temprange		
600-650 ℃	53	0.0640358
Sample*Pressure		
Y118*9 MPa	24	0.146939
Sample		
Y120	69	0.0541804

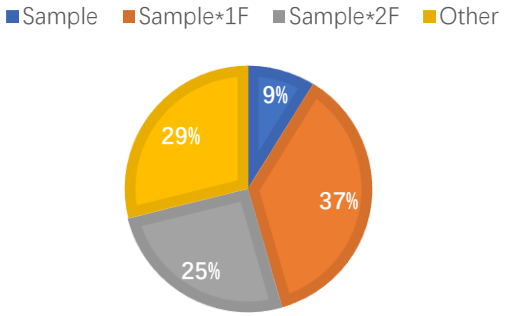

Figure 4.19 - *Pie chart of contribution of the main factor and interaction effects to the ANOVA GLM model of diff.*

The results from post-hoc testing are provided in Table 4.8, and main effect plots were shown in Figure 4.20. Results indicated that the means of *diff* changed with different samples and temperature ranges were complicated.

For the *Temprange* factor, the *diff* mean of 750-800 °C was significantly different from all the other levels in the *Temprange* factor – it should be noted that carbonate decomposition would be expected to occur between 200 °C to 600 °C and dehydroxylation of clay minerals would occur between 600 °C to 900 °C.

For the *Sample* factor. *Y100*, was significantly different from the rest and was the most unresponsive sample. For the other five samples, *Y120* responded greatest, followed by *Y118*, which did not show significant differences with other samples except from *Y100*. Therefore, compared to samples Y100 and Y121, mineral composition of Sample Y118, Y120, Y125, YX981 were more beneficial for carbonation in physical simulation experiments.

Among the remaining two factors, an increase in *temperature* resulted in an increase in carbonation, especially to 140 °C, the highest among all three temperatures which indicated significant differences to the two lower temperatures, while the trend of pressure different. The mean of *diff* reached peak at the lowest pressure, 4 MPa with significant differences with that of higher pressure. Though compared with 6 MPa, 9 MPa was a more responsive level, there was not a significant difference between them. In summary, high temperature (140°C) significantly promoted the conversion of CO_2 to carbonate in physical simulation experiments, while high pressure did not.

Table 4.8 – *Tukey Pairwise Comparisons for each main factor effect.*

Tukey test for Sample

Sample	Grouping	
Y120	A	
Y118	A	B
YX981	A	B
Y125	A	B
Y121		B
Y100		C
Conditions	Y118>Y100	Y120>Y121
P-Value	0.000	0.029

Tukey test for Temp

Temp(°C)	Grouping
140	A
100	B
50	B
Conditions	140>100 (°C)
P-Value	0.000

Tukey test for Pressure

Pressure(MPa)	Grouping	
4	A	
9		B
6		B
Conditions	6<4(MPa)	9<4(MPa)
P-Value	0.001	0.047

Tukey test for Temprange

Temprange (°C)	Grouping			
600-650	A			
500-550	A	B		
550-600	A	B		
650-700	A	B		
850-900	A	B		
700-750		B	C	
800-850			C	D
750-800				D
Conditions	650-700 > 750-800(°C)	700-750 > 750-800(°C)	850-900 > 750-800(°C)	
P-Value	0.000	0.000	0.000	

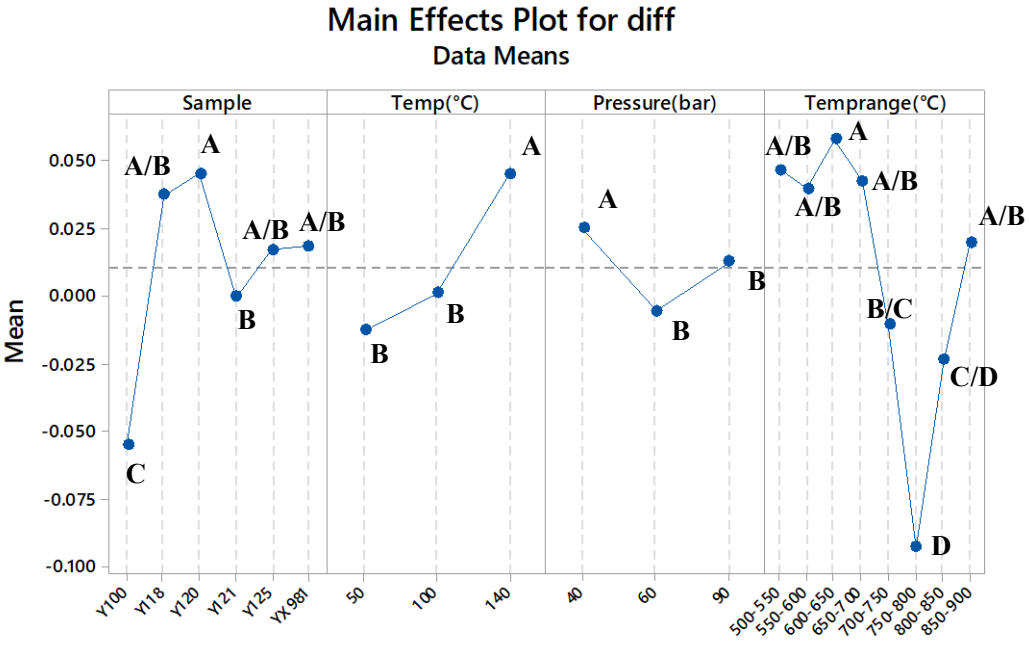

Figure 4.20 - *Sample, Temp, Pressure and Temprange. The significant differences of means were displayed by the labels A, B, C and D, where diff for A >B > C > D. Means that did not share a letter were significant different.*

5. Discussion

5.1 Mineral reactions in CO_2-saturated $CaCl_2$-rich formation water systems.

Based on comprehensive results of multiple analysis, i.e. compositional analysis, XRD, TGA and SEM / EDS, to reacted / unreacted sandstone samples, mineral changes of feldspar dissolution and calcite precipitation were identified in reacted sandstone samples after physical simulation experiments (Figure 4.13; Figure 4.14). Results of ANOVA indicate that factors of mineral composition, temperature and pressure (Table 4.6) can exert significant influence on carbonate dissolution / precipitation. To clarify how different factors impact the chemical process of CO_2 mineral trapping in CO_2-saturated $CaCl_2$-rich formation water systems, it is necessary to figure out the mineral reactions occurred in the physical simulation experiments.

At the beginning of the chemical process, CO_2 was saturated in saline solution due to high pCO_2, creating $CO_{2\,(aq)}$ (Equation 5.1) and $H_2CO_{3\,(aq)}$ (Equation 5.2). Then $H_2CO_{3\,(aq)}$ primarily ionized and decomposed into H^+ and HCO_3^- ions rapidly (Equation 5.3), followed by HCO_3^- secondary ionization where H^+ and CO_3^{2-} were released (Equation 5.4) (Giles, 1986).

$$CO_{2\,(g)} = CO_{2\,(aq)} \quad \text{Equation 5.1}$$

$$CO_{2\,(g)} + H_2O \leftrightarrows H_2CO_{3\,(aq)} \quad \text{Equation 5.2}$$

$$H_2CO_{3\,(aq)} \leftrightarrows H^+ + HCO_3^- \quad \text{Equation 5.3}$$

$$HCO_3^- \leftrightarrows H^+ + CO_3^{2-} \quad \text{Equation 5.4}$$

For feldspar dissolution, though cations of K-feldspar and albite are different, both reactions are acid-consuming and produce kaolinite. Injection of CO_2 provide acid to both reactions of feldspar dissolution (Equation 5.5 and Equation 5.6) (Zhu et al, 2009; Tutolo et al, 2015; Yuan et al, 2019).

$$KAlSi_3O_8(K\text{-}Feldspar) + H^+ + 0.5H_2O = K^+ + 2SiO_{2(aq)} + 0.5Al_2Si_2O_5(OH)_4\ (Kaolinite) \quad \text{Equation 5.5}$$

$$NaAlSi_3O_8(Albite) + H^+ + 0.5H_2O = Na^+ + 2SiO_{2(aq)} + 0.5Al_2Si_2O_5(OH)_4\ (Kaolinite) \quad \text{Equation 5.6}$$

For reaction of calcite precipitation (Equation 5.7, Equation 5.8) in Ca^{2+}-rich solution, CO_3^{2-}

provided by injection of CO_2 can be consumed by abundant Ca^{2+}, forming calcite to sequester CO_2 (Yuan et al, 2015; Wang et al, 2020; Barclay and Worden, 2000).

$$Ca^{2+}+CO_3^{2-}=CaCO_3 \quad \text{Equation 5.7}$$

$$Ca^{2+}+HCO_3^{-}=CaCO_3+H^+ \quad \text{Equation 5.8}$$

According to Equation 5.1 to 5.4, it can be concluded that injection of CO_2 probably has a positive effect on both feldspar dissolution and calcite precipitation in CO_2-saturated $CaCl_2$-rich formation water systems in the long term (Yuan et al, 2015; Tutolo et al, 2015). In order to further clarify the chemical process of CO_2 mineral trapping in this system, the sequence of feldspar dissolution and calcite precipitation and the relationship between them need to be further discussed.

5.2 Coupling processes of the chemical reaction relevant to mineral trapping in silicate-rich sandstones with CO_2-saturated saline

Precipitation of carbonate minerals in subsurface porous rocks is an important and a safe pathway to storage CO_2 (Yuan et al, 2015; Tutolo et al, 2015; Wang et al, 2020; Celia and Nordbotten, 2009; Zwaan and Semkens, 2009; Yang et al., 2010; Myer, 2011). As carbonate minerals occurred in the present experiments, identification and understanding of the chemical reaction processes relevant to carbon storage can provide implications for CCS in buried rocks. Based on analyses of mineral reactions in CO_2-saturated $CaCl_2$-rich formation water systems from the physical simulation experiments, a series of three-stage chemical reaction processes in silicate-rich sandstones with CO_2-saturated saline can be proposed to sequester CO_2 in the present experiments, which are analogous with chemical processes identified in the numerical simulations conducted by previous research (Barclay and Worden, 2000; Yuan et al., 2015a; Wang et al, 2020).

Stage I: Carbon Dioxide dissolved to form carbonic acid

Chemical process **Stage I** is illustrated as above from Equation 5.1 to 5.4. Due to the relatively lower equilibrium constant of HCO_3^- secondary ionization, solution acidity in experiment system was dominated by H^+ created from $H_2CO_{3\,(aq)}$ primary ionization, increasing dissolution of carbonate and feldspar (Giles, 1986; Emery et al., 1990; França et al., 2003; Bjørlykke and Jahren, 2012).

Stage II: Dissolution of carbonate and feldspar minerals

Acid produced in **Stage I** led to dissolution of both carbonate and feldspar. In this case, carbonate phase included calcite and ankerite, and the feldspar phase included K-feldspar and plagioclase.

K-feldspar and plagioclase had similar dissolution process as they share the same crystal structure, while different carbonate minerals had different solubility. There were two carbonate phases observed in sample *Y100* and *Y125* before reaction, i.e. calcite and ankerite, while in sample *Y118*, *Y120*, *Y121* the only carbonate phase was ankerite. Almost no carbonate grew in sample *YX981* before experiment. Therefore, the solubility of calcite and ankerite were compared. The temperature and pressure functions of calcite and dolomite respectively in equilibrium with CO_2 aqueous solution (Cai, 1993). Functions are shown in Equation 5.9 and 5.10.

$$-7\,272.636 + 44.73T = p + 1.491ZT\ln p \qquad \text{Equation 5.9}$$

$$-8\,611.961 + 54.705T = p + 1.635ZT\ln p \qquad \text{Equation 5.10}$$

In Equation 5.9 and 5.10, T is temperature; Z is compressibility factor; p is pressure. The functions indicate that the order of solubility is calcite > dolomite when the temperature, pressure and the amount of CO_2 in the solution are the same.

Dissolution of carbonates was observed in SEM analysis of sample *Y121-140 ℃-4 MPa* (Section 3, Figure 4.10). Chemical reaction of calcite, ankerite and feldspar dissolution in **Stage II** are shown in Equations 5.11 through 5.13, respectively. Basically, these dissolution processes are all acid-consumed chemical reactions, leading pH to increase. Therefore, mineral dissolution in **Stage II** had possibility to create a solution environment beneficial for coming carbonate precipitation, i.e. feldspar dissolution had possibility to promote CO_2 mineral trapping (Barclay and Worden, 2000; Yuan et al., 2015a; Tutolo et al, 2015; Wang et al, 2020).

$$CaCO_3\ (Calcite) + CO_{2\ (g)} + H_2O = Ca^{2+} + 2\ HCO_3^- \qquad \text{Equation 5.11}$$

$$0.5Ca(Mg,Fe)(CO_3)_2\ (Ankerite) + H^+ = HCO_3^- + 0.5Ca^{2+} + 0.5Mg^{2+} + 0.5Fe^{2+} \qquad \text{Equation 5.12}$$

$(K,Na)AlSi_3O_8$ (K-Feldspar / Albite) + $CO_{2\,(g)}$ + $1.5H_2O$ = $0.5Al_2Si_2O_5(OH)_4$ (Kaolinite) + $2SiO_2$ (Quartz) + K^+ + Na^+ + HCO_3^-

Equation 5.13

The logarithmic values of the chemical equilibrium constants of these dissolution reactions are shown in Equation 5.14, 5.15, 5.16, respectively. Further comparisons among $logK_1$ to $logK_3$ in Figure 5.1, indicate that at the same temperature, the equilibrium constant of the calcite dissolution is nearly 0.5 orders of magnitude greater than that of dolomite; the equilibrium constant of the feldspar dissolution is 3-5 orders of magnitude greater than that of carbonate minerals, and the higher the temperature, the greater the difference. Additionally, chemical kinetics data in Table 5.1 indicates that reaction rate of calcite dissolution was several orders of magnitude greater than feldspar dissolution. Due to effects of greater reaction rate and fewer content and chemical equilibrium constant, reaction of calcite dissolution, i.e. Equation 5.11, was possible to achieve the equilibrium in **stage II** quickly, while feldspar dissolution still kept processing slowly and far away from equilibrium. Therefore, the concentration of Al^{3+} and $SiO_{2\,(aq)}$ released from dissolved feldspar was not high enough to achieve precipitation of kaolinite and quartz (Yuan et al., 2015a).

$logK_1 = loga[Ca^{2+}] + 2loga[HCO_3^-] - logf[CO_{2(g)}] - loga[H_2O]$ Equation 5.14

$logK_2 = 0.5loga[Ca^{2+}] + 0.5loga[Mg^{2+}] + 0.5loga[Fe^{2+}] + loga[HCO_3^-] - loga[H^+]$ Equation 5.15

$logK_3 = loga[K^+] + loga[HCO_3^-] - logf[CO_{2(g)}] - 1.5loga[H_2O]$ Equation 5.16

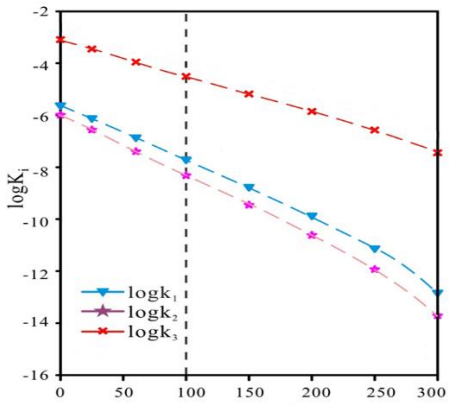

Figure 5.1 - *Comparison among dissolution equilibrium constant of calcite ($logK_1$), dolomite ($logK_2$) and feldspar ($logK_3$) (Yuan et al., 2015a).*

Table 5.1 - *Chemical kinetics data of calcite and feldspar dissolution (Arvidson et al., 2003; Harouiya and Oelkers, 2004; Pokrovsky et al., 2005); Xu et al., 2005; Kampman et al., 2009).*

Mineral	Activation energy (kJ/mol)	Specific surface area (cm2/g)	Reaction rate, 25 re k_m(mol/cm^2/sec)	Reaction rate, 100 re k_m(mol/cm^2/sec)
Calcite	48.2	1500	1500^{-9}	$4.98ite^{-8}$
Feldspar	57.78	100	1007^{-17}	$1.088pa^{-15}$

Stage III: Feldspar continued to be dissolved and calcite started to precipitate

Due to a greater equilibrium constant and lower reaction rate, feldspar dissolution continued to process when **Stage II** ended. Increasing concentration of K^+, Al^{3+}, $SiO_{2\,(aq)}$ and HCO_3^- released from dissolved feldspar into solution led to kaolinite and quartz to precipitate (Equation 5.9).

In this physical simulation experiment, CO_2 was in excess in the sealed system as in this case pCO_2 was almost equal to system pressure. Effects of continuous CO_2 dissolution and acid-consumed mineral dissolution led Equation 5.1 to 5.4 to go forward, resulting in increasing concentrations of $HCO3^-$ and CO_3^{2-}. Given the fact that the solution applied in physical experiments was rich in Ca^{2+}, calcite was possible to precipitate. In SEM photomicrograph Figure 4.11, clays inserting into calcite was possible to evidence the simultaneous precipitation of calcite and kaolinite in this stage. SEM photomicrograph of sample *Y118* (Figure 5.2) shows that authigenic quartz grew on clays, indicating simultaneous precipitation of secondary authigenic quartz and clays.

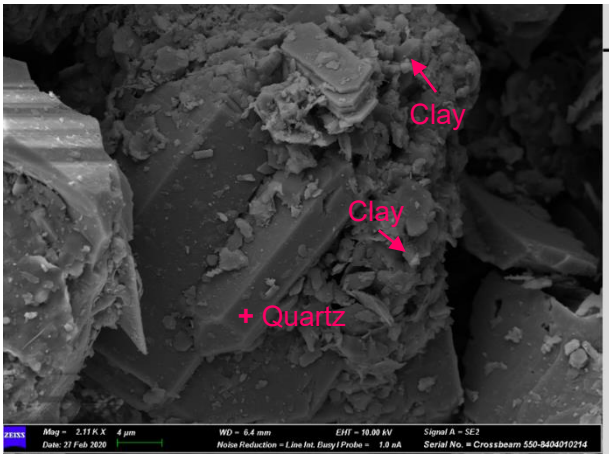

Element	Mass / %	Atom / %
Al	5.95	4.51
O	48.93	62.61
Si	45.12	32.88

Figure 5.2 - *SEM photomicrographs and EDS analyses show the authigenic quartz and clays in sample Y118. The red crosses represent the locations of EDS analysis.*

5.3 Factors affecting the Geological CO_2 trapping

CO_2 mineral trapping in silicate-rich sandstones with CO_2-saturated $CaCl_2$-rich formation water was led by coupling chemical processes discussed in Section 5.2. In order to effectively sequester CO_2 in practical geological reservoir, controlling factors of the coupling chemical processes need to be discussed further.

5.3.1 Interaction effects with controlling factors of physical simulation experiments

In physical simulation experiments, controlling factors were set as *Sample* (mineral composition), *Temperature* and *Pressure*. According to result of ANOVA (Table 4.6), all these three factors were statistically significant (though the result indicate that *Pressure* was less important). Based on result of ANOVA, interactions effect among factors were conducted in Minitab 18.

Results from the interaction of *Sample* with *Temperange is* shown in Figure 5.3. In Figure 5.3, an interaction effect between the *Sample* and *Temprange* was clear in the particular temperature range where carbonate minerals were known, i.e. from 600-650 °C to 850-900 °C. Difference between weight loss of reacted and unreacted samples, referred as *diff*, increased from 550-600 °C to 600-650 °C in all samples except *Y100*, illustrating that carbonate had decomposed. Samples sorted by their maximum values of *diff* were, in decreasing order: *Y120, Y121, Y125, Y118, YX981* and *Y100*. The maximum value of *diff* was in temperature range 600-650 ºC for samples *Y120, Y121, Y125*; while for samples *Y118* and *YX981* the peak in *diff* was at the range 650-700 °C, and the lowest peak of *diff* (*Y100*) lay at higher temperature range 700-750 °C.

For five of the samples (*Y120, Y121, Y125, Y118* and *Y100*) the values of *diff* decreased after its peak value, while for *YX981*, which only fluctuated up and down around the its mean value (0.01317). The *diff* of *Y120* and *Y125* began to decrease from temperature range 700-750 °C and reached a minimum in the temperature range 750-800 °C, while *diff* of Y121 plunged after a plateau period and reached the minimum from 700-750 °C. The *diff* of Y118 and Y100 reached their lowest value in the temperature range 700-750 °C and 800-850 °C respectively.

In general, results of interaction of *Sample* with *Temprange* show that more carbonate content was

identified in *Sample Y118, Y120* and *YX981* than *Sample Y100, Y121* and *Y125.* But according to results of mineral composition of unreacted samples (Table 4.2), Y120 originally contains 4.78% carbonate minerals, which may not be completely dissolved in chemical process **Stage II,** affecting evaluation by TGA of effectiveness of CO_2 mineral trapping. Therefore, mineral composition of *Sample Y118* and *YX981* were evaluated as more conductive to CO_2 mineral trapping.

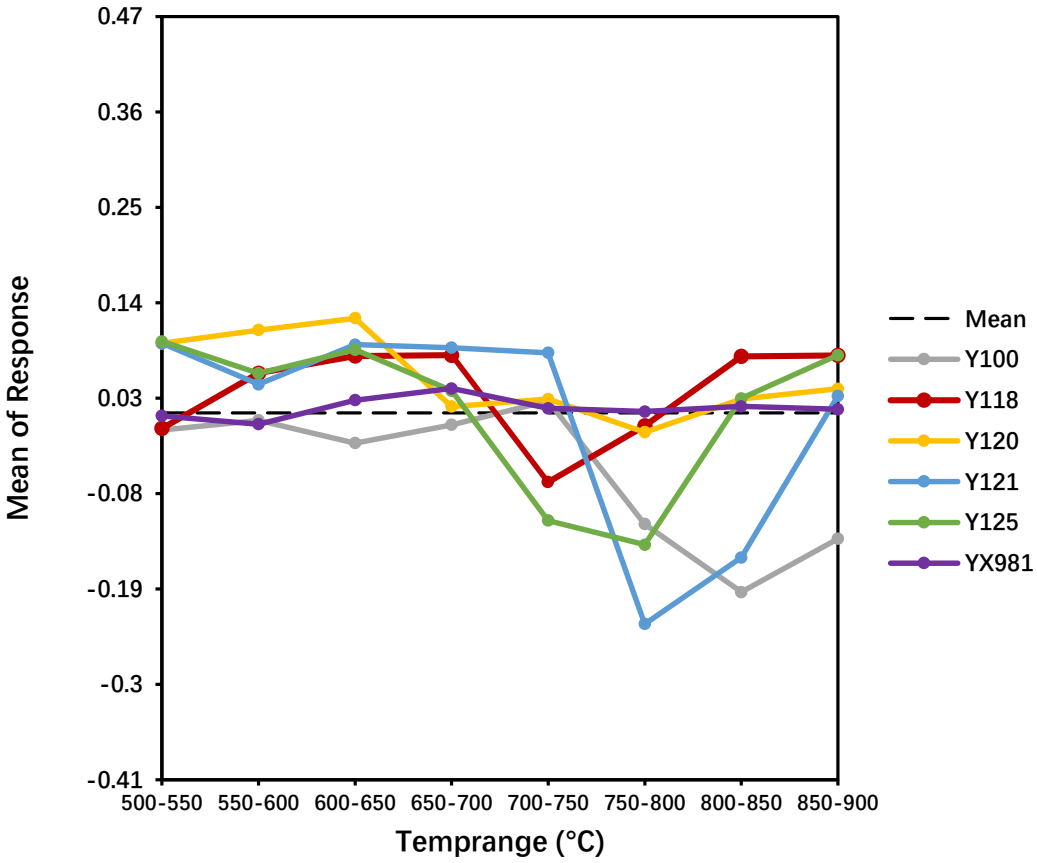

Figure 5.3 - *Interaction plot for Sample*Temprange.*

Several patterns of behavior appear in the interaction between *Sample* and *Pressure* (Figure 5.4). Four samples reached their *diff* maximum at 4 MPa. Three of them, i.e. *Y120 Y121* and *YX981*, *diff* declined when pressure rose, indicating that low pressure was preferable for carbonate mineral production, while *Y125* witnessed a decrease of *diff* at a pressure of 6 MPa whereas there was a smaller increase of *diff* at a pressure of 9 MPa. The pattern shown by *Y125* was similar to that of *Y118*. Results showed there was no interaction between the samples *Y118* and *Y125* from 4 MPa to 6 MPa, but from 6 MPa to 9 MPa, *diff* of *Y118* went up by a greater amount than seen for other

samples. The mean of response of *Y118* at 9 MPa was the maximum in interaction effect between *Sample* and *Pressure*, followed by mean of response of *Y120* at 4 MPa. The most negative interaction effect in each pressure condition was for *Y110*, and response of *Y100* hardly changed with pressure. In summary, interaction effect related to *Pressure*, 4 MPa was more important in carbonate mineral production than the other studied, though for one sample, *Y118*, the most important pressure was 9 MPa. In general, results of interaction of *Sample* with *pressure* show that for all six samples, the amount of carbonate precipitation in physical experiments were not linear positive correlated with pressure.

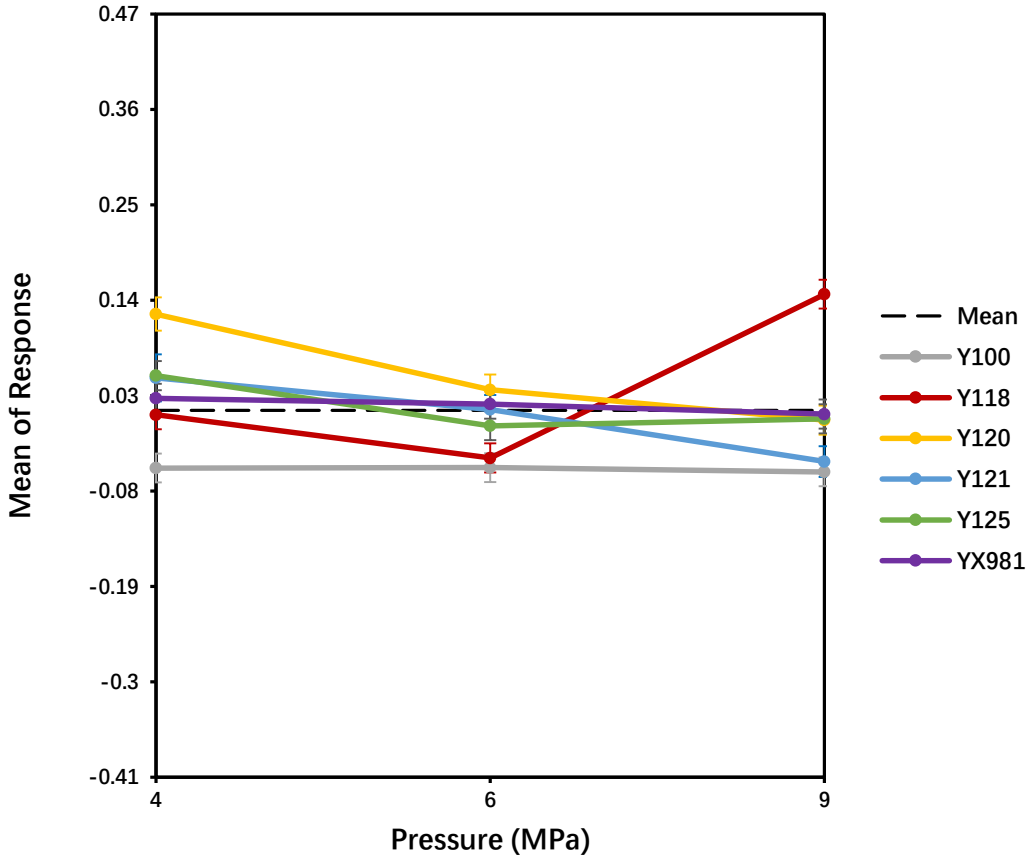

Figure 5.4 - *Interaction plot for Sample*Pressure.*

In interaction plot of *Sample* and *Temperature* (Figure5.5), shows that interaction effects between sample and high temperature were larger. Most samples, other than *Y121*, reached maximum of *diff* at 140 °C: the *diff* for *Y121* peaked at 100 °C. However, *diff* of *Y120* and *YX981* reached their lowest value at 100 °C: the *diff* of the other three samples increased with increasing temperature. Generally, higher temperatures were more beneficial for carbonate mineral production.

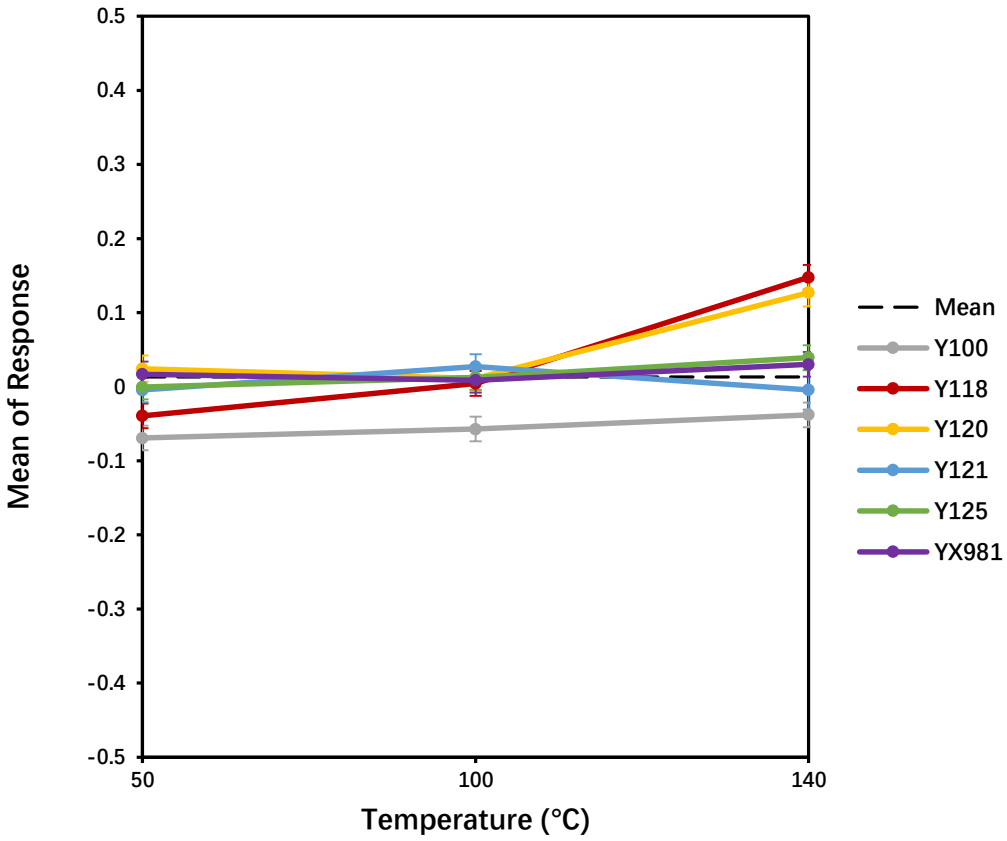

Figure 5.5 - *Interaction plot for Sample*Temperature.*

Interactions between the *Temprange* and *Temperature*, and *Temprange* and *Pressure* factors were significant but only explained 2.43 % and 1.20 % of the original variance respectively (Figure 5.6, 5.7). In interaction plot of *Temprange* and *Temperature* (Figure 5.6), though *diff* of interaction with *Temprange* at 140 °C were not obviously lower than *diff* of interaction with *Temprange* at 100 °C at temperature range 650-700 °C, 700-750 °C and 800-850 °C. Greater *diff* were achieved in other temperature among carbonate mineral decomposition temperature range, indicating that high temperature 140 °C was more conductive to formation of carbonate minerals during physical experiments.

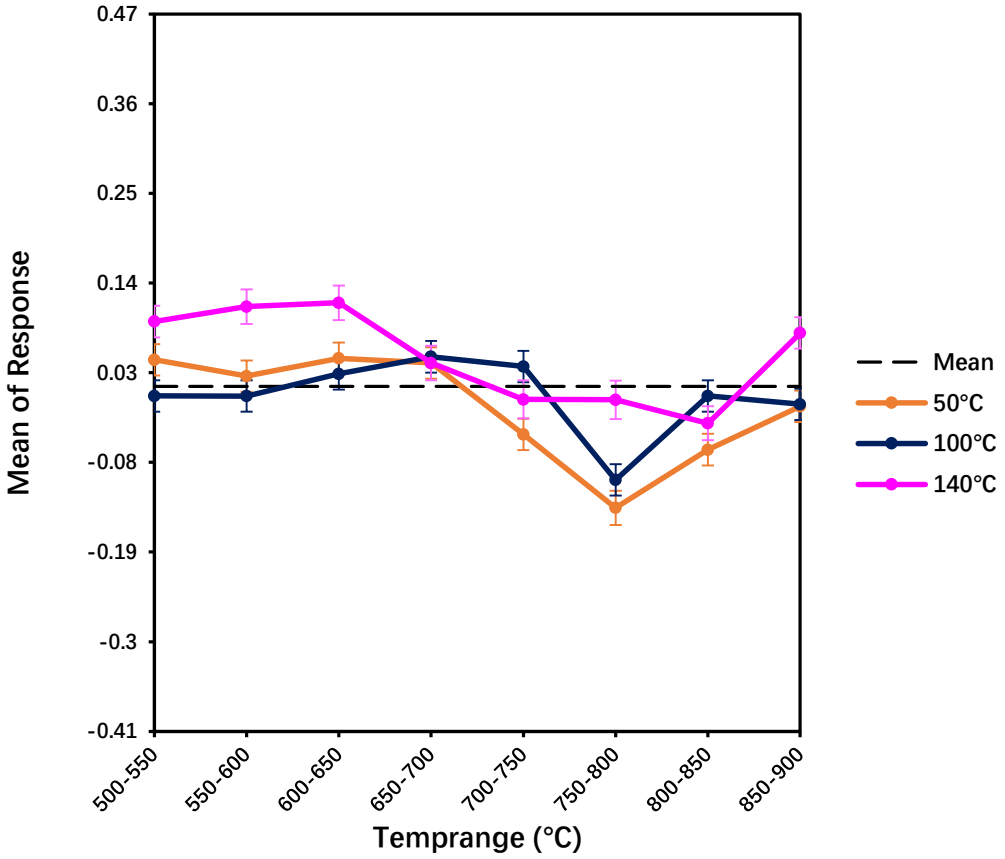

Figure 5.6 - *Interaction plot for Temperature*Temprange.*

High pressure did not further promote the carbonate forming process. Similar to interactions with *Temprange* at 100 °C, *diff* of interations with *Temprange* at 9 MPa only had small advantage (less than 0.09 diff mean of response) in 650-700 °C, 700-750 °C and 800-850 °C, but surpassed by *diff* of interactions with *Temprange* at 4 MPa in carbonate mineral decomposition temperature range (Figure 5.7). Therefore, the higher levels of *Temperature*, 140 °C, increased the formation of carbonate minerals, and both low (4 MPa) and high level (9 MPa) also promoted carbonate mineral production though not by as much as high temperature.

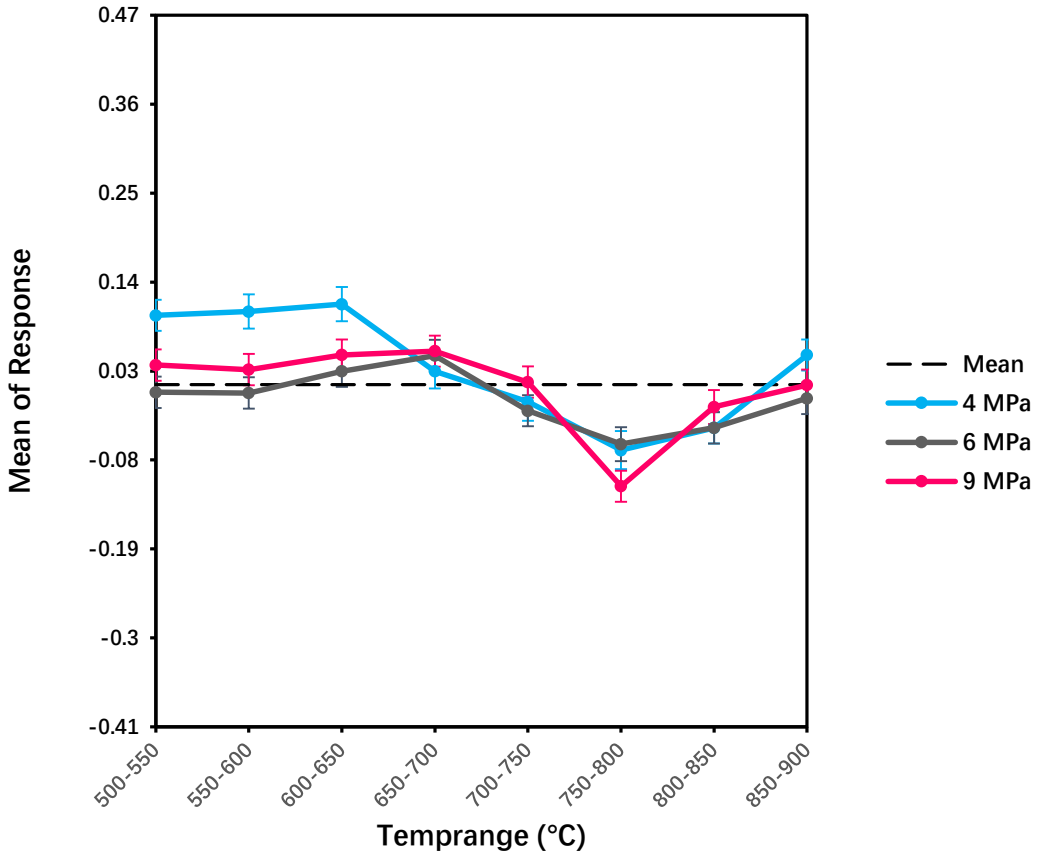

Figure 5.7 - *Interaction plot for Pressure*Temprange.*

The interaction effect of *Pressure*Temperature* (Figure 5.8) was even less important than *Temprange*-related interaction effects, i.e. this interaction term explained a smaller proportion of the original variance. No clear differences emerged among *diff* of 3 pressures in 50 °C and 100 °C. Even in 140 °C the differences were not outstanding, either, indicating that the impact of different pressure on CO_2 mineral trapping process in different temperature was not crucial. In contrast, interaction effect of *Sample*Temprange* (Figure 5.3) and *Sample*Temperaure* (Figure 5.5) were much more obvious, indicating that mineral composition and temperature are two critical factors to CO_2 mineral trapping process.

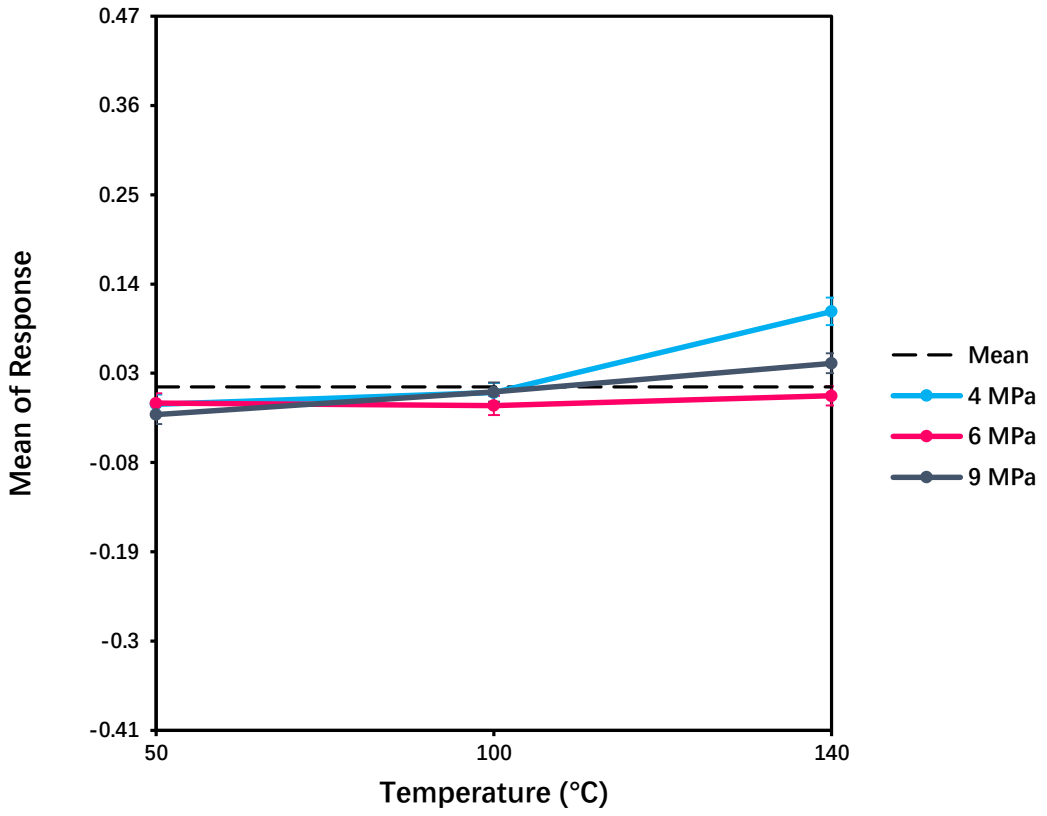

Figure 5.8 - *Interaction plot for Pressure*Temperature.*

The 3-way interactions are shown in Figures 5.9 and 5.10. Firstly, the interaction between the Sample, *Temperature* and *Pressure* was found to be significant interaction and contributed 12.17% to the model (Table 4.6). On comparison of Figure 5.9 A to F, the carbonation effect of sample *Y100* (Figure 5.9 A) and *YX981* (Figure 5.9 F) only changed inconspicuously (the absolute value of the difference from the mean value of mean of response was less than 0.055) at both varying *Temperature* and *Pressure*, while the most increase over all interaction between the *Sample, Temperature* and *Pressure* was for sample *Y118* at 4 MPa from 100 °C to 140 °C (Figure 5.9 B). For interactions between the sample *Y118*, temperature and other two pressures, their carbonation effect both increased though the rates were less from 50 °C to 100 °C, but that of interaction between the sample *Y118*, temperature and 6 MPa decreased at higher temperature while 4 MPa still increased. The other three samples, *Y120, Y121* and *Y125*, showed a common pattern of carbonation increasing with the *Pressure* at 4 MPa from 100 °C to 140 °C: the effect was largest for *Y120* (Figure 5.9 C). The impacts of varying temperatures were not important on interactions between the sample *Y125* and other two pressures, 6 MPa and 9 MPa (Figure 5.9 E). However, at 6 MPa, carbonation in sample

Y120 decreased from 50 °C to 100 °C (Figure5.9 C), while carbonation in sample *Y121* at 9 MPa increased to about 0.16 below 100 °C and then decreased to about -0.19 above 100 °C (Figure 5.9 D).

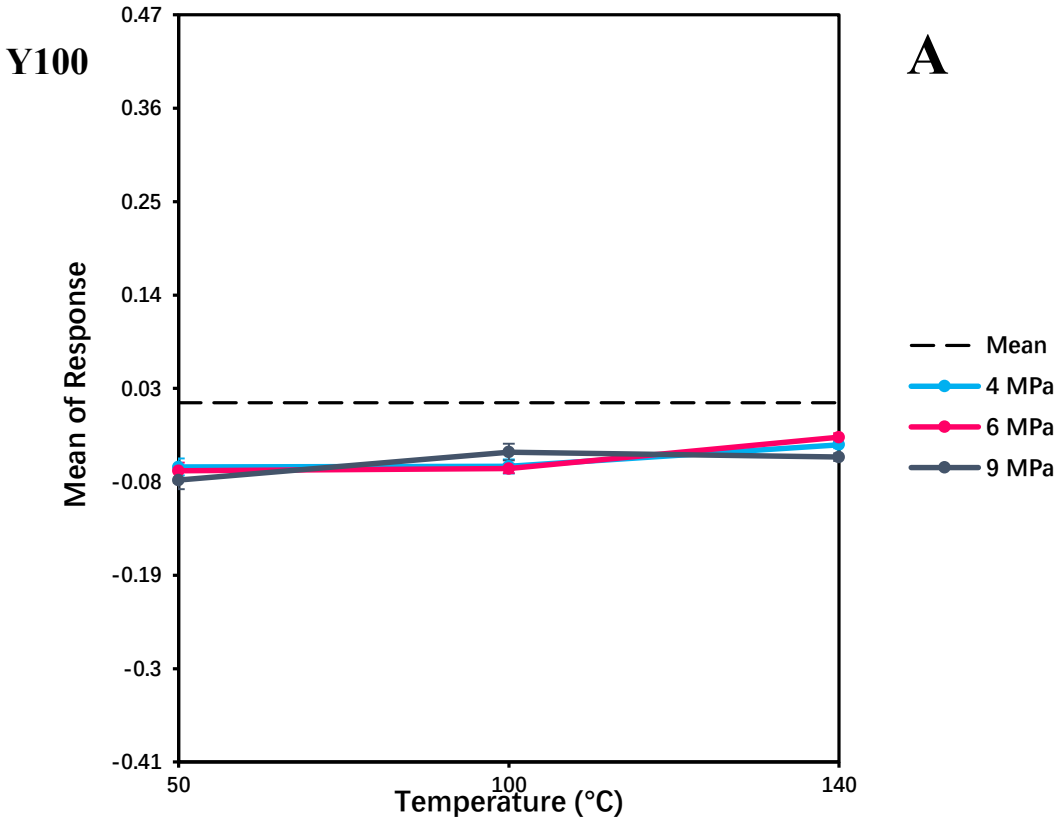

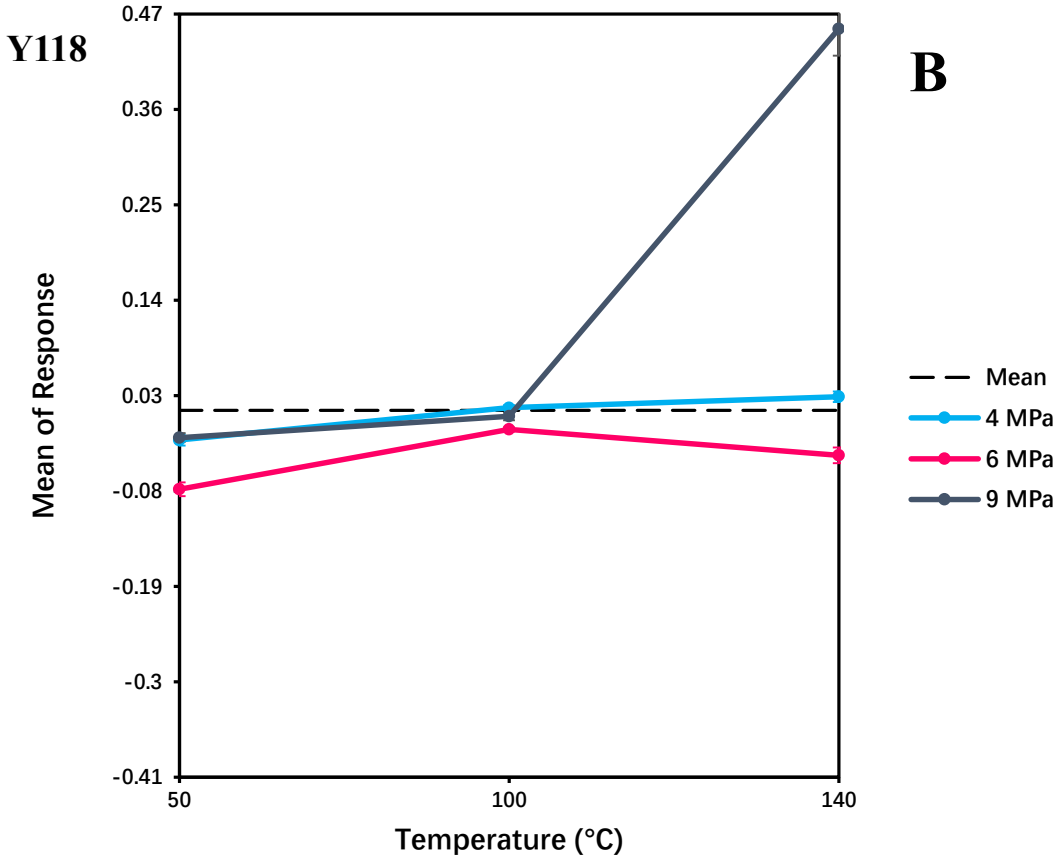
Y118
B
0.47
0.36
0.25
0.14
0.03
-0.08
-0.19
-0.3
-0.41
Mean of Response
50
100
140
Temperature (°C)
Mean
4 MPa
6 MPa
9 MPa

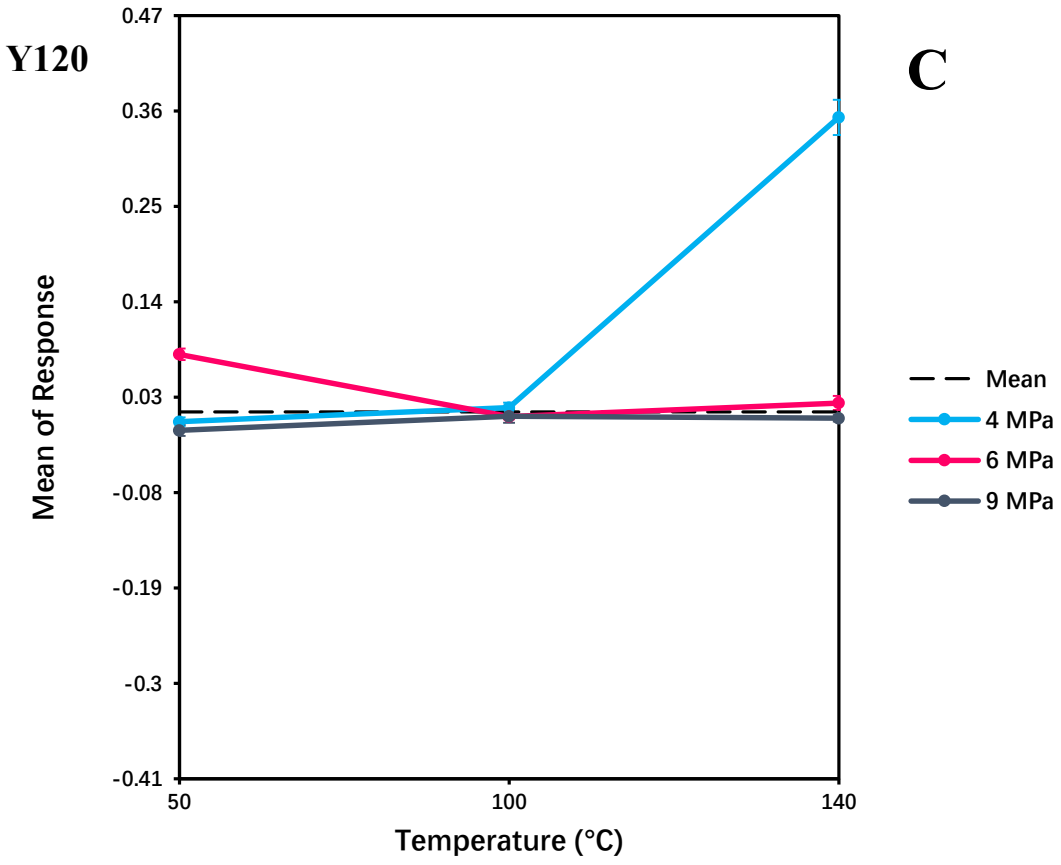
Y120
C
0.47
0.36
0.25
0.14
0.03
-0.08
-0.19
-0.3
-0.41
Mean of Response
50
100
140
Temperature (°C)
Mean
4 MPa
6 MPa
9 MPa

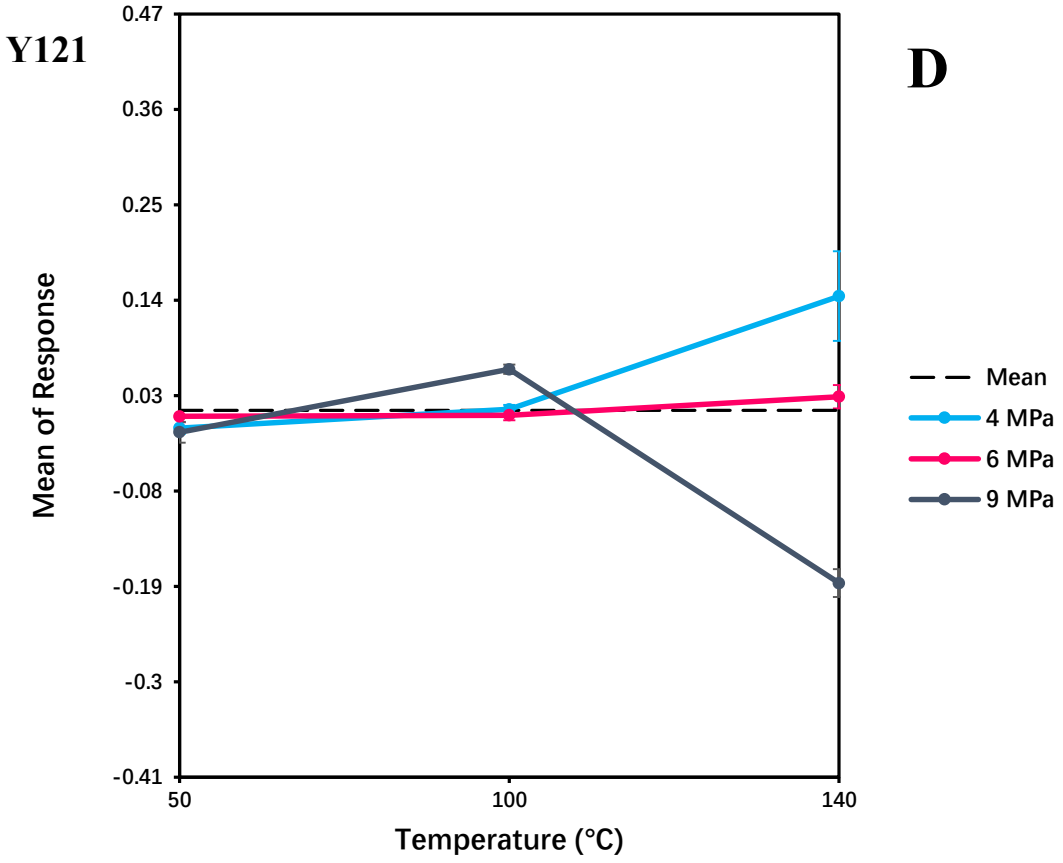
Y121
D
0.47
0.36
0.25
0.14
0.03
-0.08
-0.19
-0.3
-0.41
Mean of Response
50
100
140
Temperature (°C)
Mean
4 MPa
6 MPa
9 MPa

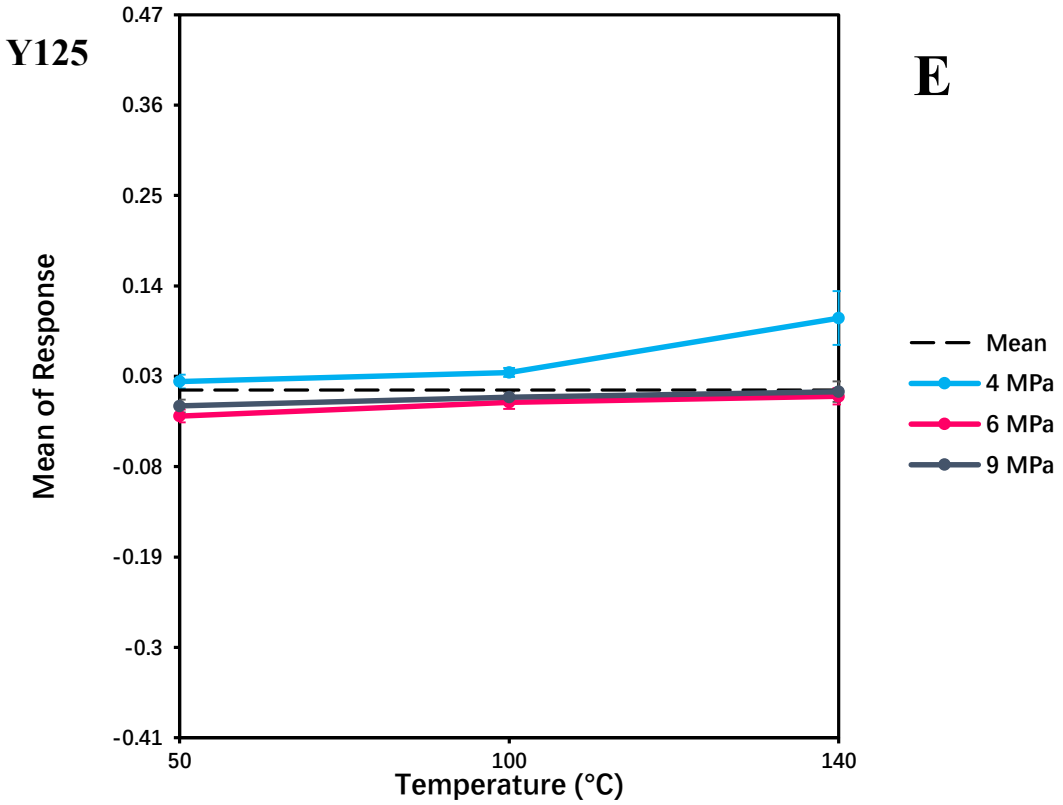
Y125
E
0.47
0.36
0.25
0.14
0.03
-0.08
-0.19
-0.3
-0.41
Mean of Response
50
100
140
Temperature (°C)
Mean
4 MPa
6 MPa
9 MPa

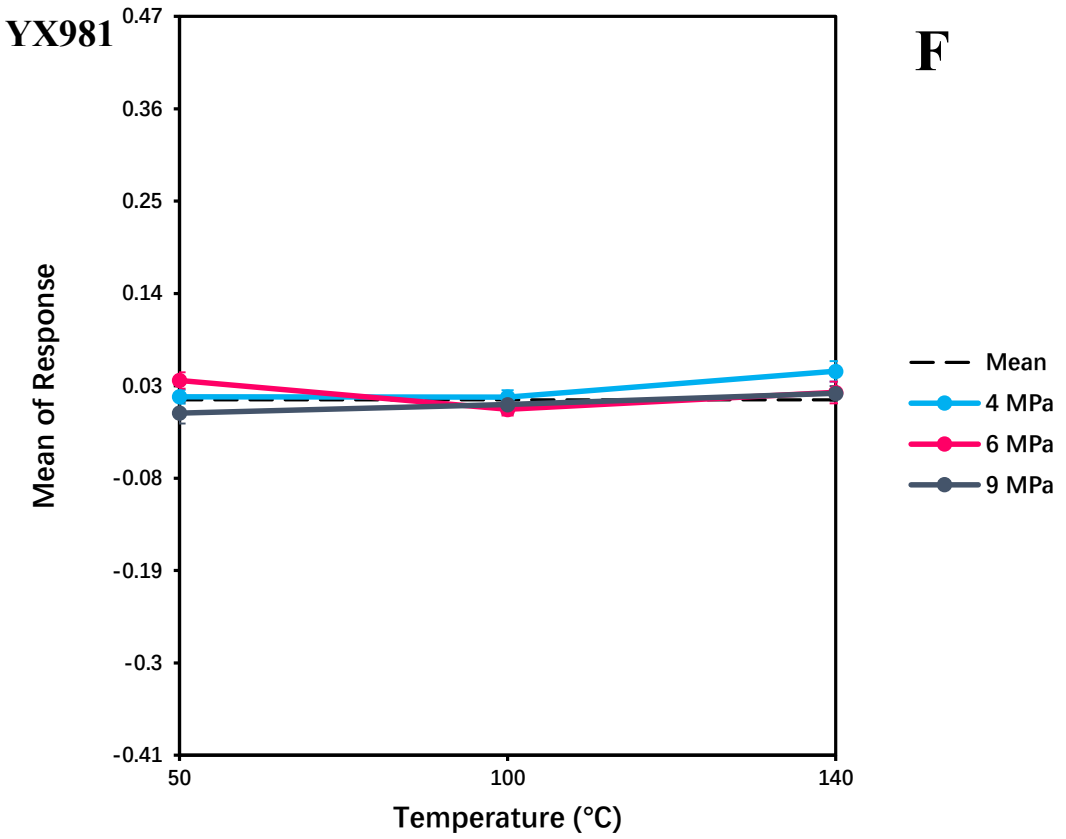

Figure 5.9 - *Interaction plot for Samples *Temperature*Pressure.*

Interaction effects between the *Samples, Temperature* and *Temprange* are shown in Figure 5.10. For samples reacted at 50 °C, their two main temperature ranges of carbonate mineral decomposition in TGA were 600-650 °C (i.e. sample *Y120* and *YX981*) and 650-700 °C (i.e. sample *Y100* and *Y121*). In terms of the temperature range 650-700 °C, it was also where carbonate deposited in sample *Y118* and *YX981* at 100 °C mainly decomposed, while for sample *Y120* at 100 °C, 700-750 °C was where carbonate mainly decomposed. Both 650-700 °C and 700-750 °C were main levels in the *Temperature* factor for carbonate mineral decomposition for *Y100* at 100 °C. More distinct phenomena of carbonate mineral decomposition were observed in interaction effects related with high temperature 140 °C. For sample *Y118* at 140 °C, a large part of carbonate was decomposed for the temperature range 600-650 °C to 850-900 °C except 700-750 °C. Such phenomena of carbonate mineral decomposition were also detected in sample *Y120* at 140 °C, at temperature range 600-650 °C and 750-800 °C. Less carbonate mineral decomposition were observed in sample *Y121* (mean of *diff* was about 0.15 at temperature range 600-650 °C), *YX981* (mean of *diff* was about 0.06 at temperature range 650-700 °C) and *Y125* (mean of *diff* was about 0.12 at temperature range 600-

650 °C and mean of *diff* was about 0.17 at temperature range 850-900 °C) at 140 °C.

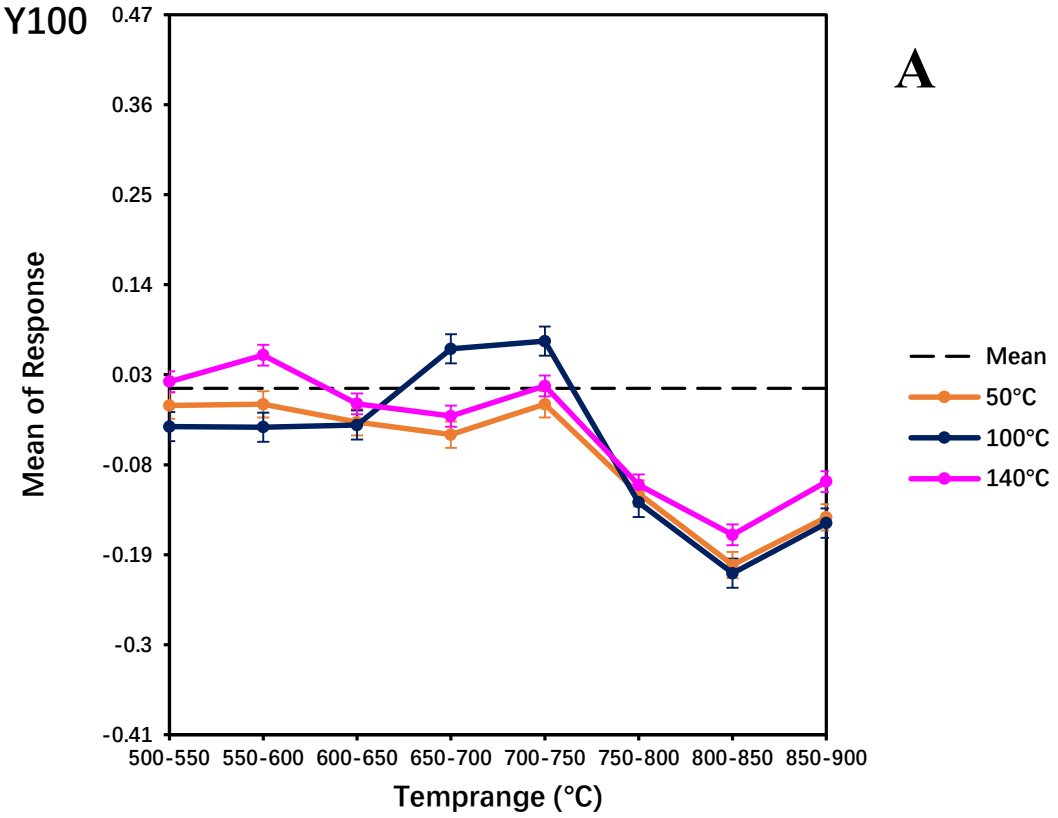

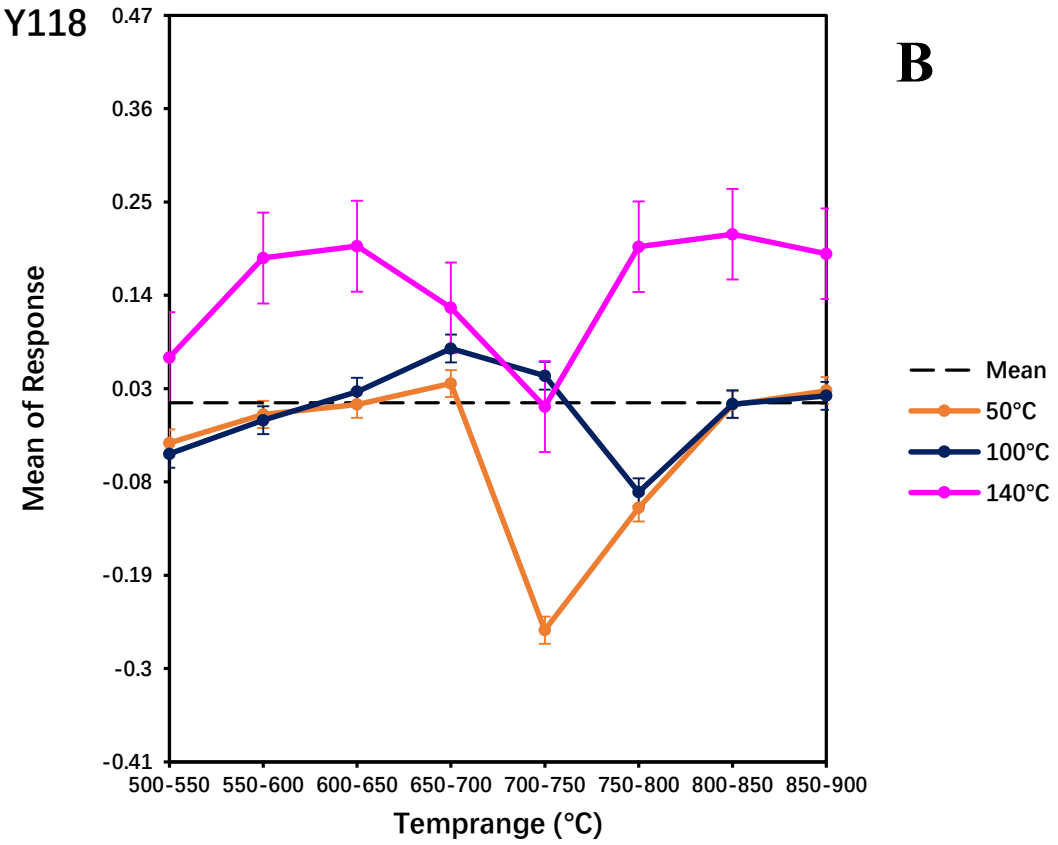

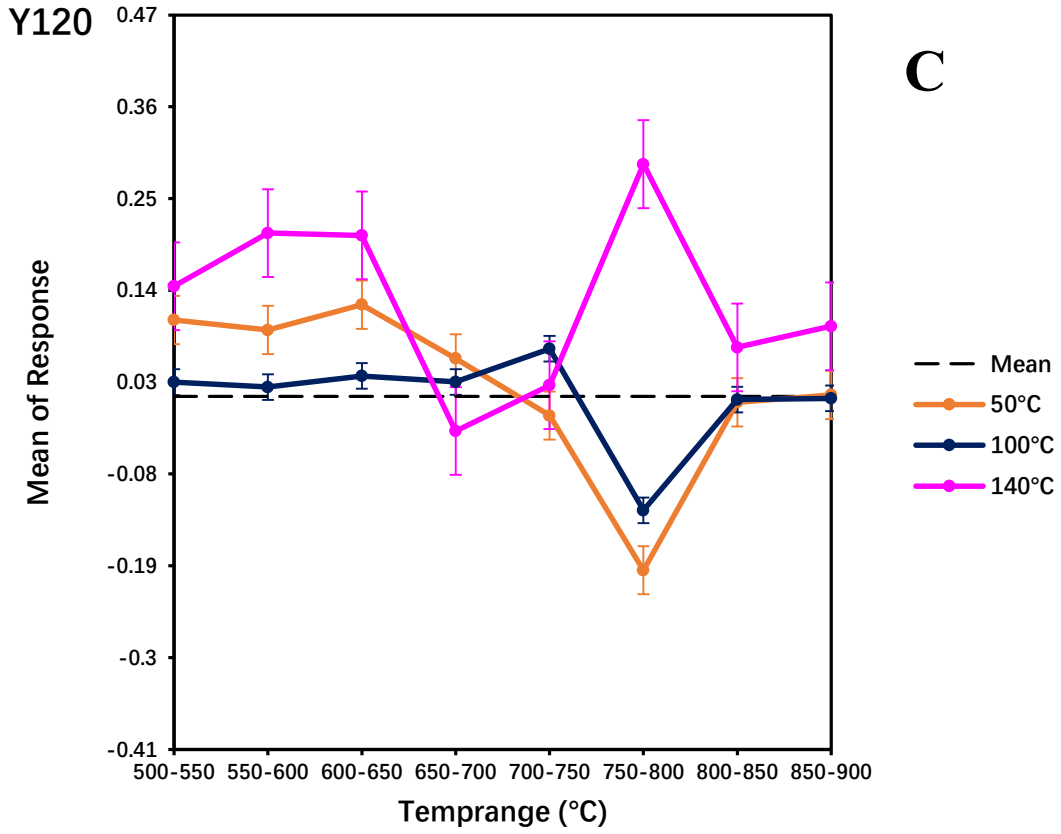
Y120
C
0.47
0.36
0.25
0.14
0.03
-0.08
-0.19
-0.3
-0.41
Mean of Response
500-550
550-600
600-650
650-700
700-750
750-800
800-850
850-900
Temprange (°C)
Mean
50°C
100°C
140°C

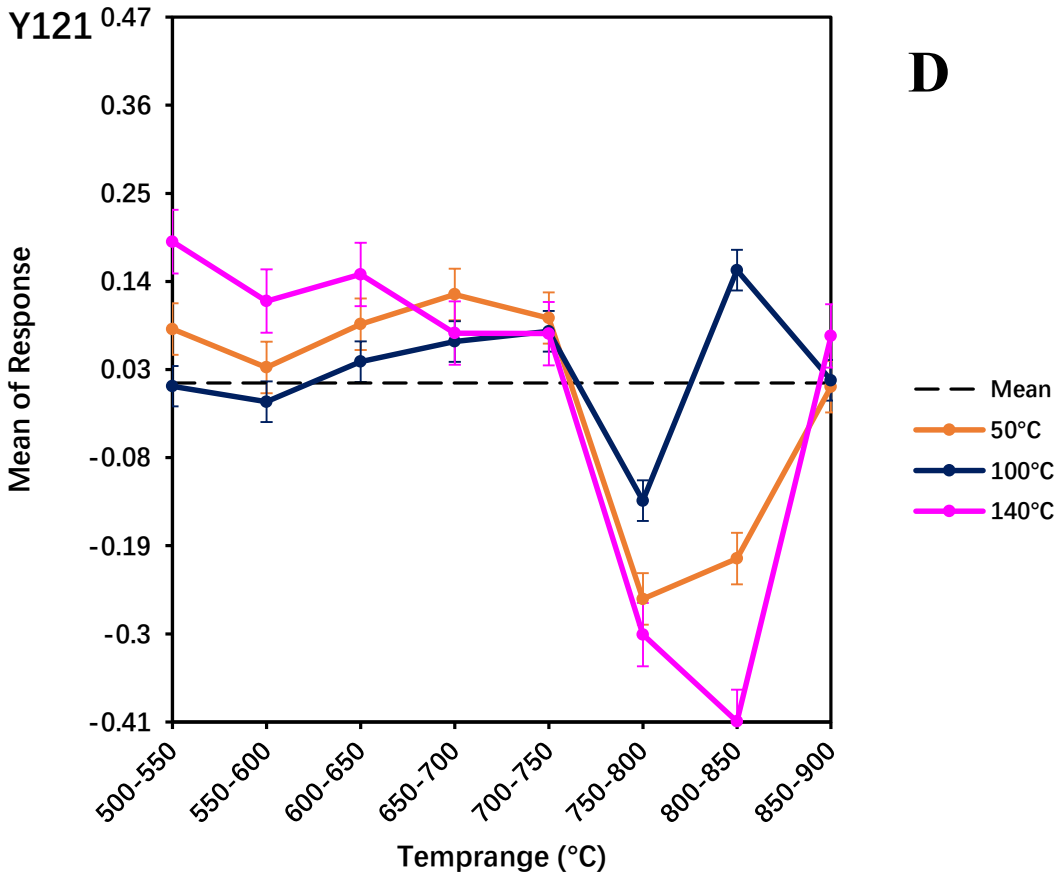
Y121
D
0.47
0.36
0.25
0.14
0.03
-0.08
-0.19
-0.3
-0.41
Mean of Response
500-550
550-600
600-650
650-700
700-750
750-800
800-850
850-900
Temprange (°C)
Mean
50°C
100°C
140°C

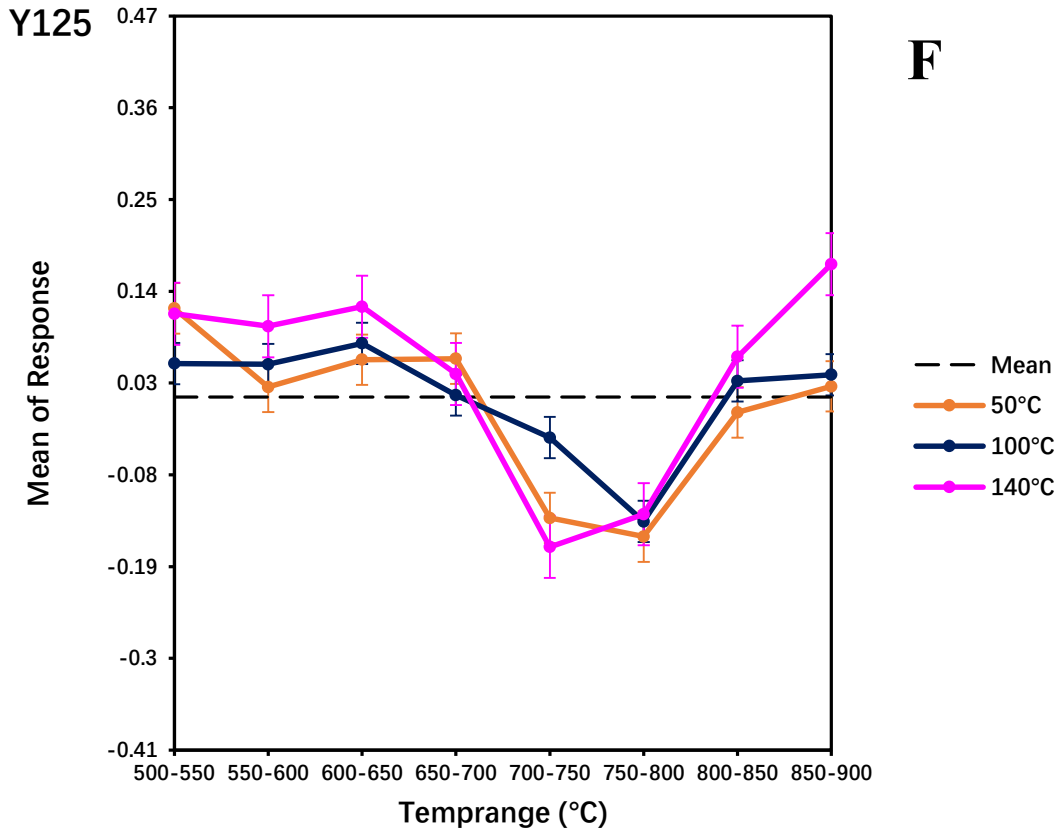

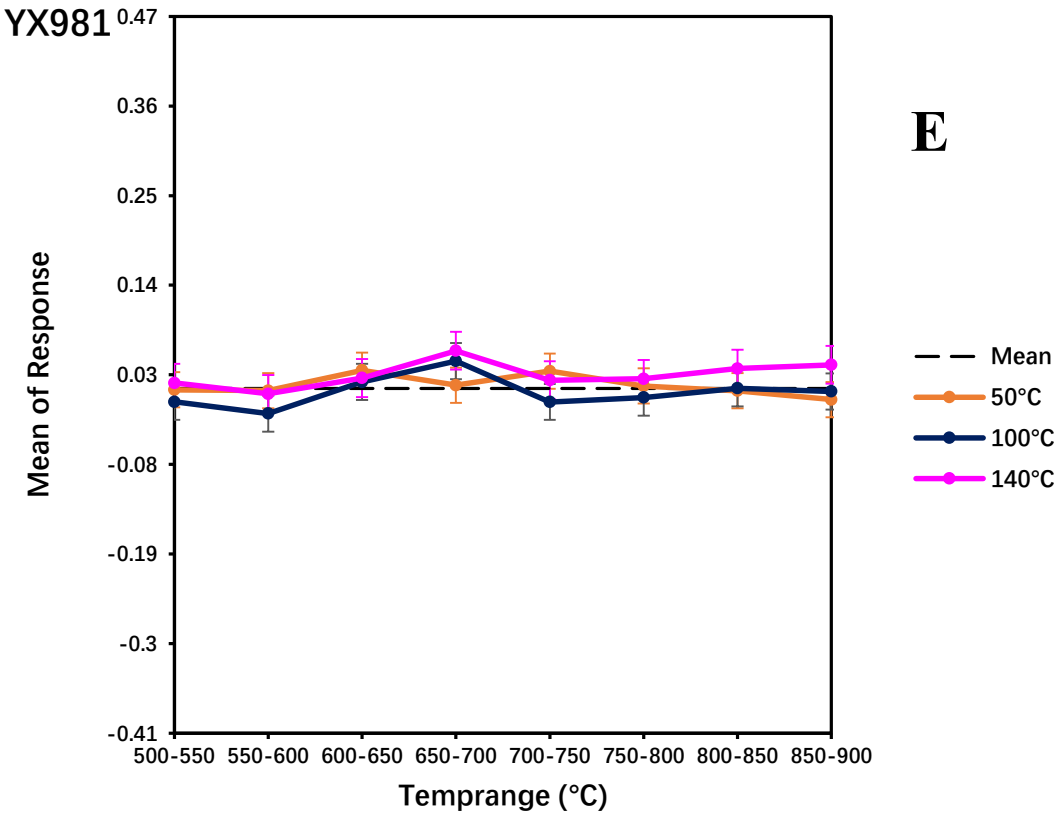

Figure 5.10 - *Interaction plot for Samples *Temperature* Temprange.*

Through analysis of interaction effect with *Sample, Temperature* and *Pressure*, it can be concluded that in physical simulation experiment, carbonation, i.e. CO_2 mineral trapping phase, was greater in *Sample Y118* and *YX981*, and increased with temperature but not linear positive correlated with pressure. While to practical storage work, real reservoir conditions should be considered, including temperature, pressure, rock texture and mineral composition.

5.3.2 Implications of controlling factors of CO_2 mineral trapping process in practical storage work based on physical simulation experiment results

1) Temperature

Temperature, a primary condition in a real reservoir, is the vital effect on chemical reaction equilibrium and reaction rate (Barclay and Worden, 2009; Steefel and Lasaga, 1994; Wang et al., 2020). According to chemical kinetics, temperature rising is possible to promote calcite precipitation by increasing reaction rate of feldspar dissolution (Yuan et al., 2015a; Yuan et al, 2019; Zhu et al, 2009), as suggested by the much more extensive feldspar dissolution phenomena in the experiments conducted at 100 and 140 °C. Data acquired from TGA indicates that carbonation was promoted as temperature rose (Table 4.4). For examples, the amount of carbonation of sample *YX981* in experiment of ① 50℃ was 0.47% in average (0.77% in *140℃-4MPa*, 0.64% in *140℃-6MPa*, 0.59% in *140℃-9MPa*), ② 100℃ was 0.54% in average (0.57% in *100℃-4MPa*, 0.53% in *140℃-6MPa*, 0.53% in *140℃-9MPa*), ③ 140 ℃ was 0.67% in average (0.77% in *140℃-4MPa*, 0.64% in *140℃-6MPa*, 0.59% in *140℃-9MPa*) (Table 4.2). In this case, 100 ℃ and 140 ℃ were conducive for CO_2 mineral trapping in comparison with conditions at 40 ℃. In practical geological storage site, formation temperature reflects the depths. In Bohai Bay, East China, 100 ℃ occurs in 2500 m depth approximately, while 140 ℃ occurs in 3500 m depth approximately (geothermal gradient is 35℃ / km). Therefore, reservoirs deeper than 2500 m in Bohai Bay have potential to be favorable mineral trapping site.

2) CO_2 Pressure

CO_2 partial pressure determines CO_2 solubility, leading to changes in chemical equilibrium, and high pCO_2 (over 50 atm, approximately 5.07 MPa) is likely to promote mineral trapping, as an

inhibitor of carbonate mineral reactivity (Pokrovsky et al., 2009; Giles, 1986). While in physical simulation experiments in this study, system pressure was equal to pCO_2. Data acquired from TGA indicates that carbonation did not increase obviously with pressure in physical simulation experiments (Table 4.2). Even supercritical CO_2 (over 31.3 ℃,7.3 MPa) did not bring an obvious positive effect. This lack of significant effect is likely to be rationalized as too high pCO_2 used in this physical simulation experiments. It is possible that chemical reaction in term of carbonate precipitation is not sensible to change in pCO_2 at high pCO_2 condition - over about 5.07 MPa (Pokrovsky et al., 2009). Another possible explanation is that the impact of pressure/pCO_2 is not conspicuous in short-term experiment as both calcite precipitation and feldspar dissolution are going forward in slow rate. According to numerical simulation of geological CO_2 storage conducted by Wang, the precipitation rate of calcite reached the equilibrium within 300 years (Wang et al., 2020). While high pressure had potential to promote solubility trapping and sequester CO_2 in formation water as solute though possibly not stable as minerals (Xu et al., 2017).

3) Rock textures

Though porosity in the present physical simulation experiments could not be taken into consideration as experiment material was rock powder, it is necessary to consider the effect of porosity in actual geological reservoirs. Abundant pores are able to provide not only pathways for CO_2 to flow but also space for chemical reaction to process (Steefel et al., 2013). Therefore, on the basis of silicate content, porosity is also possible to affect CO_2 geological storage in sandstone reservoir (Jun et al., 2013). Quantitative mineral compositional analysis shows that unreacted sample in decreasing order of surface porosity are *Y125* (26.86 %), *Y100* (20.18 %), *YX981* (16.12 %), *Y120* (16.12 %), *Y118* (8.97 %), *Y121* (5.39 %) (Table 4.2). Low porosity makes *Y118* and *Y121* unlikely to be selected as potential CO_2 geological storage site. Therefore, in practical storage work, reservoirs with low porosity (less than 10% like *Y118* and *Y121*) should be excluded.

4) Mineral composition

Feldspar dissolution played a vital role in chemical reaction equilibrium of the process where CO_2 transferred into calcite (Lu et al, 2013; Tutolo et al, 2015; Wang et al., 2020). Due to high equilibrium constant, abundant feldspars are needed in geological storage site. It is possible for

feldspar dissolution to promote CO_2 geological storage in two ways: 1) by consuming acid and releasing suitable cations (K^+, Na^+, Al^{3+}) to enable carbonation to go forward; 2) by creating secondary dissolution pores to allow for CO_2 physical trapping (Figure 4.1). Quantitative mineral compositional analysis shows that unreacted sample in decreasing order of silicates content are *Y118* (54.61 %), *YX981* (50.94 %), *Y120* (49.24 %), *Y100* (49.23 %), *Y121* (45.45 %), *Y125* (37.77 %) (Table 4.2). The higher the silicate mineral content, the better the material basis for storing CO_2. According to results of TGA (Table 4.5), for example, carbonate precipitation was identified in seven of nine reacted *YX981* samples (silicates content of 50.94 %), while only one of nine reacted *Y125* samples (silicates content of 37.77 %). Though silicates content of *Y118* is the highest among six samples, the poor porosity (8.97 %) make the great material basis not useful as it seems to be (Table 4.2). In general, high silicates content can make a reservoir ideal for CO_2 mineral storage only if the reservoir is provided with high porosity.

5) Favorable geological site for CO_2 mineral storage in Bonan sub-sag, Bohai Bay

Combining the previous results and discussion, an ideal geological site for CO_2 mineral storage in Bonan Subsag should meet four conditions:

① formation water rich in Ca^{2+};

② buried depth over 2500 m;

③ porosity of reservoir over 10%;

④ mineral composition of reservoir rock rich in silicate minerals.

Sample *YX981*, $Es3^2$ member, lithic arkose, well sorted, fine sand (grain size 0.21 mm, approximately), in rounded roundness, 2726.10 m deep, rich in content of silicate mineral (50.94 %), high porosity (16.12 %), performed the greatest CO_2 mineral trapping potential (carbonate precipitation was identified in seven of nine reacted *YX981* samples) among 6 sandstone samples in physical simulation experiments. In conclusion, by the research based on combination of analyses, a favorable geological site for CO_2 mineral storage in arkosic reservoir with $CaCl_2$ – type formation water in Bonan subsag, Bohai Bay, was identified to be arkosic reservoir rich in silicate mineral and pores in $Es3^2$ member represented by sample *YX981*.

6. Conclusion

6.1 Principle findings and conclusion

Precipitation of carbonate minerals in subsurface porous rocks is an important and a safe pathway to capture and storage CO_2 in K-feldspar-rich sandstone reservoir in Bonan Subsag, East China. Analyses unreacted sample and reacted samples from the physical simulation experiments indicate that within the chemical reaction processes of $CaCl_2$ saline water-sandstones system:

1) the injection of excess CO_2 is possible to dissolve feldspar and primary carbonate mineral but still precipitate calcite eventually (Section 5.2).

2) the chemical process is controlled by mineral composition content of sandstone and system temperature. Higher silicates content and higher temperature (over 100 °C) promote the reaction to go forward. Though pressure did not play an important role in CO_2 mineral trapping, high pressure was still a possible positive effect on CO_2 physical trapping. Meanwhile, rock texture should be considered in practical CO_2 storage site, as pores are possible to provide space for CO_2 to flow and store (Section 5.3).

3) sandstone sample *YX981* collected from member $Es3^2$, 2726.10 m is the most favorable sample compared with others as CO_2 geological storage site in Bohai Bay, East China.

6.2 Study limitations

The following is a summary of limitations of experiment design and analysis across this study.

1) The duration of physical simulation experiments could be extended. Given that both of dissolution of feldspar and precipitation of carbonate were slow processes, duration as 96 hours was considered enough to allow the reaction to proceed fully, leading low amount of carbonate precipitation.

2) The duration of physical simulation experiments could be varied. Without changing other

experiment conditions (sample, temperature and pressure), reacted samples with different durations would be possible to show different stages of the reaction. Within the scope of this project decision has to be made to focus experiments on some and not other factors.

3) The pressure applied in physical simulation experiments should be reduced. High pCO_2 (over about 5.07 MPa) is possible to lead carbonate precipitation to be not sensible anymore to change of pCO_2 (Oleg et al., 2009), while two even higher pressure conditions (6 MPa and 9 MPa) were used in this study.

4) Analyses of physical simulation experiments would more comprehensive if all reacted samples were analyzed by SEM and EDS. Due to the restriction on the use of instruments, only representative reacted samples were analyzed by SEM and EDS.

6.3 Further work

Based on this study, necessary work to be done in the future should include:

1) As an improvement based on this study, long-term physical simulation experiments with different conditions (duration and pressure) should be key in future work. As study limitation parts noted above, duration should be extended and varied, while pressure should be reduced. Therefore, four durations should be set to one week, two weeks, three weeks and four weeks, and four pressure should be set to 3 MPa, 4 MPa, 5 MPa and 6 MPa. Besides, to simulate real geological reservoir which is porous media, rock cores should be used as experiment materials rather than rock powder.

2) With the result from long-term physical simulation experiments used as constraining conditions, several groups of numerical simulation on CO_2 saturated fluid and sandstones rich in feldspar should be conducted using software such as Geochemist's Workbench (GWB) 9.0. Numerical simulation can help in researching whether CO_2 is possible to be sequestrated stably and in large quantities on the scale of thousands of years. Further, based on the result of numerical simulation and the calculated effective porosity of the sandstones reservoir, the total CO_2

geological sequestration capacity by solubility trapping and mineral trapping may be calculated.

Appendices

Appendix A - XRD Diffractograms

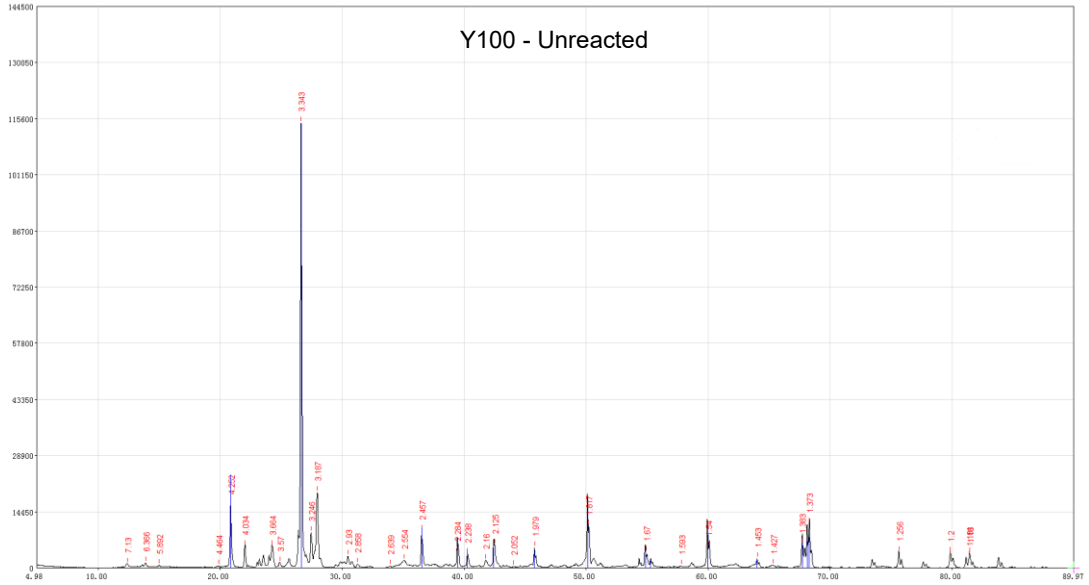

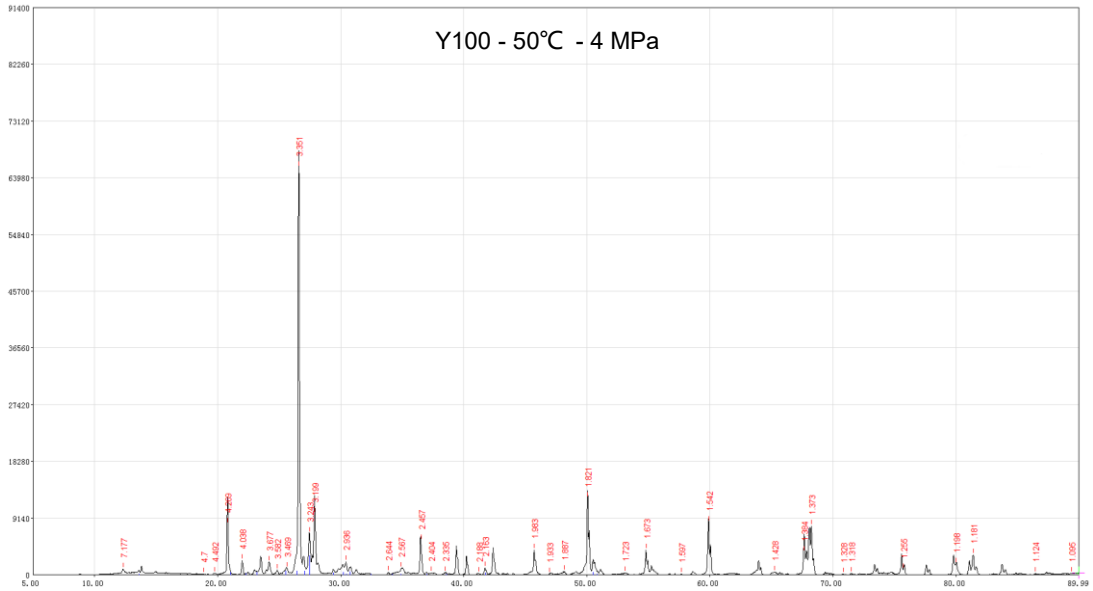

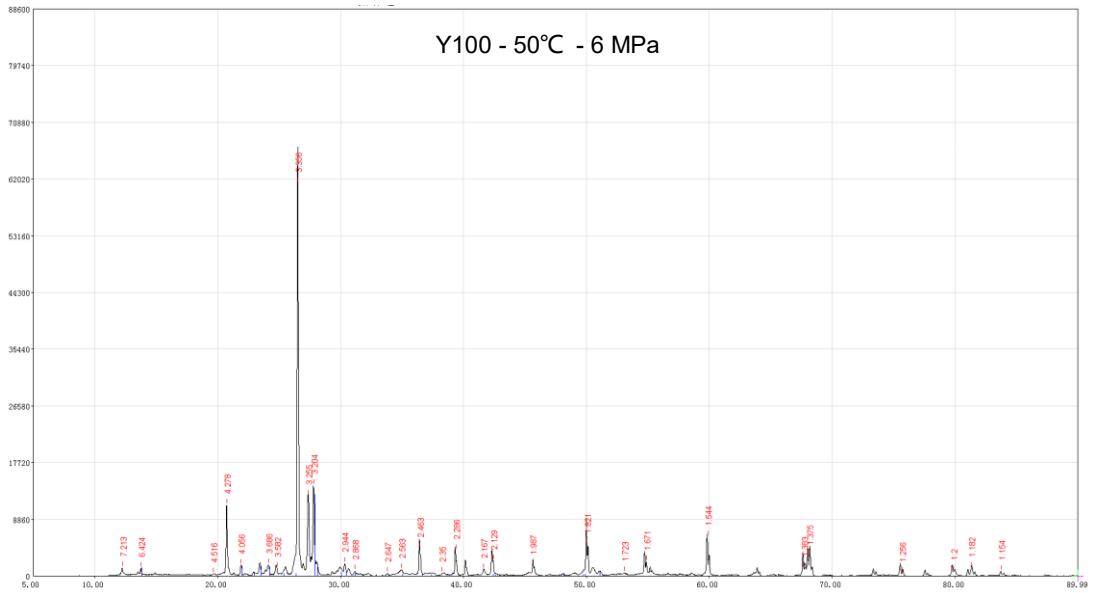
Y100 - 50℃ - 6 MPa

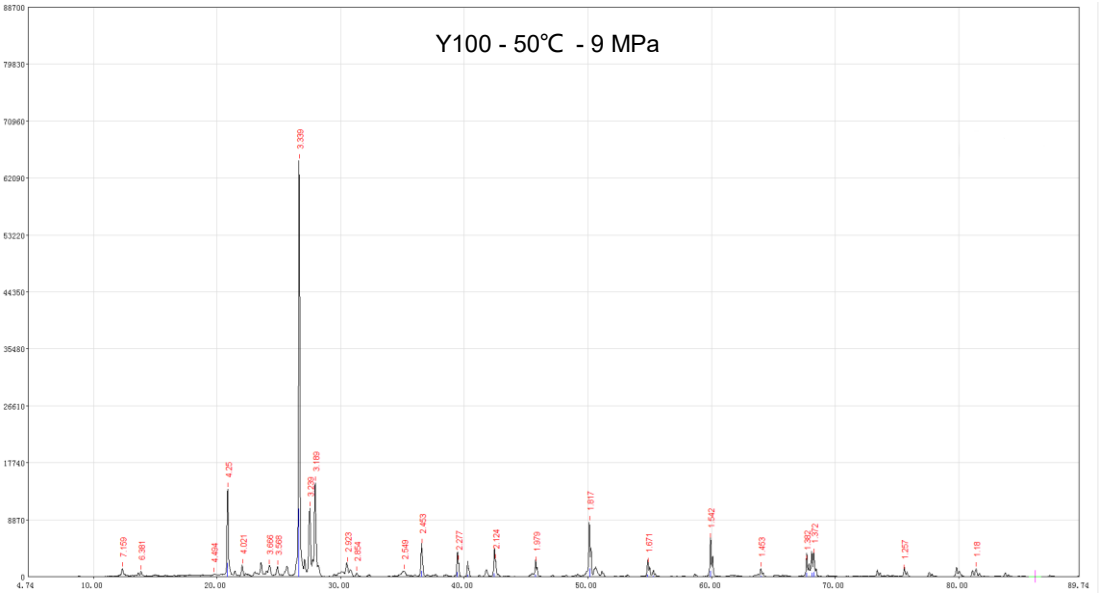
Y100 - 50℃ - 9 MPa

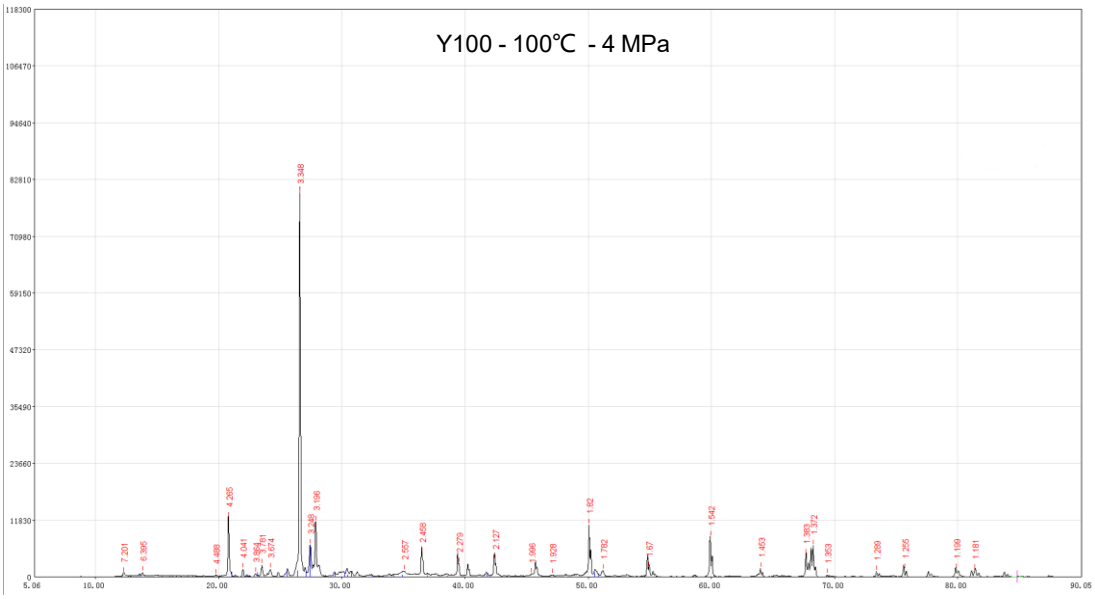
Y100 - 100℃ - 4 MPa

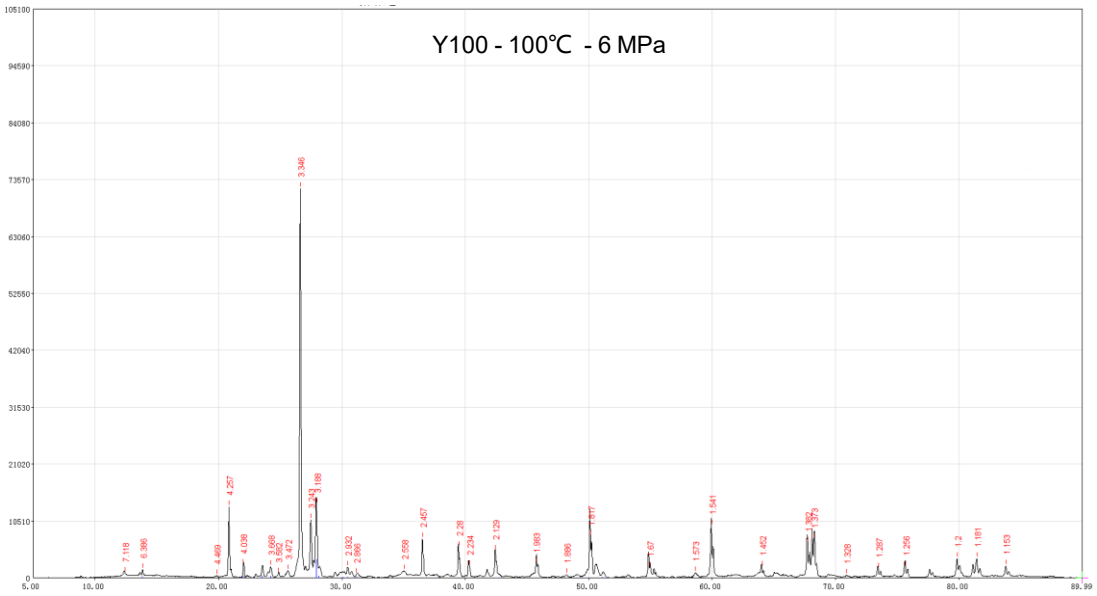
Y100 - 100℃ - 6 MPa

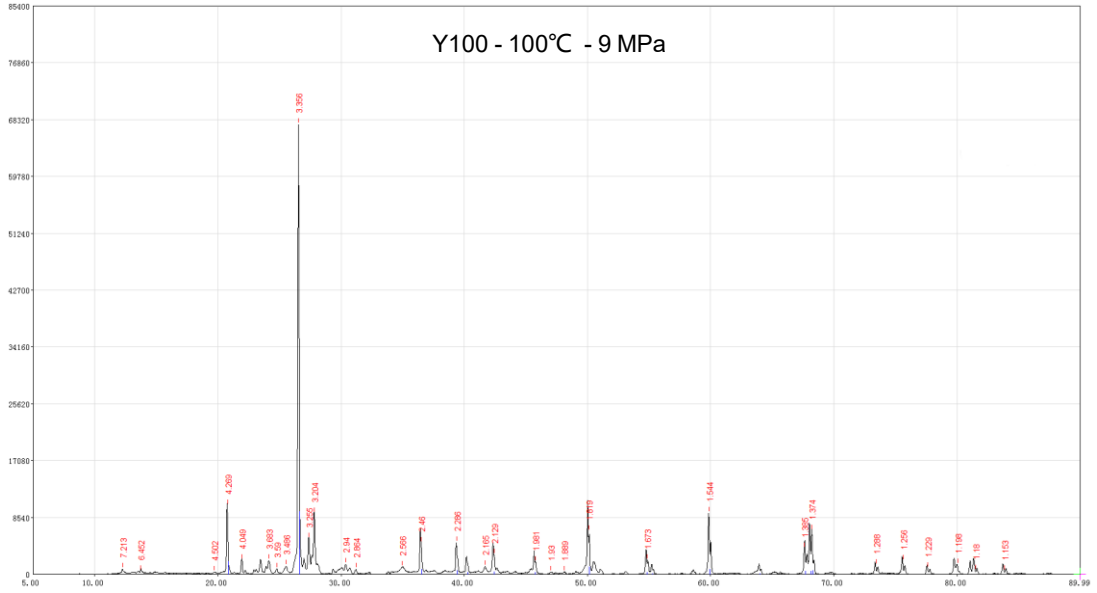
Y100 - 100℃ - 9 MPa

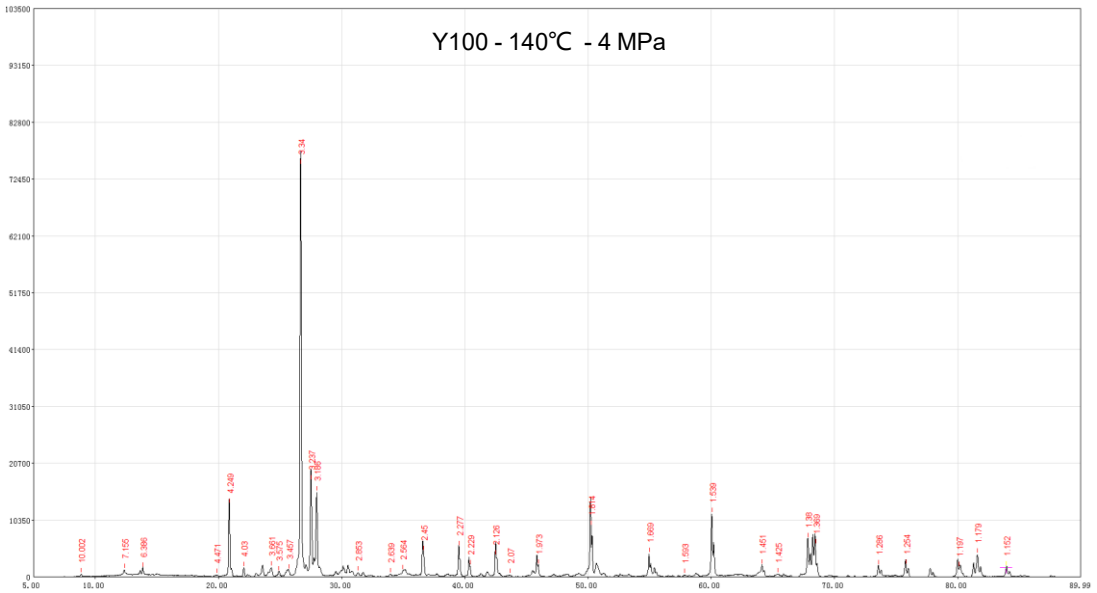
Y100 - 140℃ - 4 MPa

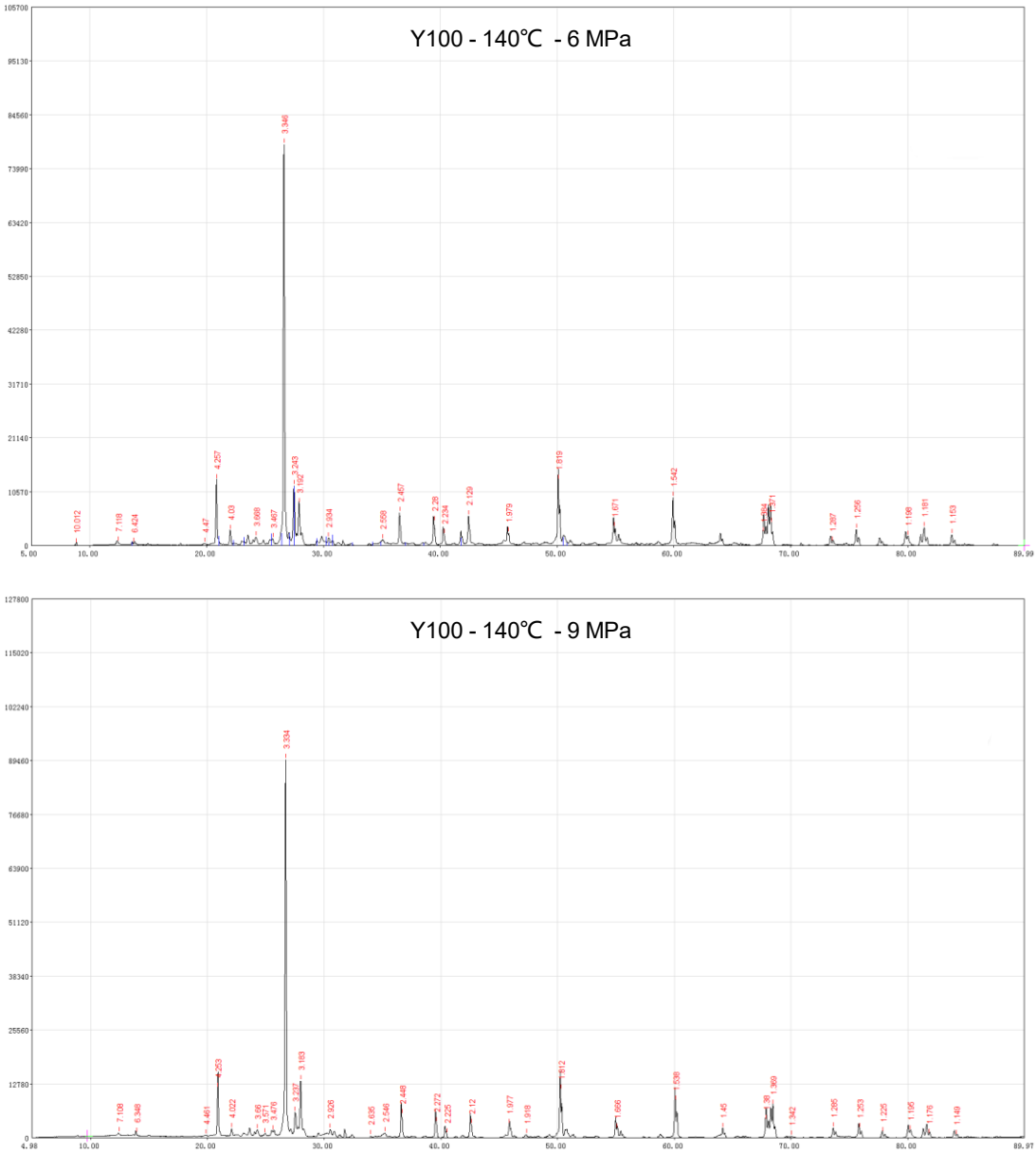

Figure 1 – *XRD Diffractograms for sample Y100*

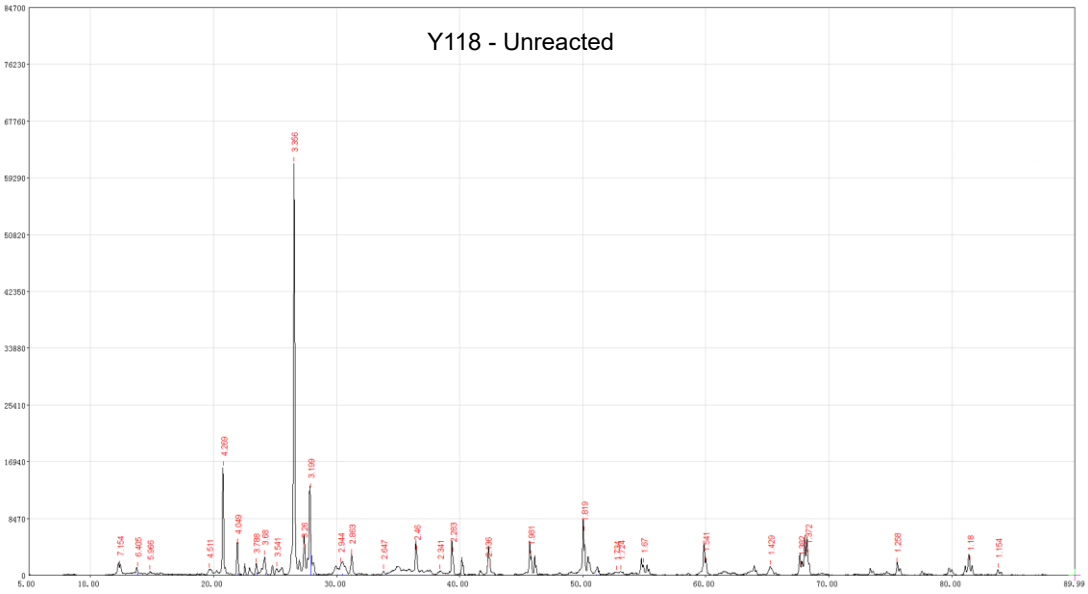
Y118 - Unreacted

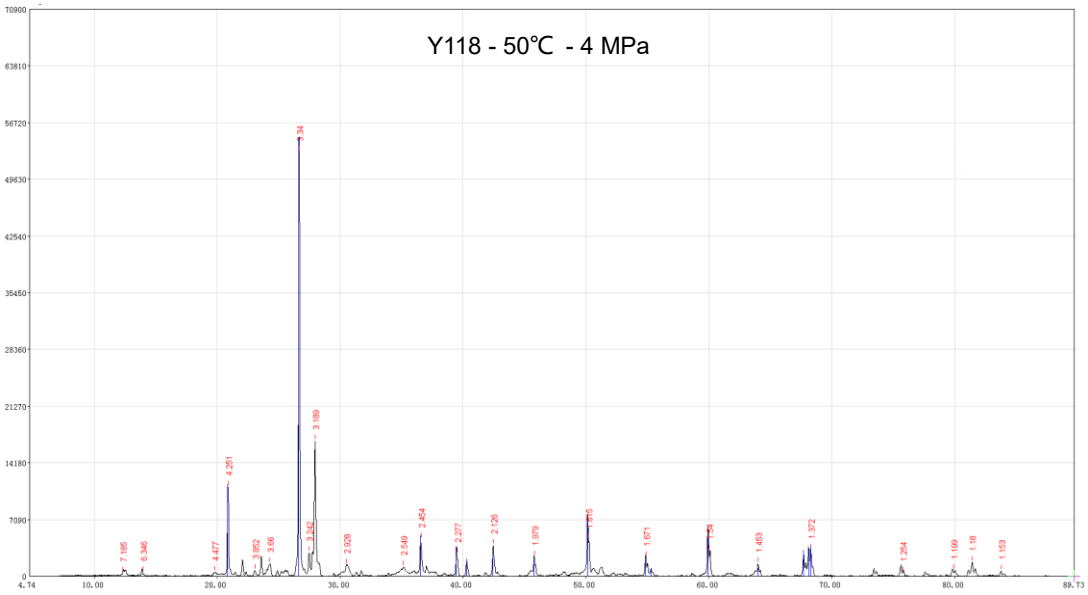
Y118 - 50℃ - 4 MPa

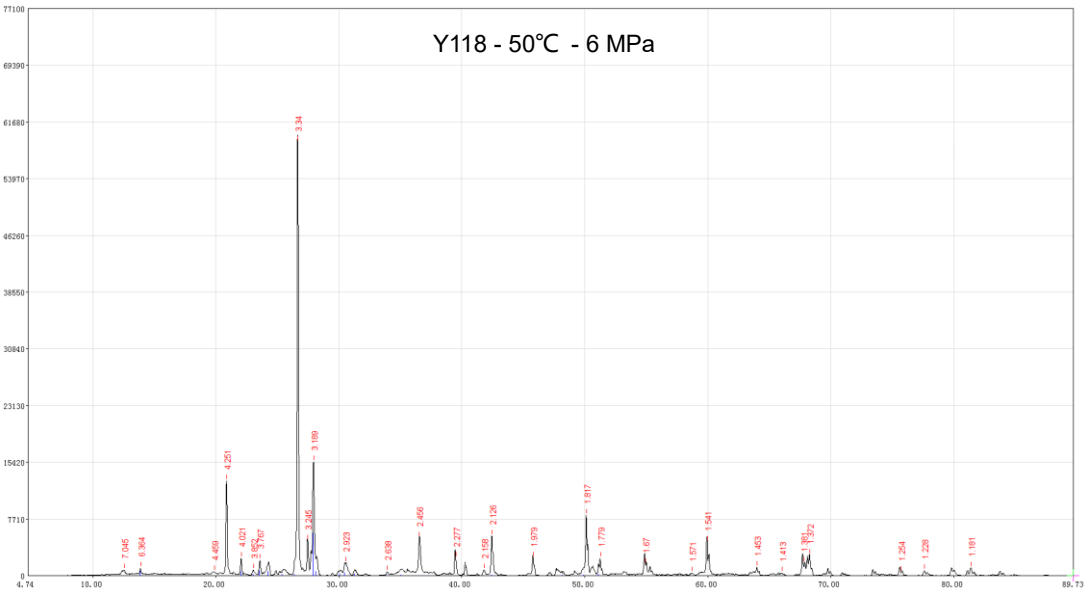
Y118 - 50℃ - 6 MPa

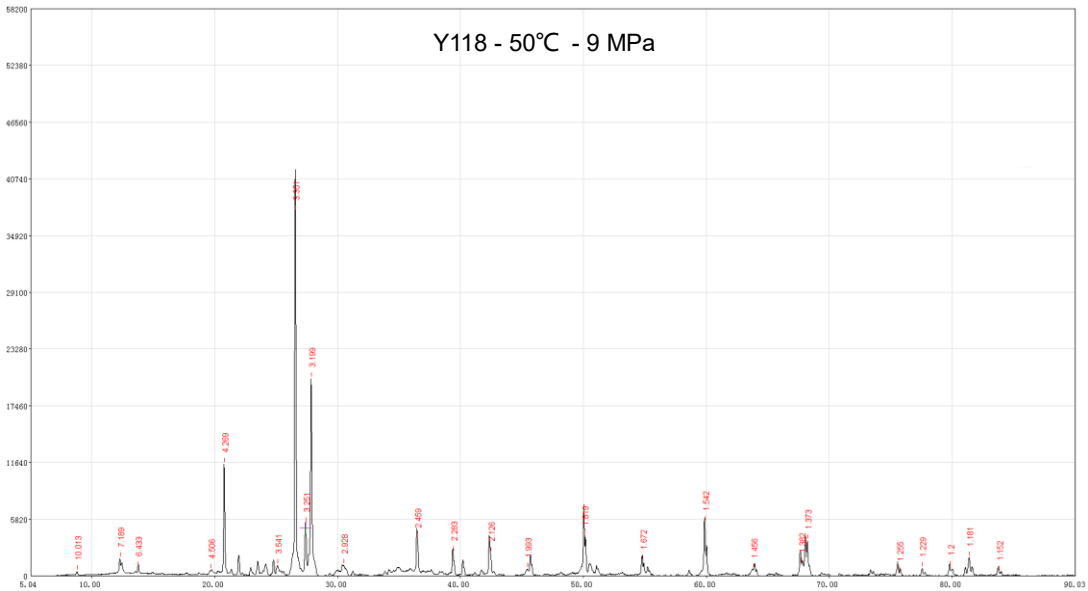
Y118 - 50℃ - 9 MPa

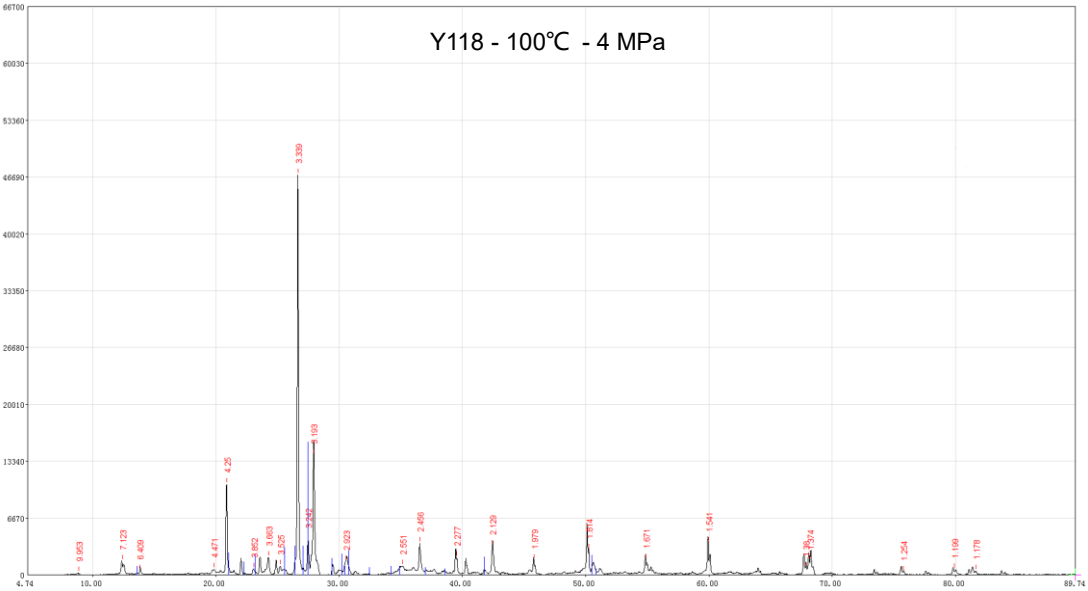
Y118 - 100℃ - 4 MPa

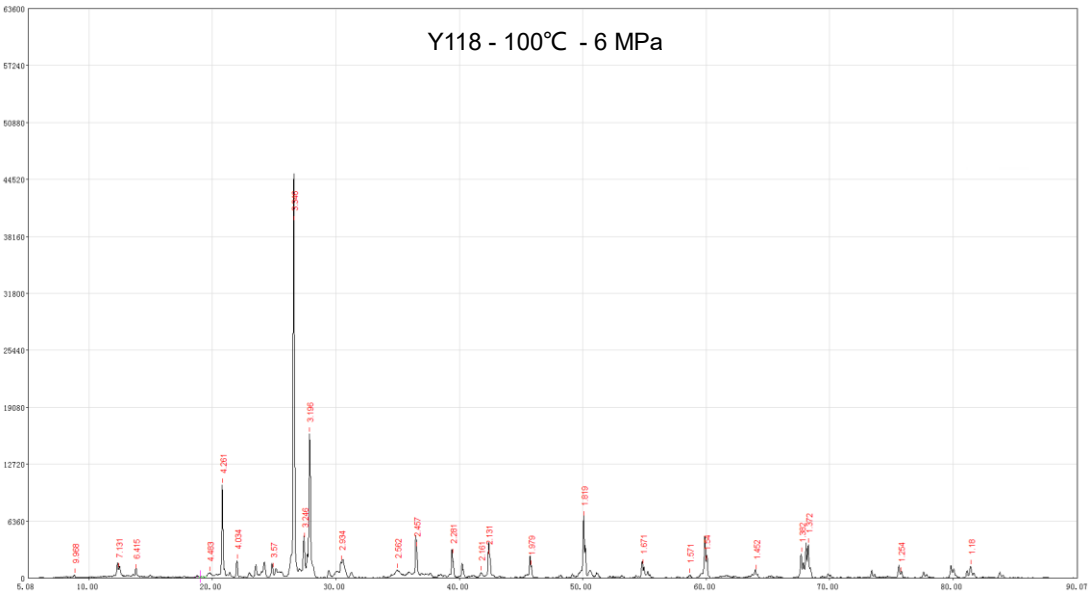
Y118 - 100℃ - 6 MPa

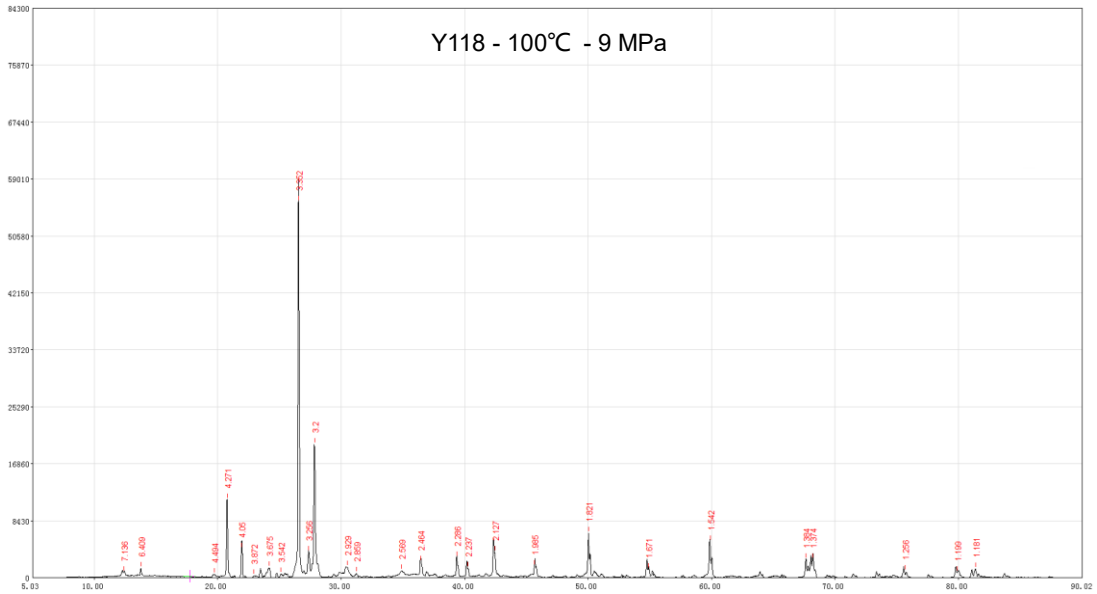
Y118 - 100℃ - 9 MPa

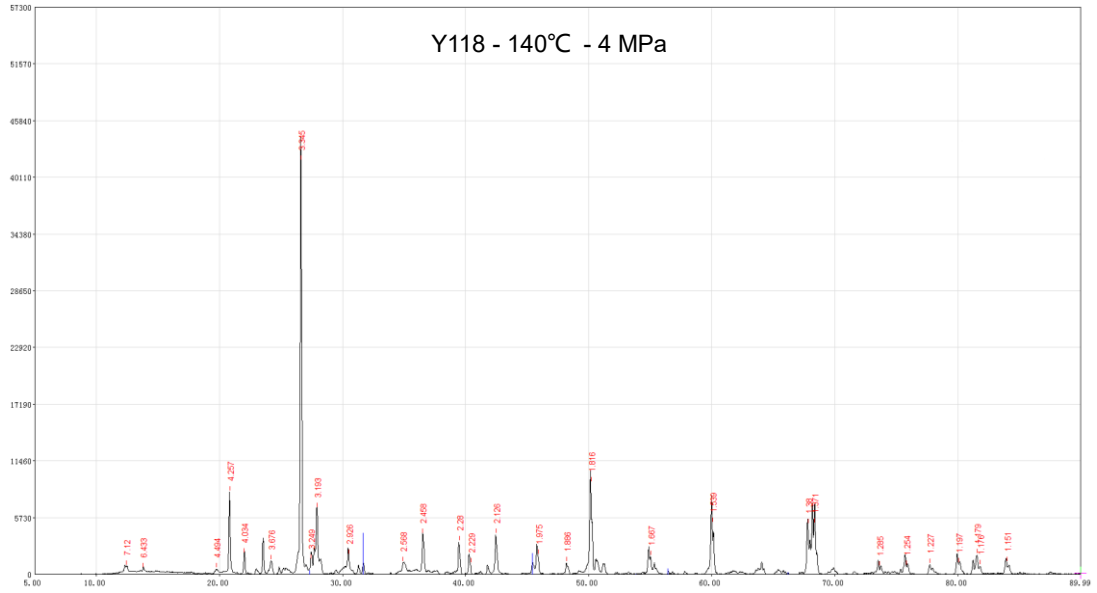
Y118 - 140℃ - 4 MPa

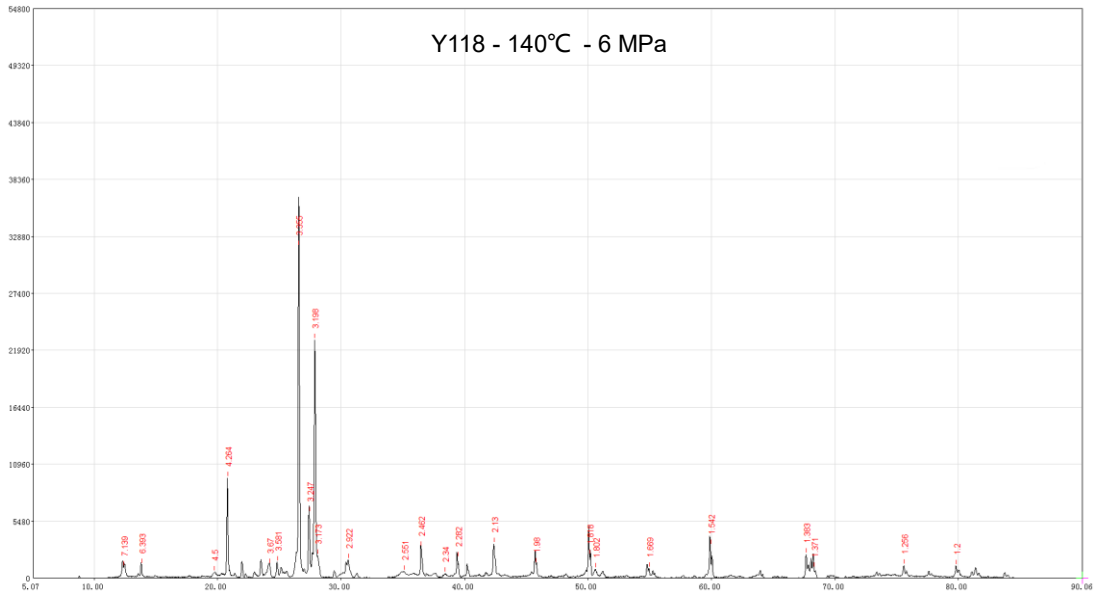
Y118 - 140℃ - 6 MPa

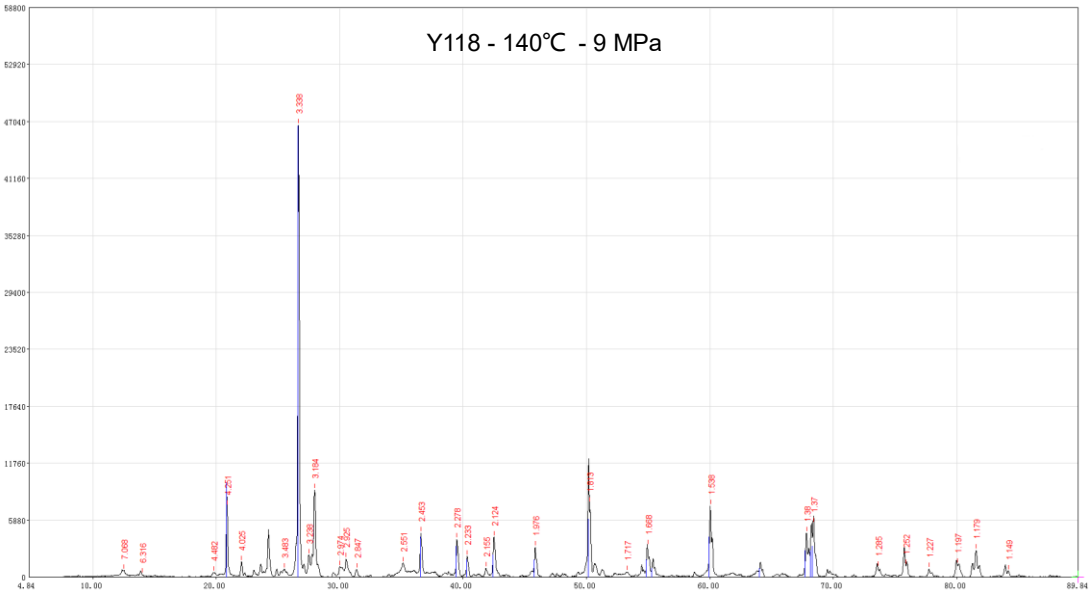

Figure 2 – *XRD Diffractograms for sample Y118*

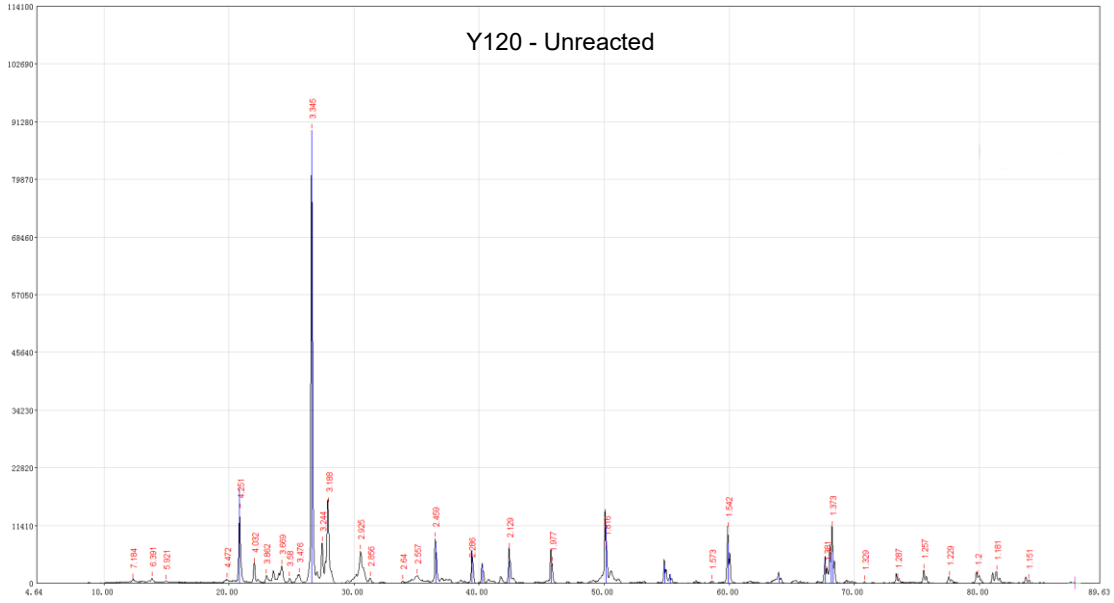

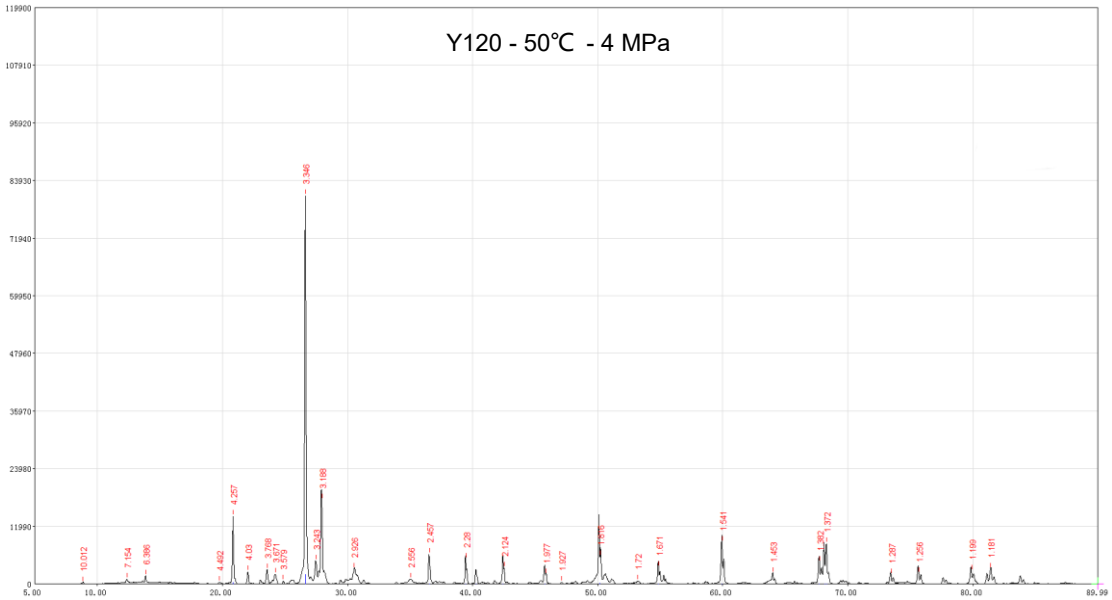
Y120 - 50℃ - 4 MPa

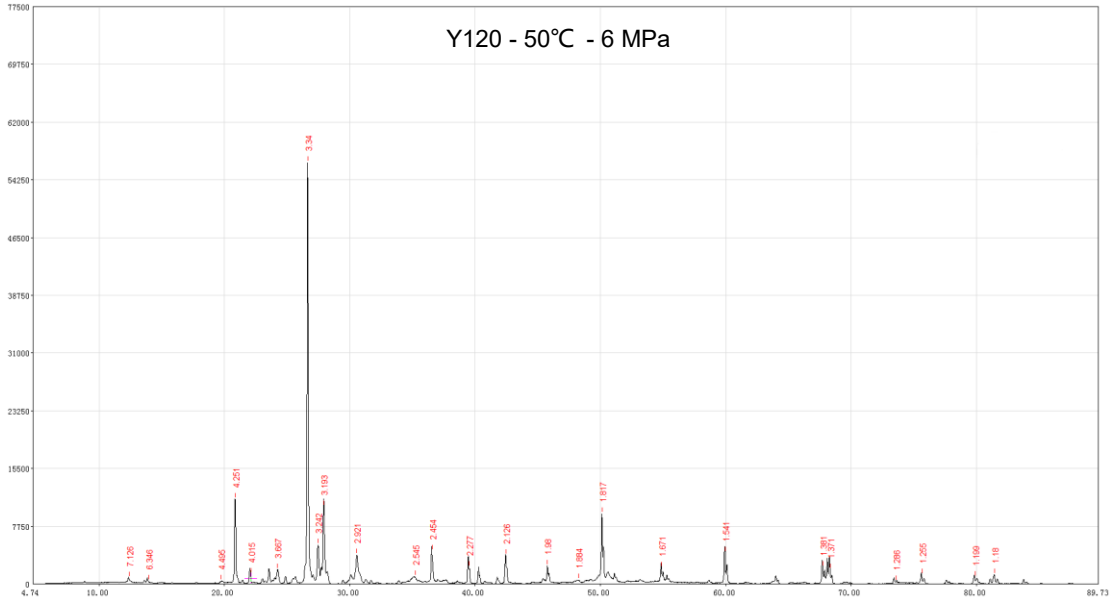
Y120 - 50℃ - 6 MPa

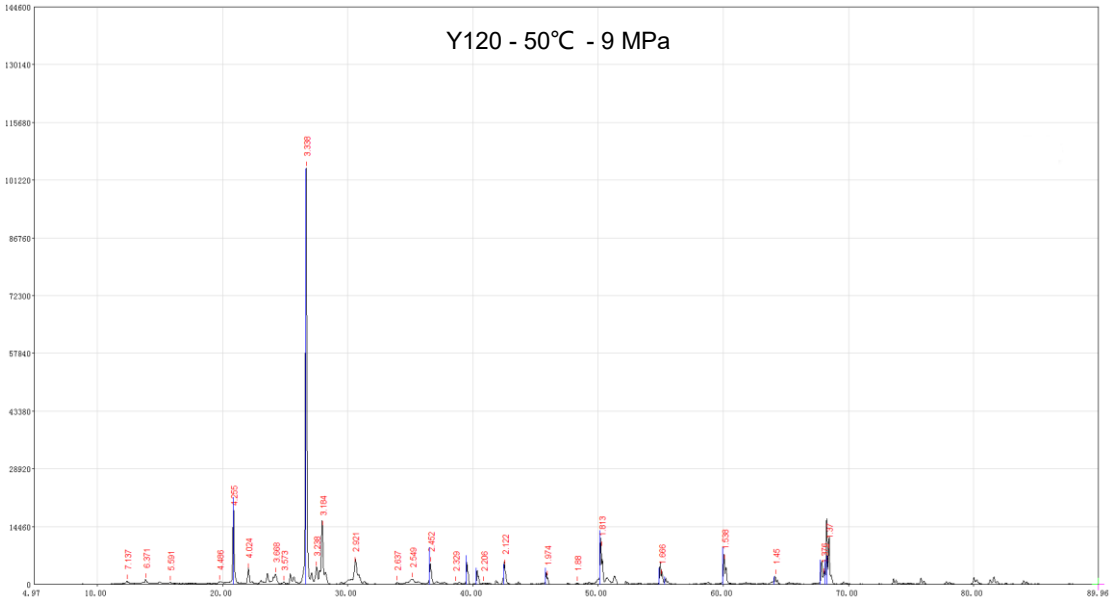
Y120 - 50℃ - 9 MPa

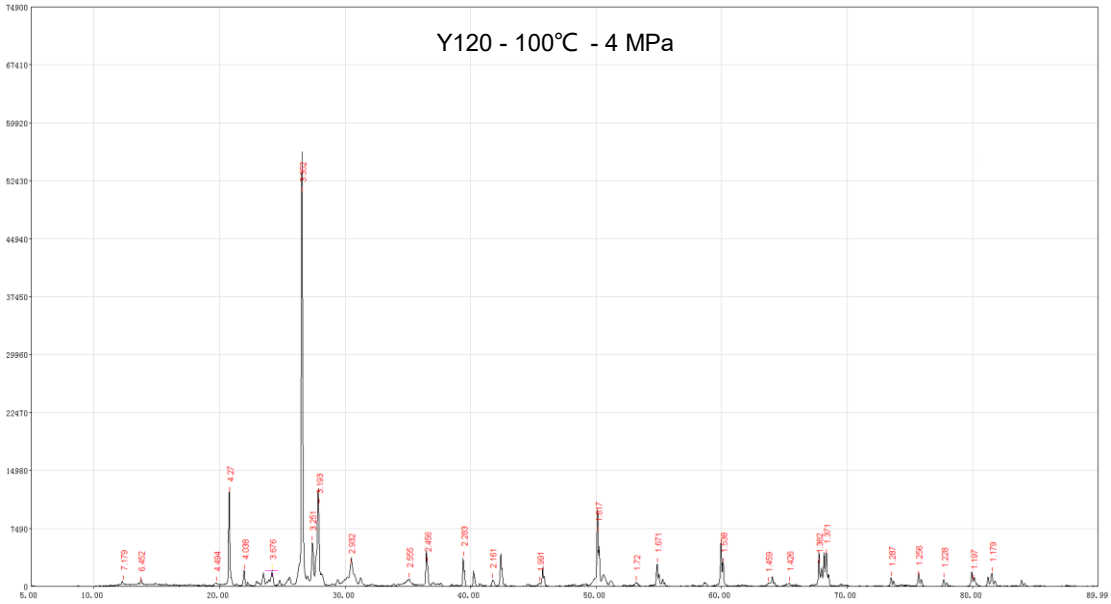
Y120 - 100℃ - 4 MPa

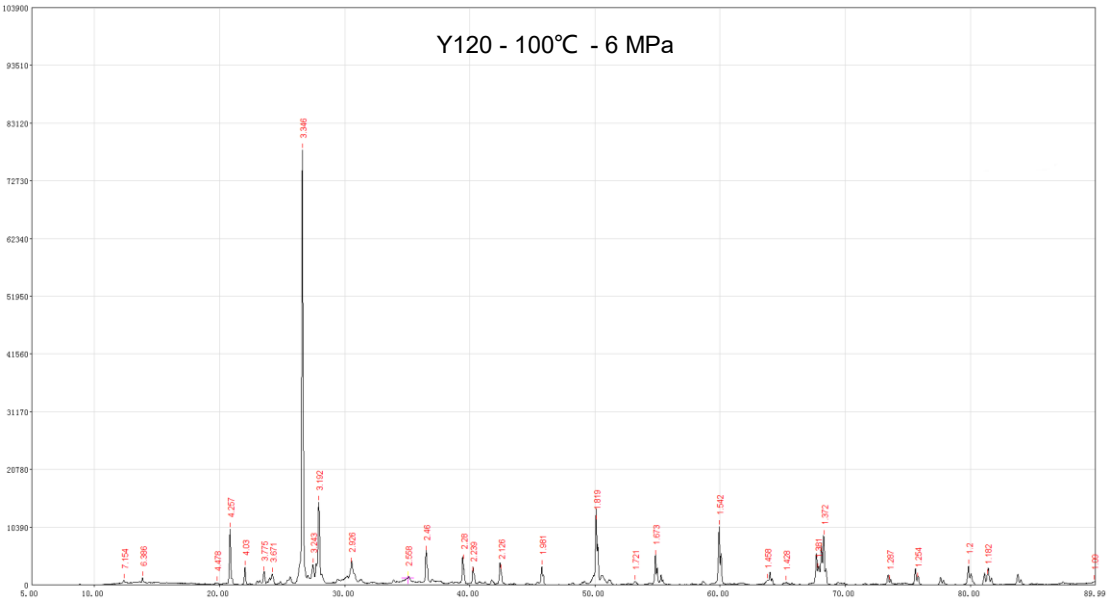
Y120 - 100℃ - 6 MPa

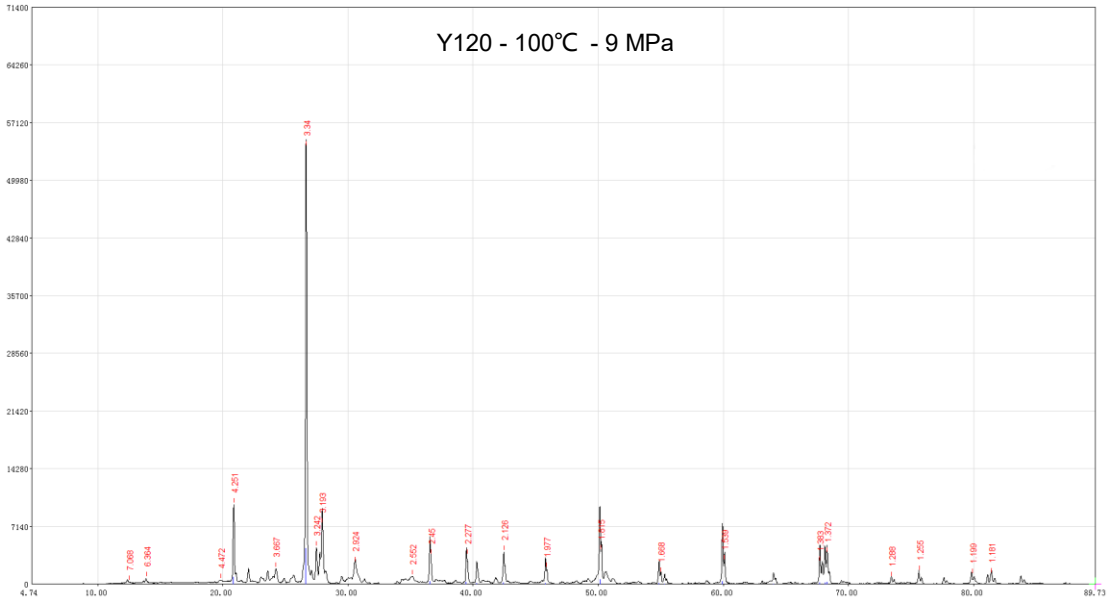
Y120 - 100℃ - 9 MPa

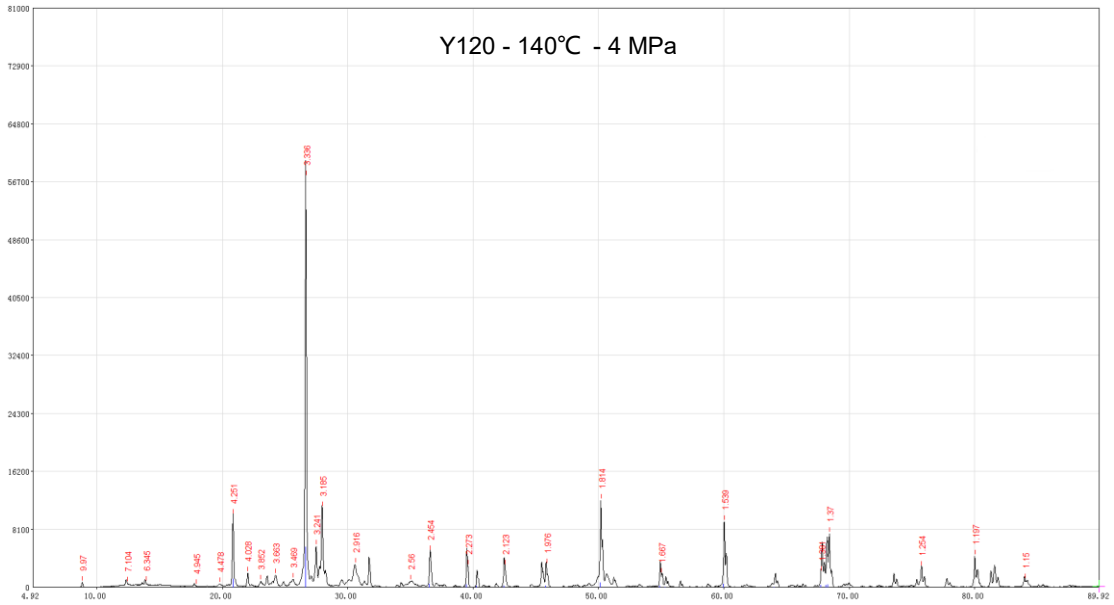
Y120 - 140℃ - 4 MPa

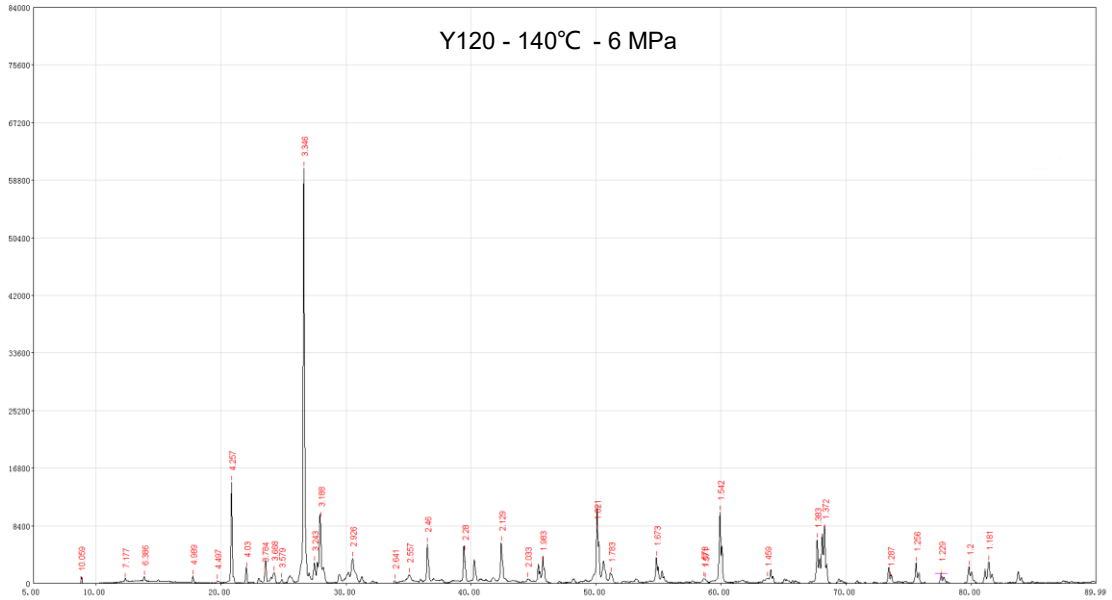
Y120 - 140℃ - 6 MPa

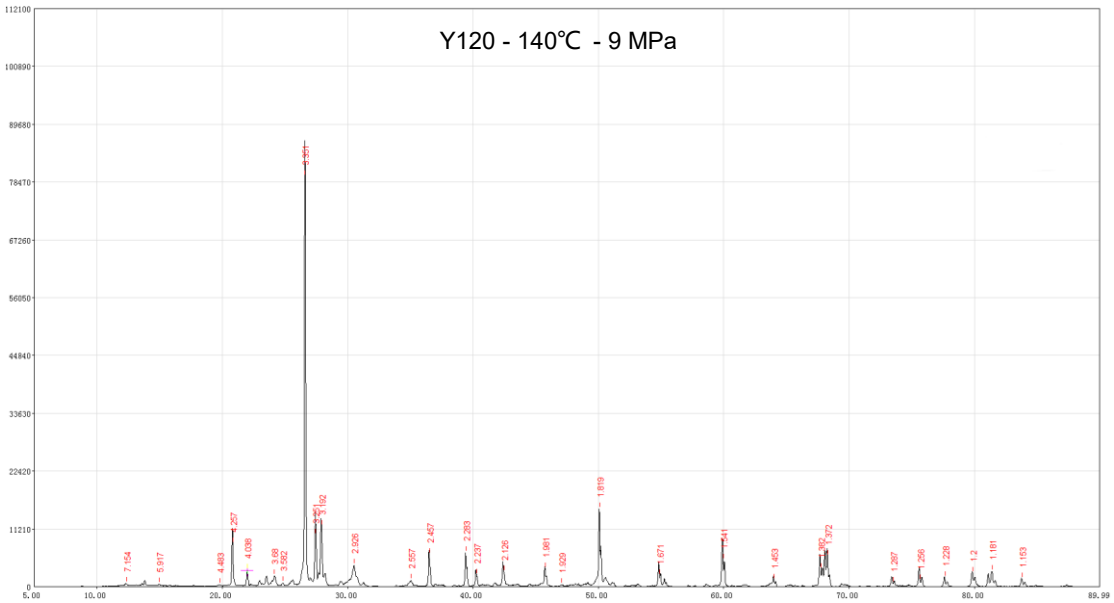
Y120 - 140℃ - 9 MPa

Figure 3 – *XRD Diffractograms for sample Y120*

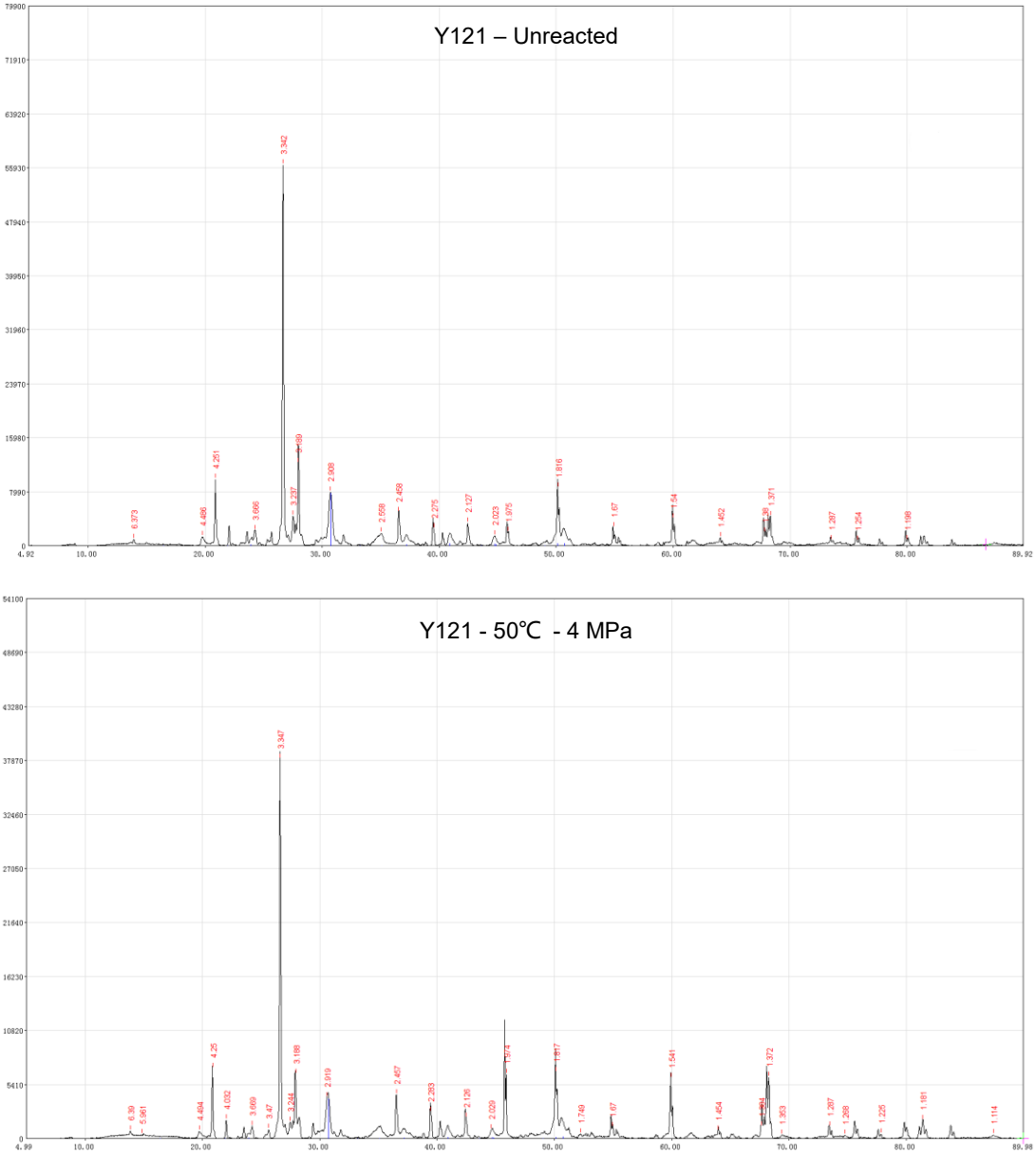

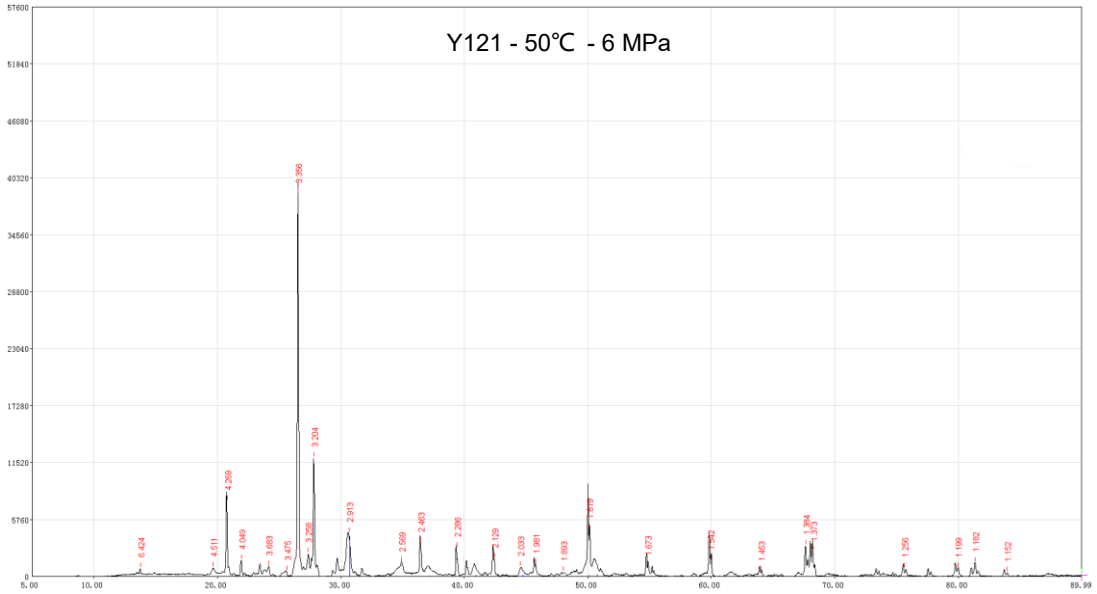
Y121 - 50℃ - 6 MPa

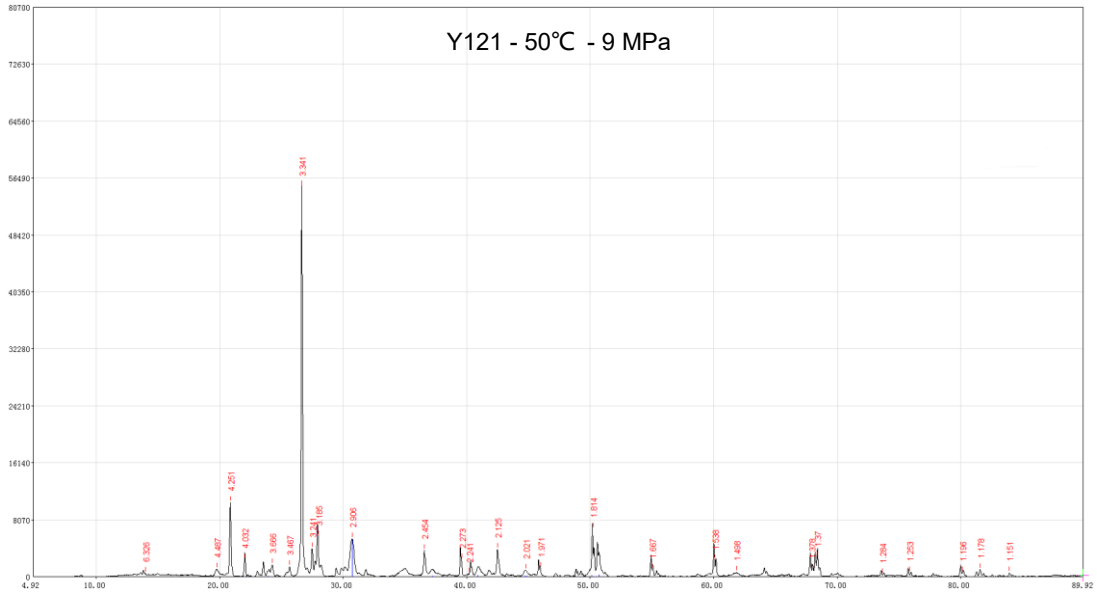
Y121 - 50℃ - 9 MPa

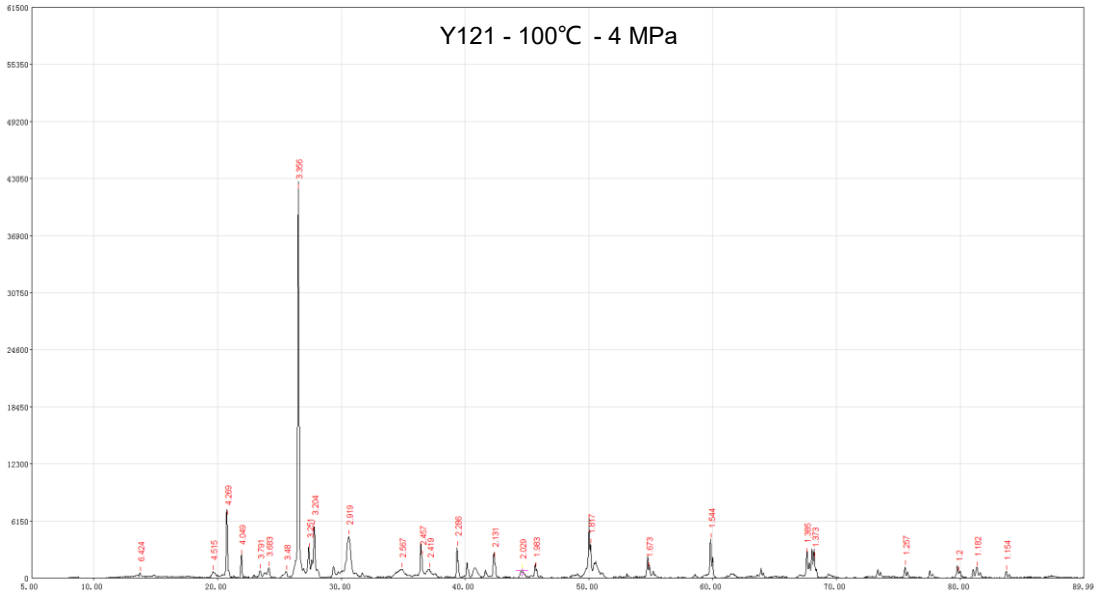
Y121 - 100℃ - 4 MPa

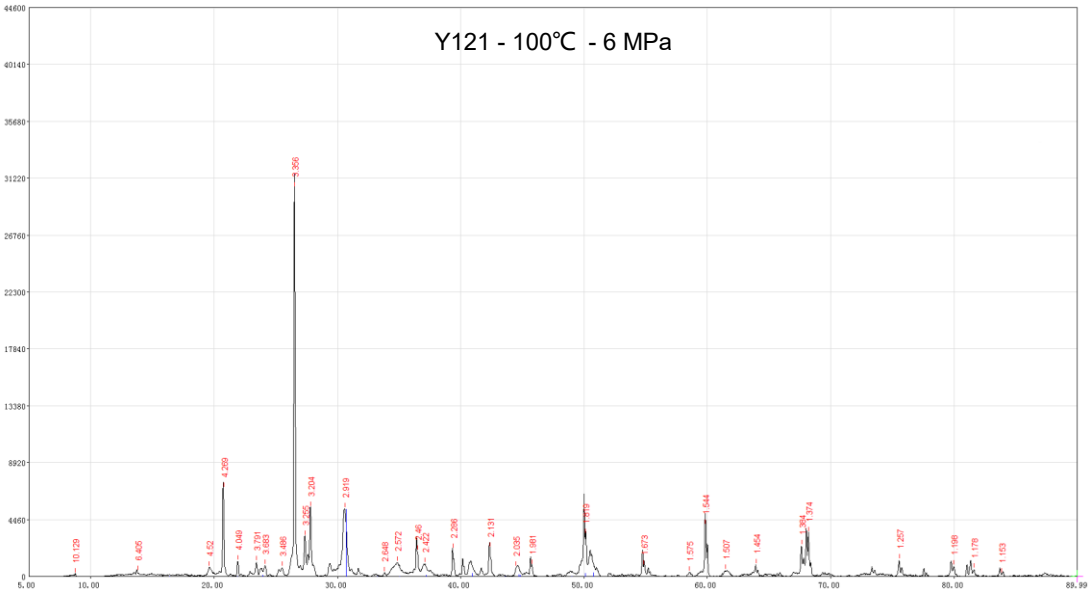
Y121 - 100℃ - 6 MPa

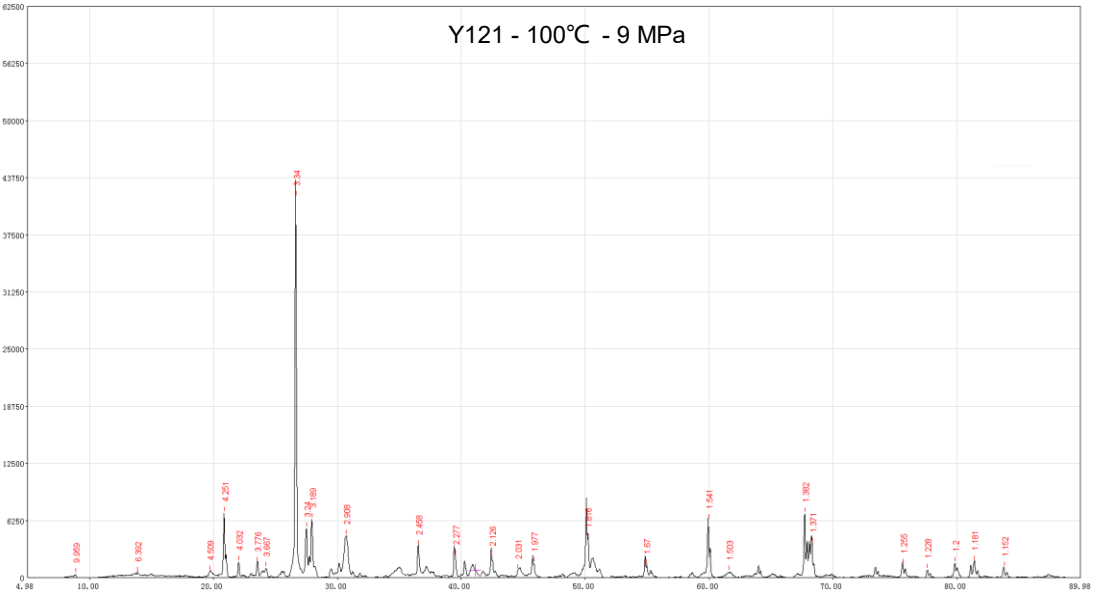
Y121 - 100℃ - 9 MPa

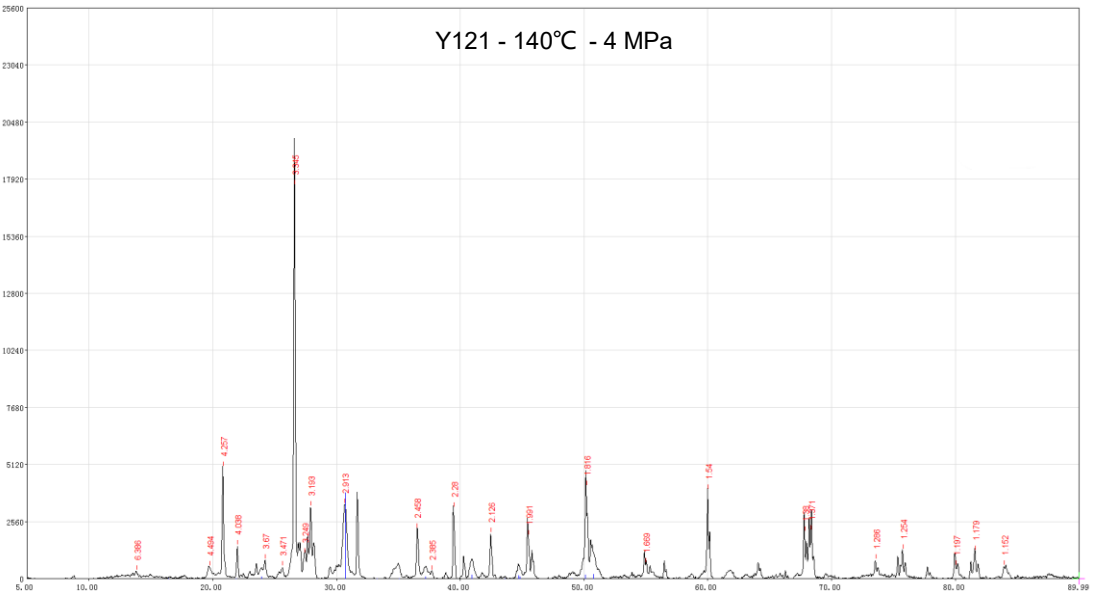
Y121 - 140℃ - 4 MPa

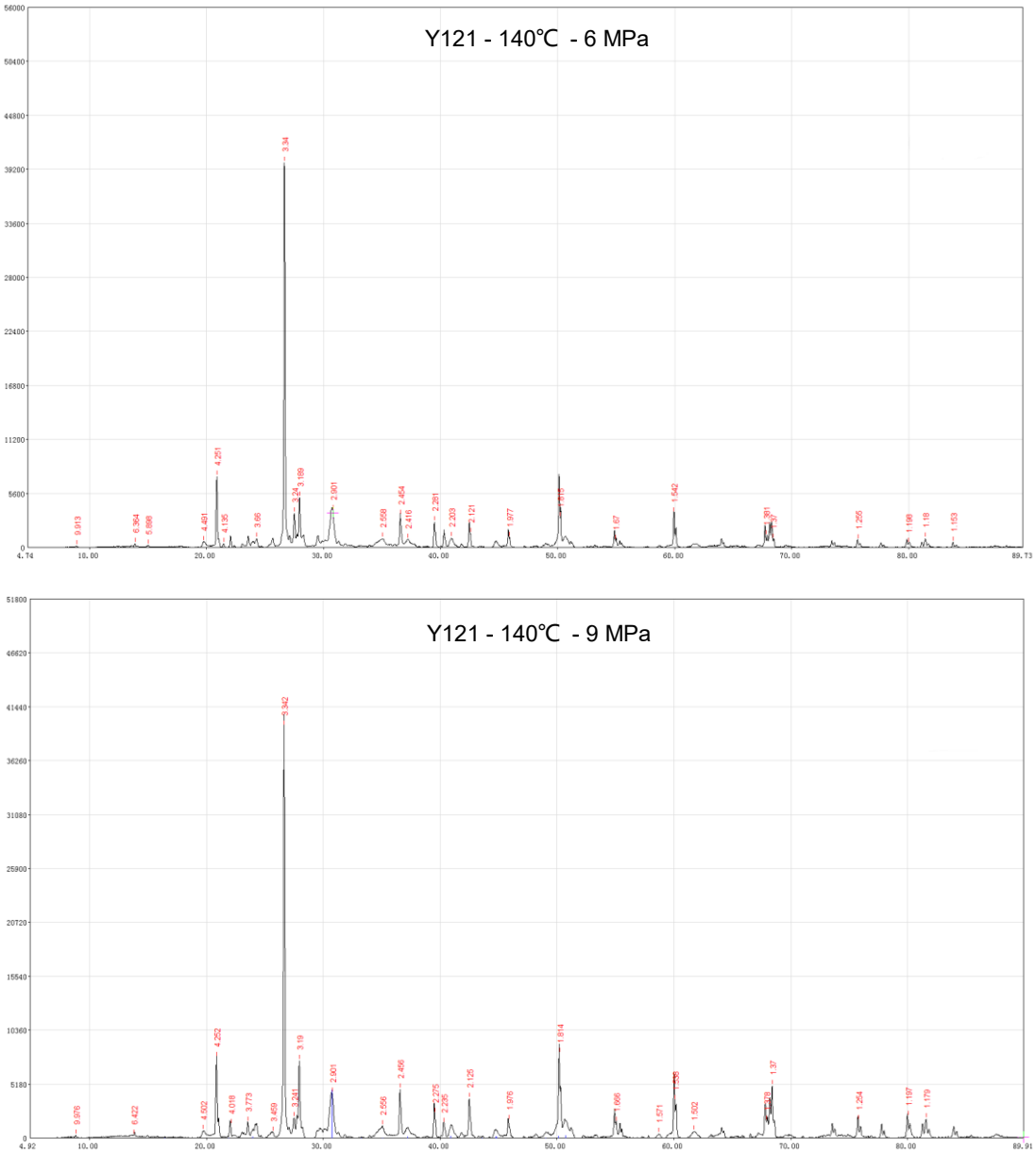

Figure 4 – *XRD Diffractograms for sample Y121*

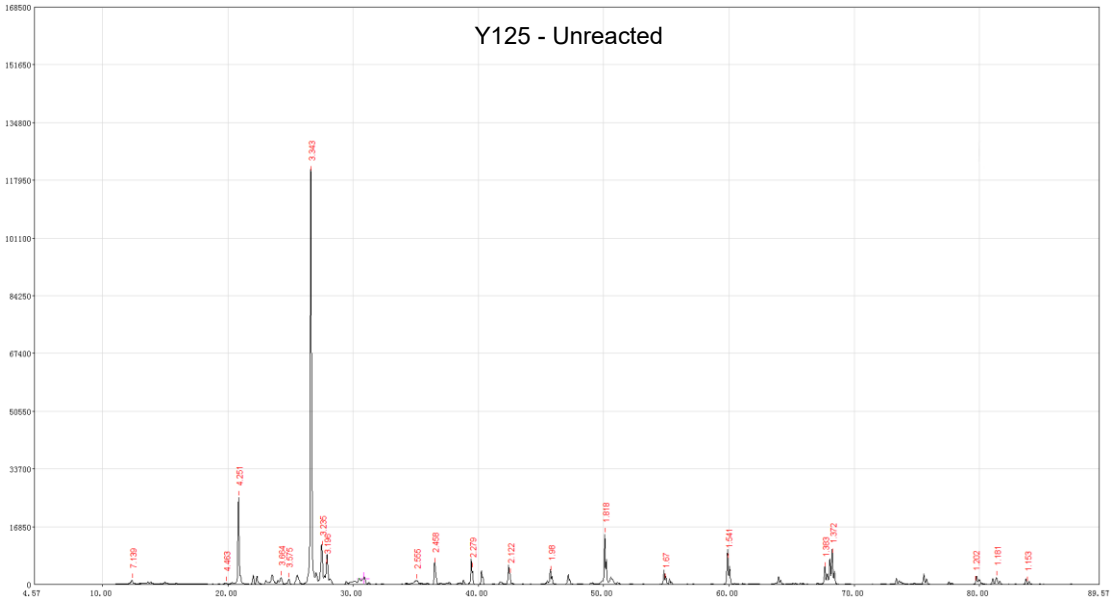
Y125 - Unreacted

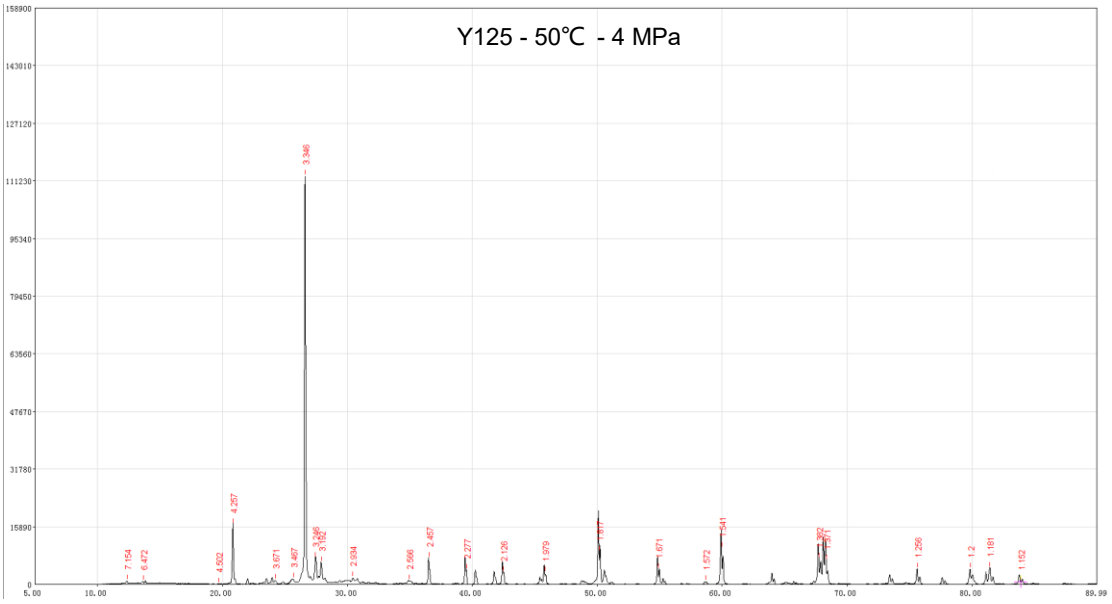
Y125 - 50℃ - 4 MPa

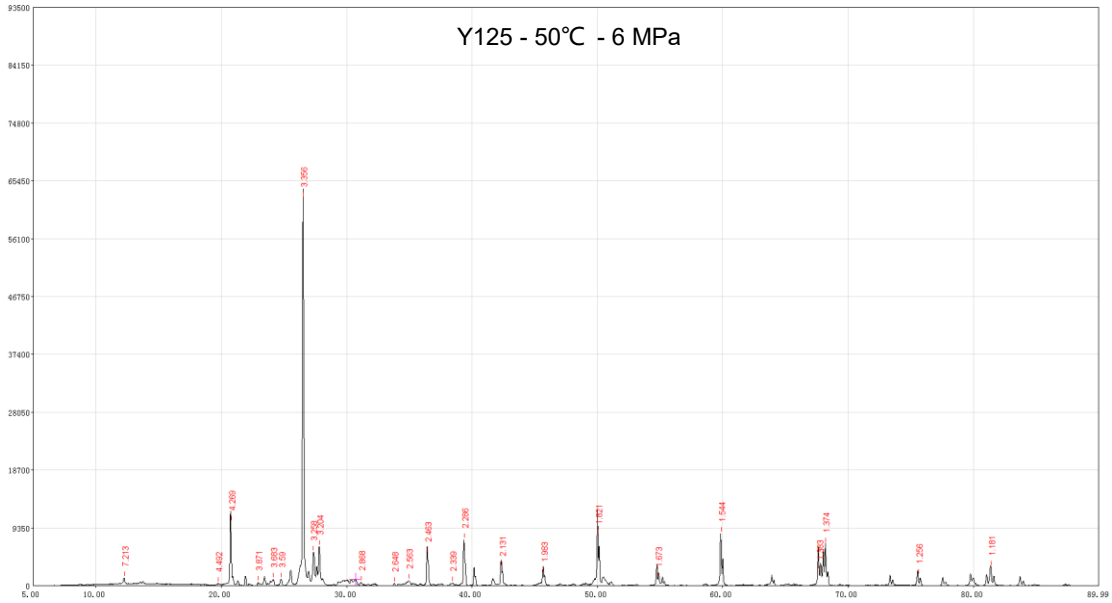
Y125 - 50℃ - 6 MPa

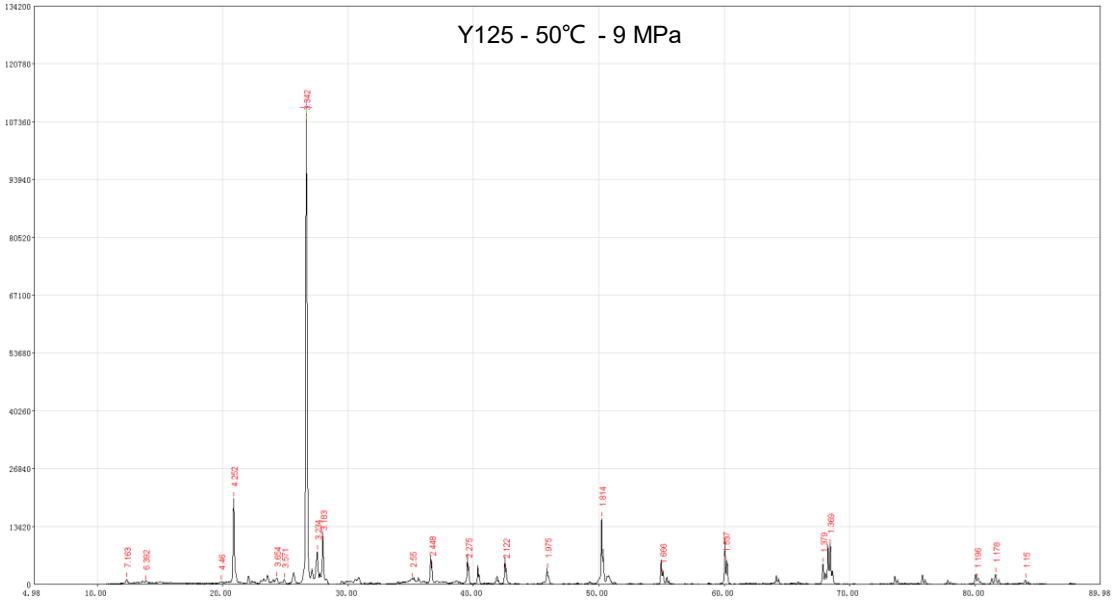
Y125 - 50℃ - 9 MPa

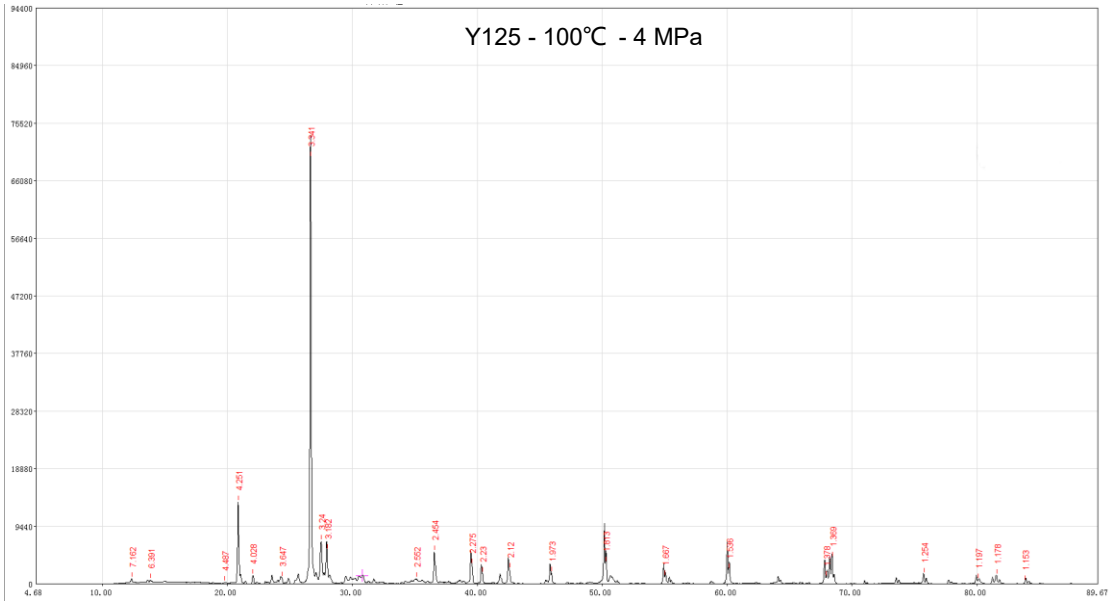
Y125 - 100℃ - 4 MPa

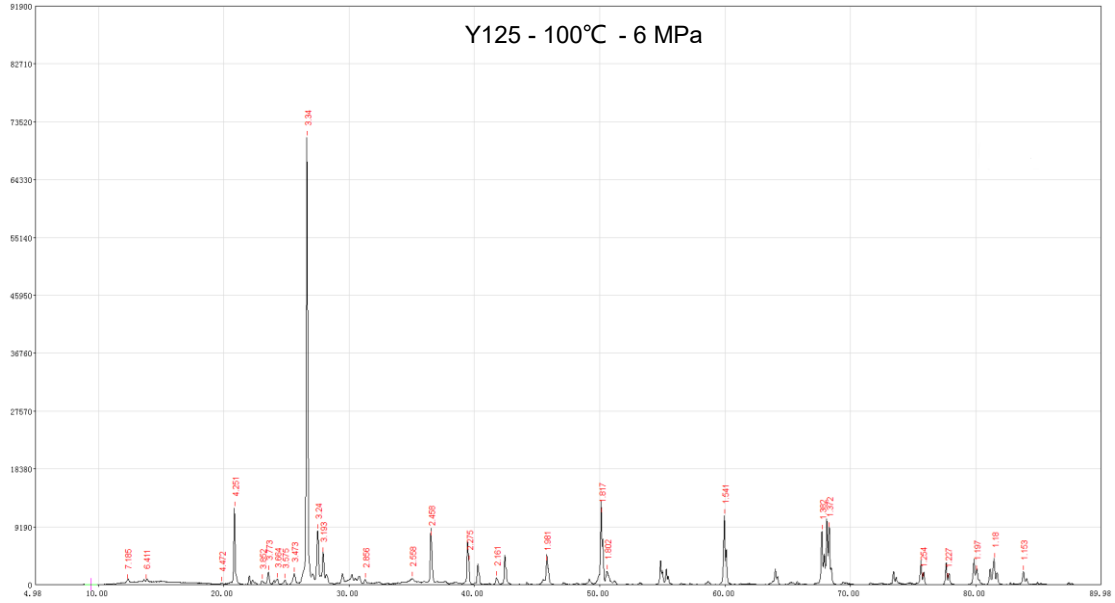
Y125 - 100℃ - 6 MPa

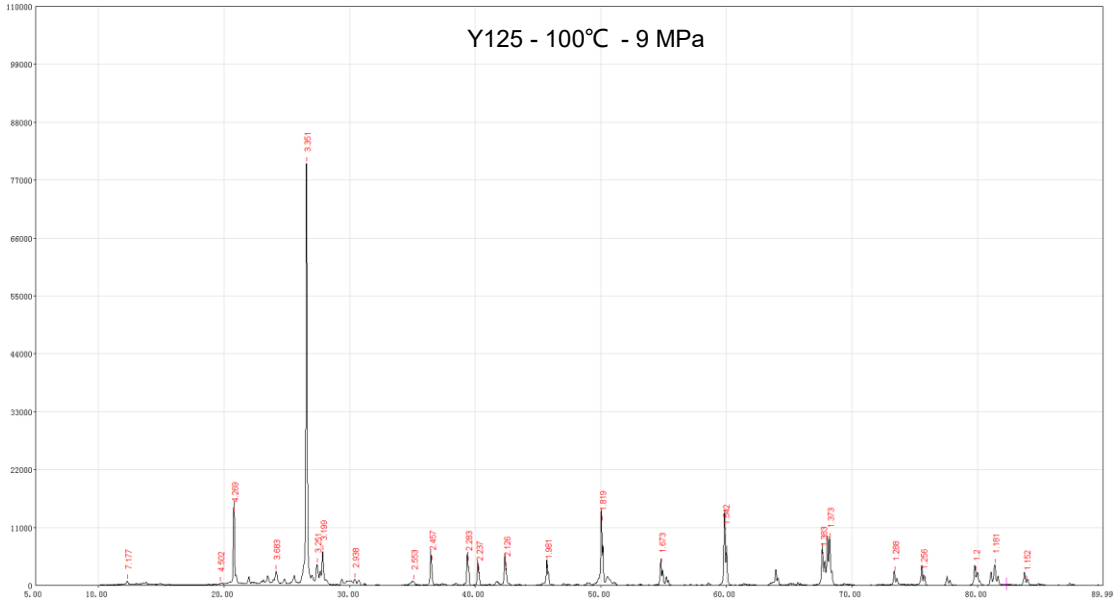
Y125 - 100℃ - 9 MPa

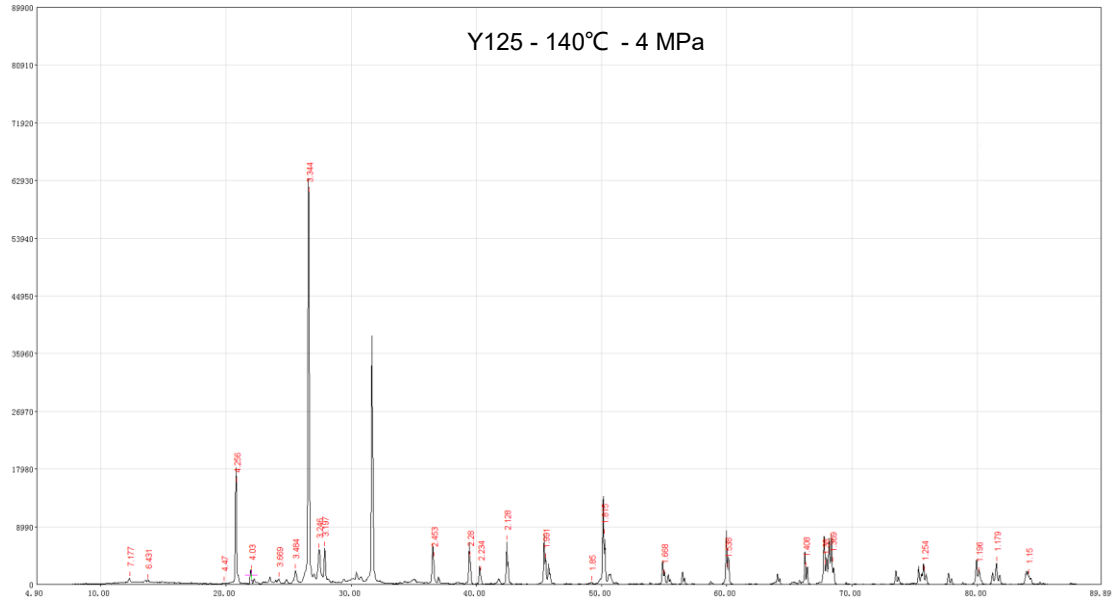
Y125 - 140℃ - 4 MPa

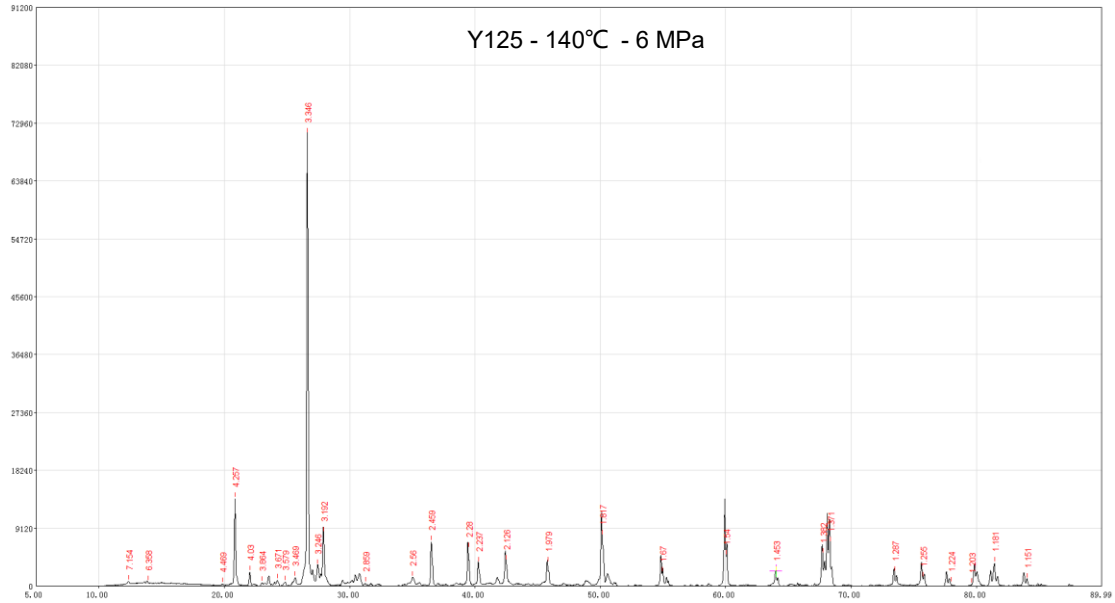
Y125 - 140℃ - 6 MPa

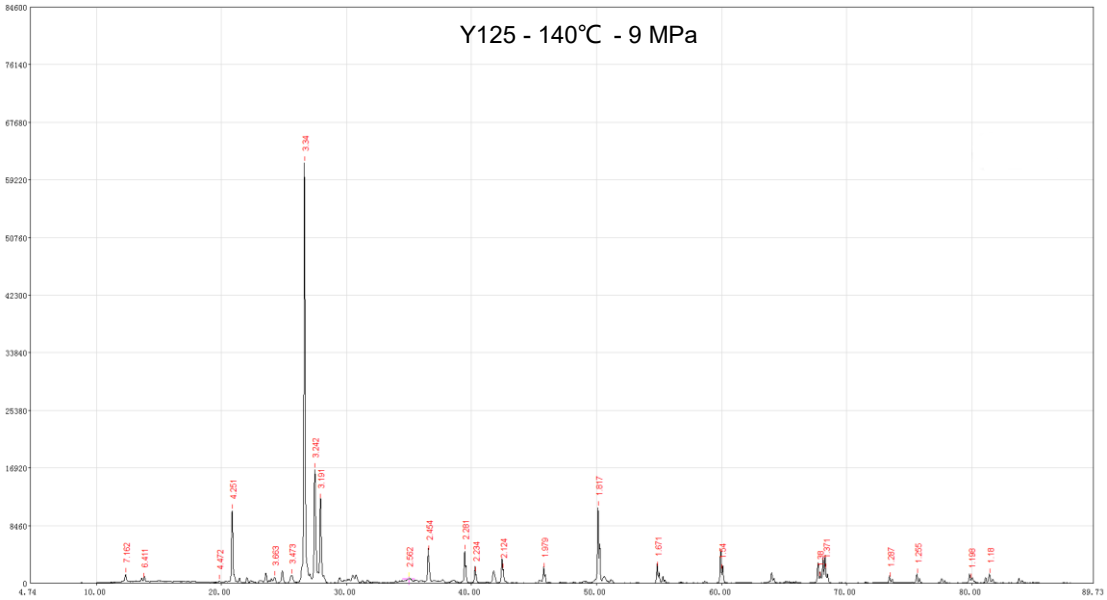

Figure 5 – *XRD Diffractograms for sample Y125*

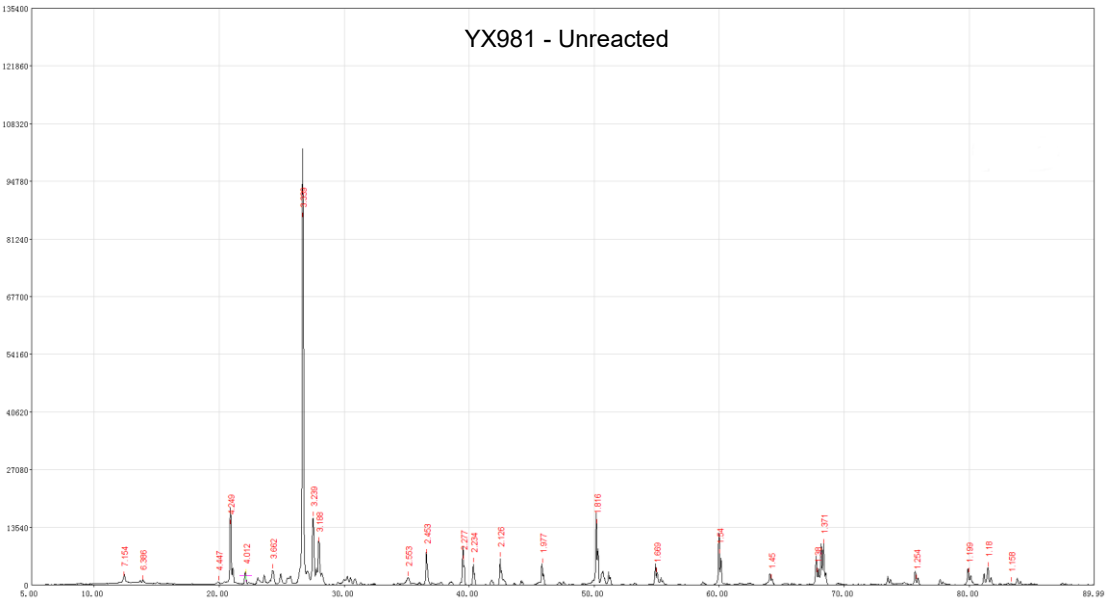

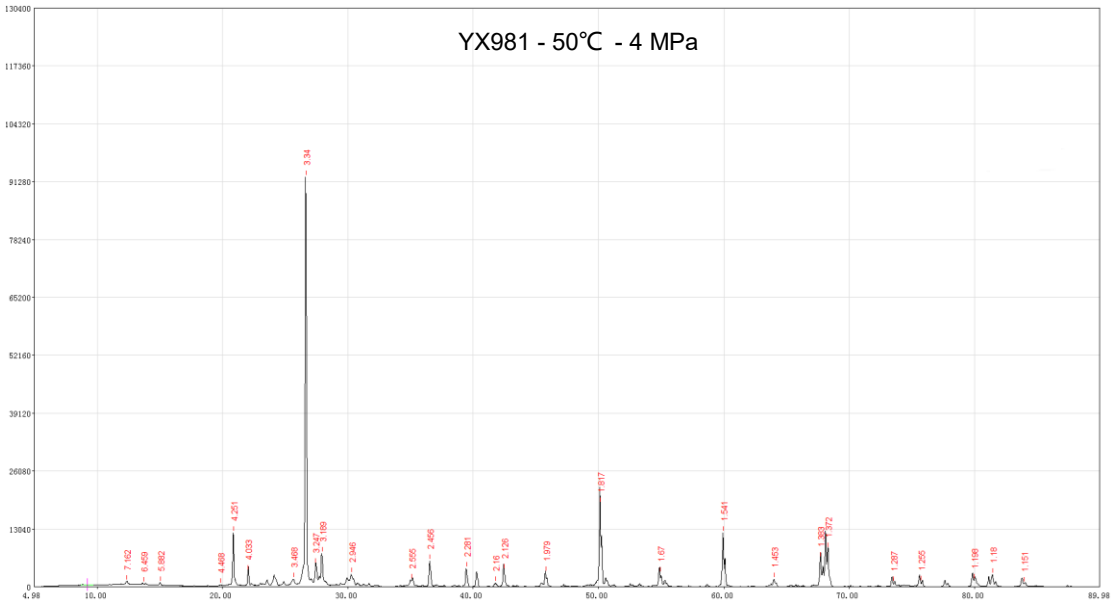
YX981 - 50℃ - 4 MPa

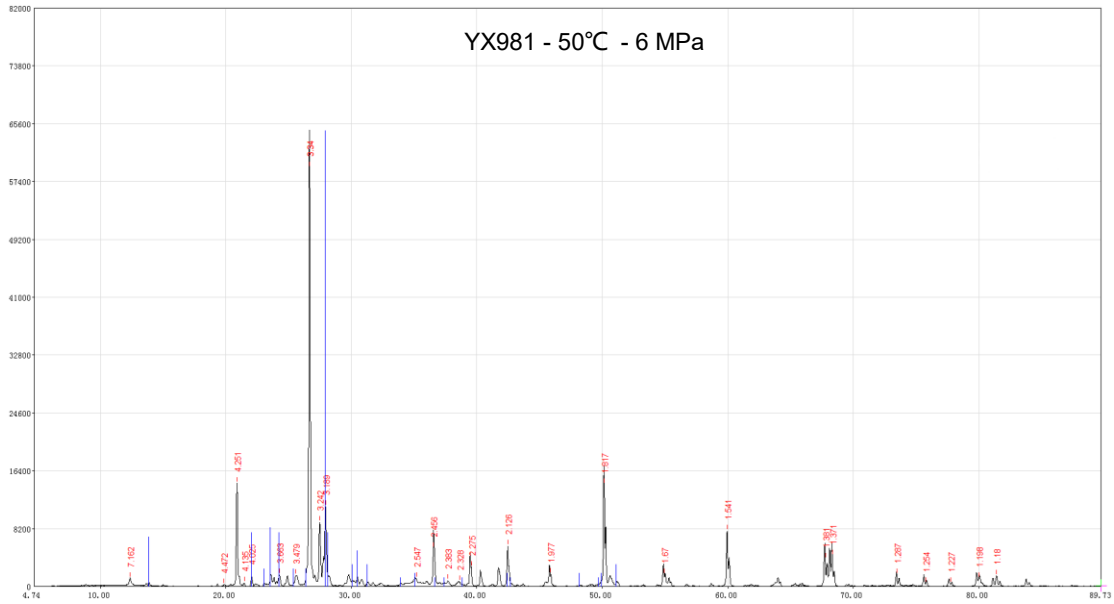
YX981 - 50℃ - 6 MPa

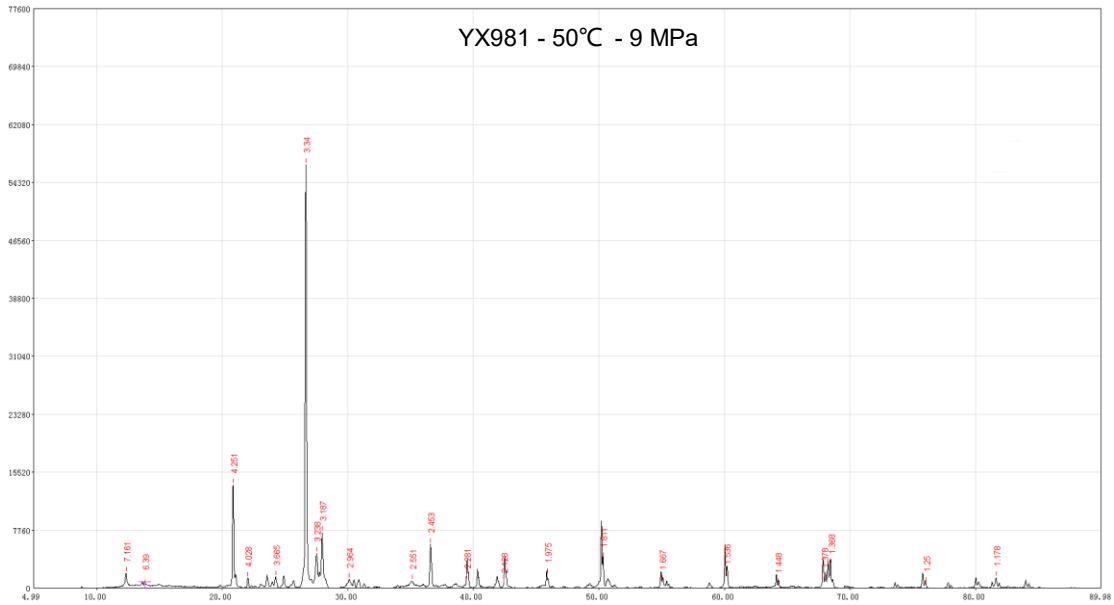
YX981 - 50℃ - 9 MPa

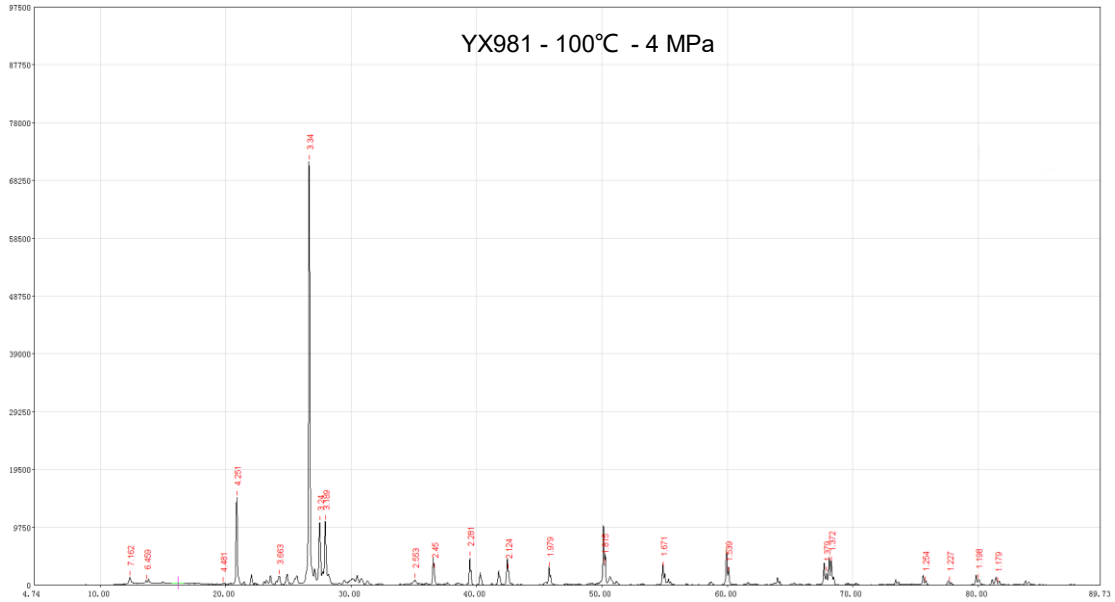
YX981 - 100℃ - 4 MPa

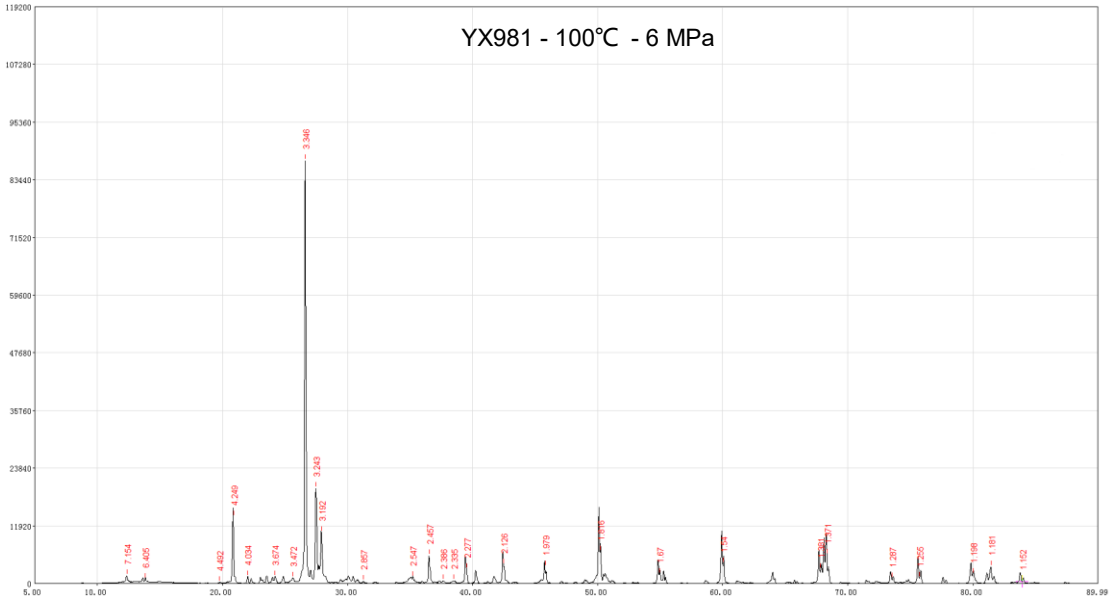
YX981 - 100℃ - 6 MPa

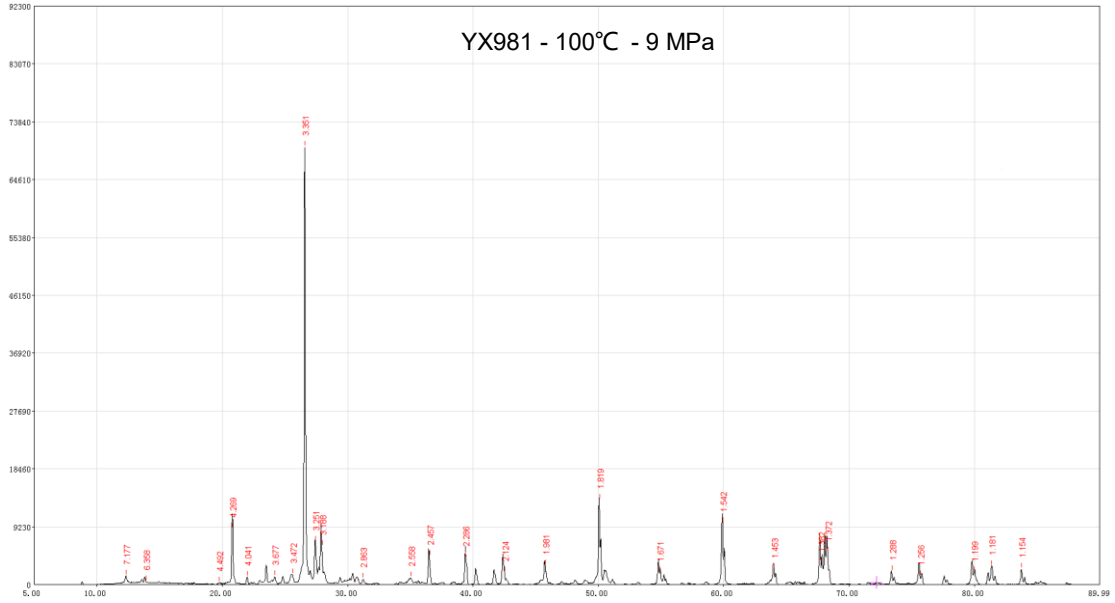
YX981 - 100℃ - 9 MPa

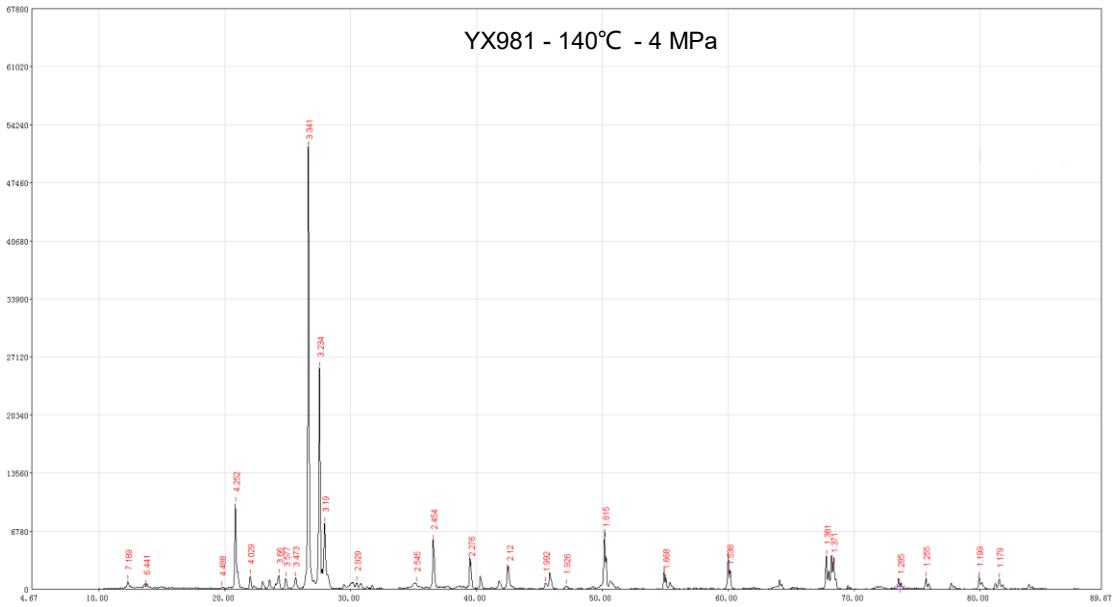
YX981 - 140℃ - 4 MPa

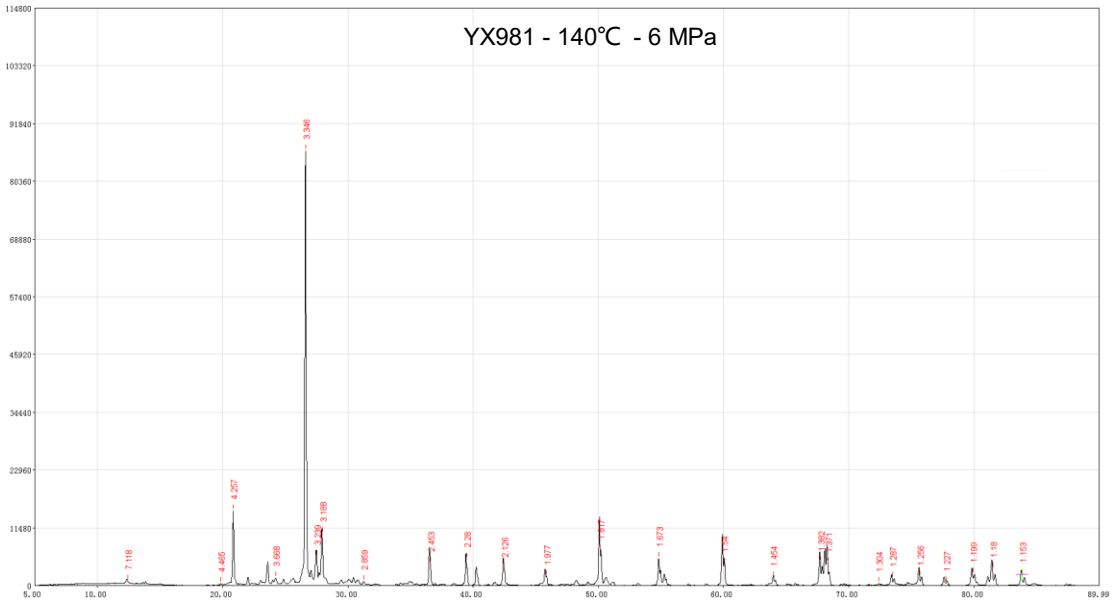
YX981 - 140℃ - 6 MPa

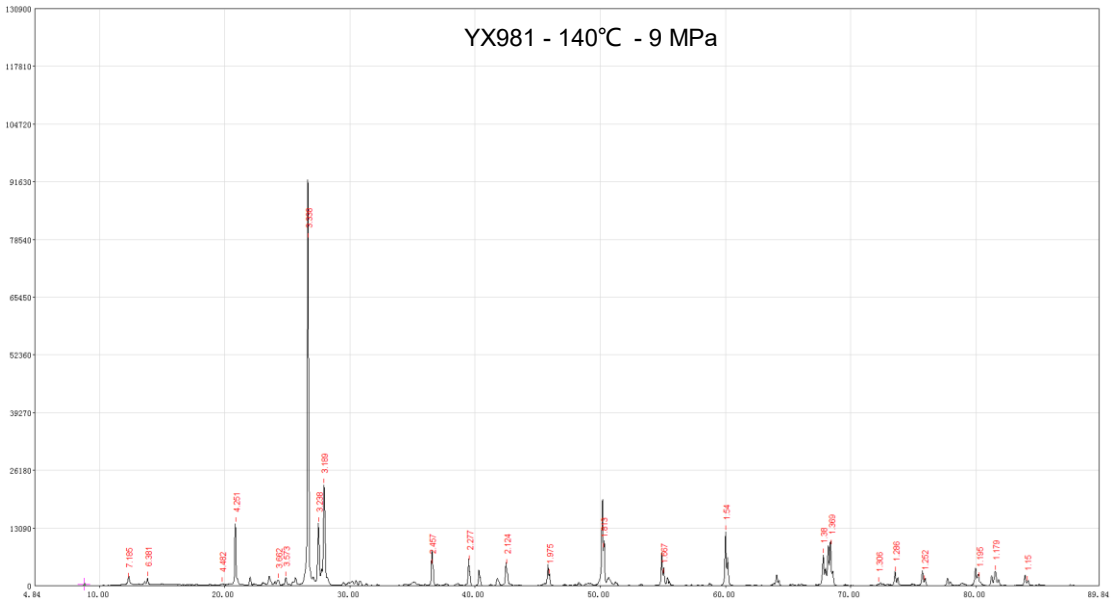
YX981 - 140℃ - 9 MPa

Figure 6 – *XRD Diffractograms for sample YX981*

Appendix B - TGA Curves

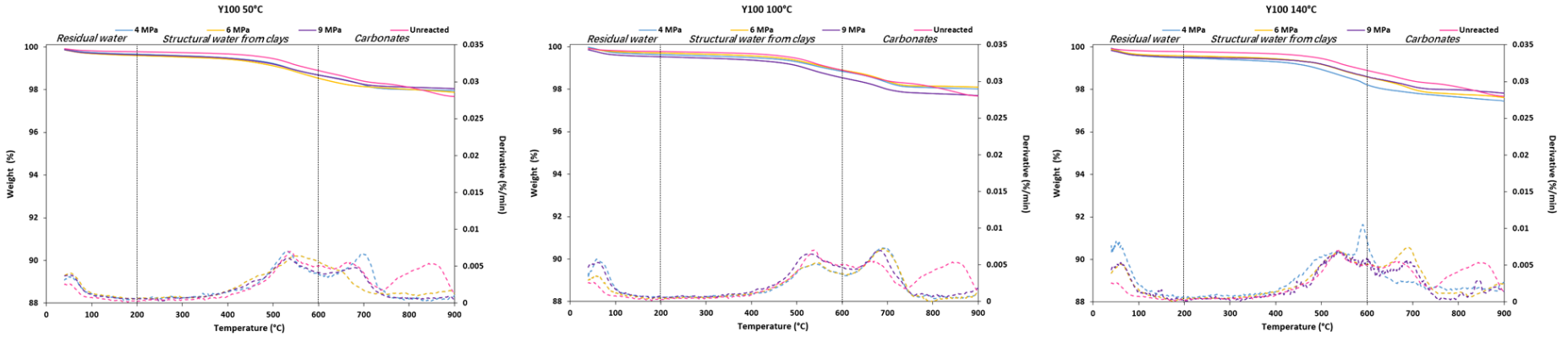

Figure 1 – *TGA curves for sample Y100*

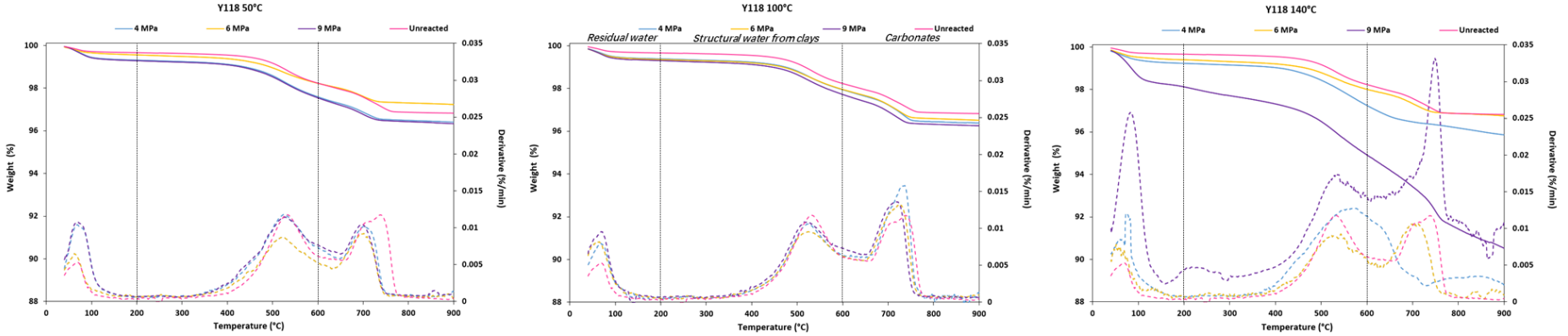

Figure 2 – *TGA curves for sample Y118*

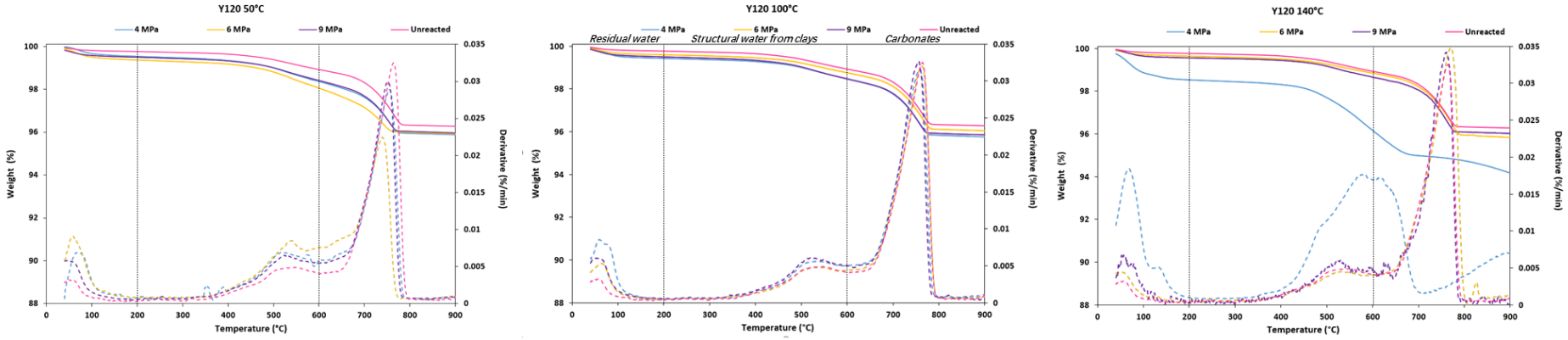

Figure 3 – *TGA curves for sample Y120*

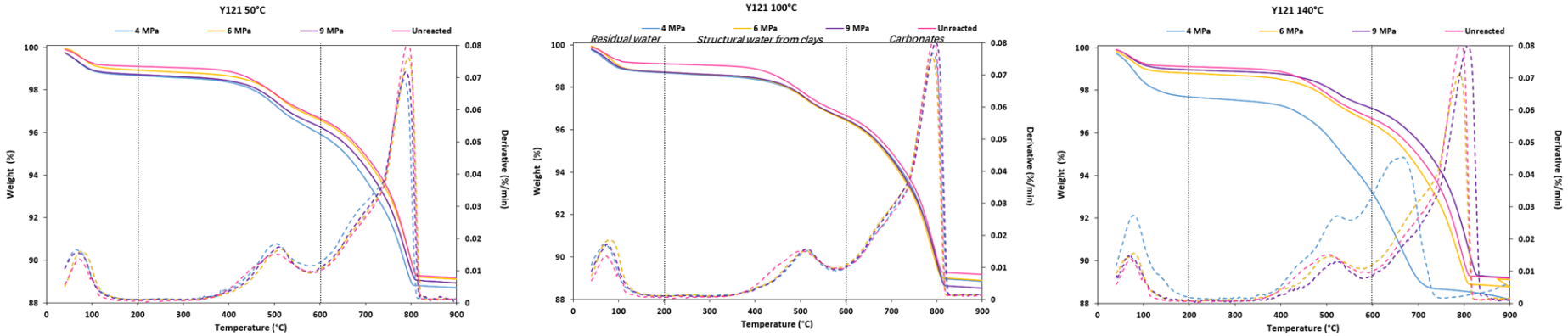

Figure 4 – *TGA curves for sample Y121*

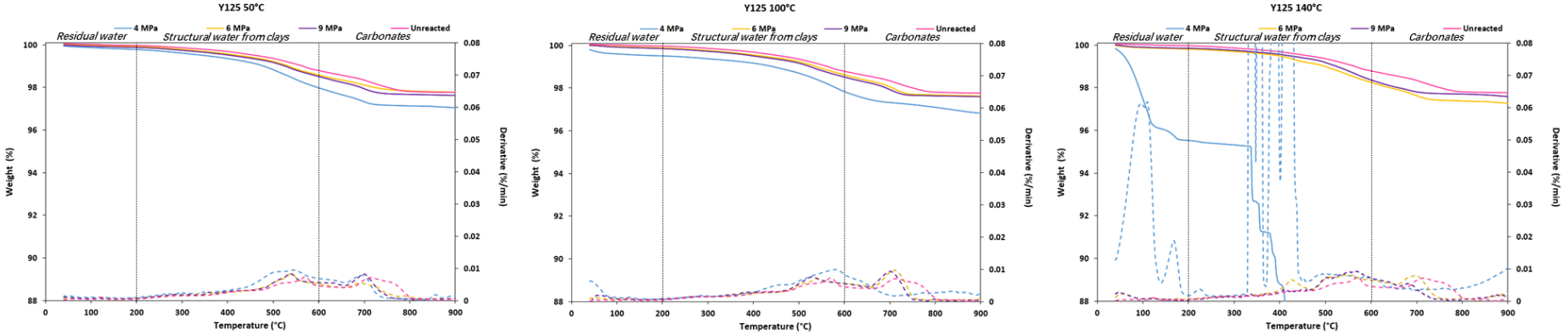

Figure 5 – *TGA curves for sample Y125*

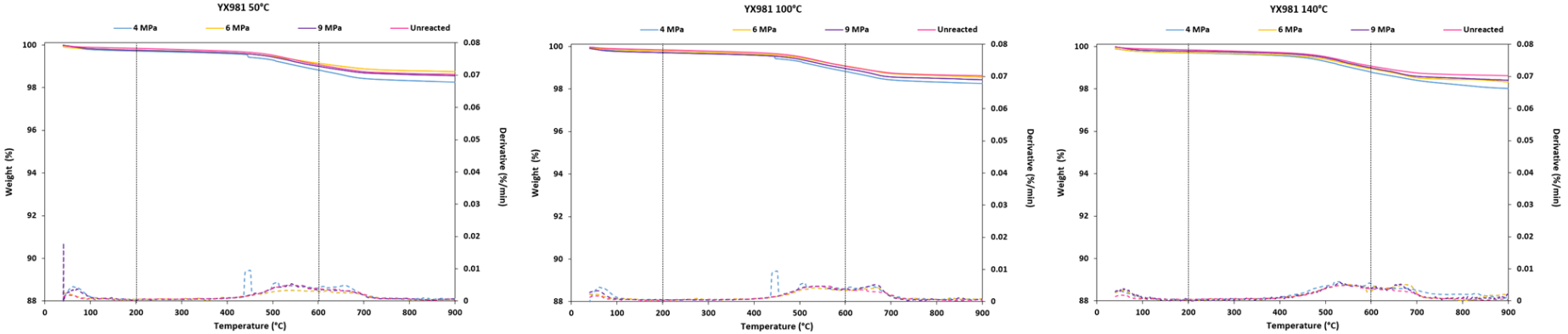

Figure 6 – *TGA curves for sample YX981*

References

Alia, B G., Emmanuelle, C., Louis-César, P., Jean-François Blais and Guy Mercier. (2015) CO2 sequestration using waste concrete and anorthosite tailings by direct mineral carbonation in gas-solid-liquid and gas-solid routes. Journal of Environmental Management, 163:70.

Aradóttir, E.S.P., Hólmfrídur Sigurdardóttir., Bergur Sigfússon and Einar Gunnlaugsson. (2011). Carbfix: a CCS pilot project imitating and accelerating natural CO2 sequestration. Greenhouse Gases Science & Technology, 1 (2), 105-118.

Arvidson, R. S., Ertan, I. E., Amonette, J. E., and Luttge, A. (2003). Variation in calcite dissolution rates: A fundamental problem? Geochimica et Cosmochimica Acta, 67, 1623-1634.

Barclay, S. A. , & Worden, R. H. . (2000). Geochemical modelling of diagenetic reactions in a sub-arkosic sandstone. Clay Minerals, 35(1), 57-68.

Bachu, S., Bonijoly, D., Bradshaw, J., Burruss, R., Holloway, S., Christensen, N. P. and Mathiassen, O. M. (2007). CO2 storage capacity estimation: Methodology and gaps. Int. J. Greenh. Gas Control, 1 (4), 430-443.

Bjørlykke, K., Nedkvitne, T, and Ramm, M. (1992). Diagenetic processes in the Brent Group (Middle Jurassic) reservoirs of the North Sea: an overview. Geological Society, London, Special Publications, 61(1), 263-287.

Cai, J. X. (1993). Temperature and pressure when calcite, dolomite and siderite react with CO_2 - dissolved aqueous solution. J Mineral Petrol, 13(2), 37-41. (in Chinese)

Celia, M. A. and Nordbotten, J. M. (2009). Practical modeling approaches for geological storage of carbon dioxide. Groundwater, 47 (5), 627-638.

Elmabrouk, S. K., Bader, H. E. and Mahmud, W M. (2017). An Overview of Power Plant CCS and CO_2-EOR Projects. International Conference on Industrial Engineering and Operations Management.

Eiken, O., Ringrose, P., Hermanrud, C., Nazarian, B., Torp, T.A., Høier, L. (2011). Lessons learned from 14 years of CCS operations: Sleipner, In Salah and Snøhvit. Energy Procedia, 4, 5541–5548.

Farquhar, S. M., Pearce, J. K., Dawson, G. K. W., Golab, A., Sommacal, S., Kirste, D., Biddle, D. and Golding, S. D. (2014). A fresh approach to investigating CO_2 storage: Experimental CO_2–water–rock interactions in a low-salinity reservoir system. Chemical Geology, https: //doi.org/10.1016/j.chemgeo.2014.10.006.

Gaus, I. (2010). Role and impact of CO_2-rock interactions during CO_2 storage in sedimentary rocks. Int. J. Greenh. Gas Control, 4 (1), 73-89.

Giles, M. R. , & Marshall, J. D. . (1986). Constraints on the development of secondary porosity in the subsurface: re-evaluation of processes. Marine & Petroleum Geology, 3(3), 243-255.

Giles, M. R. and De Boer, R. B. (1990). Origin and significance of redistributional secondary porosity. Marine and Petroleum Geology, 7 (4), 378-397.

Gilfillan, S. M., Lollar, B. S., Holland, G., Blagburn, D., Stevens, S., Schoell, M. and Ballentine, C. J. (2009). Solubility trapping in formation water as dominant CO2 sink in natural gas fields. Nature, 458 (7238), 614.

Gluyas, J.G. and Mathias, S.A. (2013) Geological storage of carbon dioxide (CO2), Geoscience, technologies, environmental aspects and legal frameworks, Woodhead Publishers ISBN 978-0-85709-427-8 (Print) 978-0-85709-727-9 (Online)

Gunter, W. D., Perkins, E. H. and Hutcheon, I. (2000). Aquifer disposal of acid gases: modelling of water-rock reactions for trapping of acid wastes. Applied Geochemistry, 15 (8), 1085-1095.

Guo, X., Liu, K., He, S., Song, G., Wang, Y., Hao, X. and Wang, B. (2012). Petroleum generation and charge history of the northern Dongying Depression, Bohai Bay Basin, China: insight from integrated fluid inclusion analysis and basin modelling. Marine and Petroleum Geology, 32 (1), 21-35.

Harouiya, N. and Oelkers, E. H. (2004). An experimental study of the effect of aqueous fluoride on quartz and alkali-feldspar dissolution rates. Chemical Geology, 205, 155-167.

He S., Lv, L., Liang, B., Li, C., Yuan, B., Ye, L. and Xie, H. (2015). Aqueous carbonation of the potassium-depleted residue from potassium feldspar–CaCl2 calcination for CO2 fixation. Environmental Earth Sciences, 73 (11), 6871-6879.

Hefferan, K. and O'Brien, J. (2010). Earth Materials. John Wiley & Sons.

Hellevang, H., Miri, R. and Haile, B. G. (2014). New Insights into the mechanisms controlling the rate of crystal growth. Crystal Growth & Design, 14 (12), 6451-6458.

Hitchon, B., Gunter, W. D., Gentzis, T. and Bailey, R. T. (1999). Sedimentary basins and greenhouse gases: a serendipitous association. Energy Conversion and Management, 40 (8), 825-843.

Jackson, R. B., Le Quéré, C., Andrew, R. M., Canadell, J. G., Peters, G. P., Roy, J. and Wu, L. (2017). Warning signs for stabilizing global CO2 emissions. Environmental Research Letters, 12 (11),

110202.

Jun, Y. S.; Giammar, D. E.; Werth, C. J. Impacts of geochemical reactions on geologic carbon sequestration. Environ. Sci. Technol. 2013, 47 (1), 3−8.

Kampman, N., Bickle, M., Becker, J., Assayag, N. and Chapman, H. (2009). Feldspar dissolution kinetics and Gibbs free energy dependence in a CO2-enriched groundwater system, Green River, Utah. Earth and Planetary Science Letters, 284, 473-488.

Kirsch, K., Navarre-Sitchler, A. K., Wunsch, A. and McCray, J. E. (2014). Metal release from sandstones under experimentally and numerically simulated CO2 leakage conditions. Environmental Science & Technology, 48 (3), 1436-1442.

Klett, T. R., Ahlbrandt, T. S., Schmoker, J. W. and Dolton, G. L. (1997). Ranking of the world's oil and gas provinces by known petroleum volumes. Center for Integrated Data Analytics Wisconsin Science Center.

Kumar, A., Shrivastava, J. P. and Pathak, V. (2017). Mineral carbonation reactions under water-saturated, hydrothermal-like conditions and numerical simulations of CO2 sequestration in tholeiitic basalt of the eastern deccan volcanic province, india. Applied Geochemistry, 84.

Leung, D. Y. C., Caramanna, G. and Marotovaler, M. M. (2014). An overview of current status of carbon dioxide capture and storage technologies. Renewable & Sustainable Energy Reviews, 39 (39), 426-443.

Li, F. and Li, W. (2017). Petrological record of CO2 influx in the Dongying Sag, Bohai Bay Basin, NE China. Applied Geochemistry, 84, 373-386.

Li, F., Cao, Y., Li, W. and Zhang, L. (2018). CO2 mineral trapping: Hydrothermal experimental assessments on the thermodynamic stability of dawsonite at 4.3 Mpa PCO2 and elevated temperatures. Greenhouse Gases: Science and Technology, 8 (1), 77-92.

Li, S. Z., Suo, Y. H., Santosh, M., Dai, L. M., Liu, X., Yu, S., Zhao, S. J., Jin, C. (2013). Mesozoic to Cenozoic intracontinental deformation and dynamics of the North China Craton. Geological Journal, 48: 543-560.

Li, W. F., Gao, Z. Z., Peng, D. T., Luo, S. S., He, Y. B. (2002). Sedimentary phases of the Shahejie Formation of Paleogene in Bonan Subsag, Shengli Oilfield. Sedimentary Geology and Tethyan Geology, 2, 24-30.(in Chinese)

Li, X., Wei, N., Liu, Y., Fang, Z., Dahowski, R. T. and Davidson, C. L. (2009). CO2 point emission and

geological storage capacity in China. Energy Procedia, 1 (1), 2793-2800.

Li, Y. and Pang, Z. (2016). Capacity and suitability assessment of deep saline aquifers for CO2 sequestration in the Bohai Bay Basin, East China. Environmental Earth Sciences, 75 (5), 402.

Li, Y., and Pang, Z. (2017). Hydrogeochemical characteristics of deep saline aquifers in sedimentary basins in China and implications for CO2 geological storage with emphasis on total dissolved solids (TDS) and water type. Greenhouse Gases: Science and Technology, 7 (1), 53-64.

Liu, H., Jiang, Y. L., Song, G. Q., Gu, G. C., Hao, L., Feng, Y. L. (2017). Overpressure characteristics and effects on hydrocarbon distribution in the Bonan Subsag, Bohai Bay Basin, China. Journal of Petroleum Science and Engineering, 149, 811-821.

Lu, P., Fu Q., Seyfried W. E. Jr., Hedges, S. W., Soong, Y., Jones, K., Zhu, C. (2013). Coupled alkali feldspar dissolution and secondary mineral precipitation in batch systems – 2: new experiments with supercritical CO2 and implications for carbon sequestration. Appl. Geochem. 30, 75–90.

Masters, C. D., Root, D. H. and Turner, R. M. (1998). World conventional crude oil and natural gas; identified reserves, undiscovered resources and futures (No. 98-468)

Matter, J. M. and Kelemen, P. B. (2009). Permanent storage of carbon dioxide in geological reservoirs by mineral carbonation. Nature Geoscience, 2 (12), 837.

McGrail, B. P., Schaef, H. T., Ho, A. M., Chien, Y. J., Dooley, J. J. and Davidson, C. L. (2006). Potential for carbon dioxide sequestration in flood basalts. Journal of Geophysical Research: Solid Earth, 111 (B12).

Miller, J. N. and Miller, J. C. (2010). Statistic and Chemometrics for Analytical Chemistry. Ashford Color Press.

Munz, I. A., Brandvoll, Ø., Haug, T. A., Iden, K., Smeets, R., Kihle, J. and Johansen, H. (2012). Mechanisms and rates of plagioclase carbonation reactions. Geochimica et Cosmochimica Acta, 77, 27-51.

Myer, L. (2011). Global status of geologic CO2 storage technology development. United States carbon sequestration council report July.

Olejnik, S., Algina, J. (2003). Generalized eta and omega squared statistics: measures of effect size for some common research designs. Psychol Methods, 8(4),434-447.

Pang, Z., Li, Y., Yang, F. and Duan, Z. (2012). Geochemistry of a continental saline aquifer for CO2 sequestration: The Guantao formation in the Bohai Bay Basin, North China. Applied Geochemistry,

27 (9), 1821-1828.

Peters, G. P., Le, Quéré C., Andrew, R. M., Canadell, J. G., Friedlingstein, P., Ilyina, T. and Sitch, S. (2017). Towards real-time verification of CO2 emissions. Nature Climate Change, 7 (12), 848.

Pokrovsky, O. S., Golubev, S. V. and Jacques, S. and Castillo, A. (2009). Calcite, dolomite and magnesite dissolution kinetics in aqueous solution at acid to circumneutral pH, 25 to 150 ℃ and 1 to 55 atm pCO2: New constraints on CO2 sequestration in sedimentary basins. Chemical Geology, 265 (1-1), 20-32.

Pokrovsky, O. S., Golubev, S. V. and Jordan, G. (2009). Effect of organic and inorganic ligands on calcite and magnesite dissolution rates at 60℃ and 30 atm PCO2. Chemical Geology, 265 (1-2), 33-43.

Shukla, R., Ranjith, P., Haque, A. and Choi, X. (2010). A review of studies on CO2 sequestration and caprock integrity. Fuel, 89 (10), 2651-2664.

Sorai, M., Ohsumi, T., Ishikawa, M., Tsukamoto, K. (2007). Feldspar dissolution rates measured using phase-shift interferometry: Implications to CO_2 underground sequestration. Applied Geochemistry, 22, 2795-2809.

Steefel, C.I., Appelo, C.A.J., Arora, B., Jacques, D., Kalbacher, T., Kolditz, O., Lagneau, V., Lichtner, P.C., Mayer, K.U., Meeussen, J.C.L., Molins, S., Moulton, D., Shao, H., Šimůnek, J., Spycher, N., Yabusaki, S.B., YEH, G.T. (2015) Reactive transport codes for subsurface environmental simulation. Computers & Geosciences, 19, 445-478

Steefel, C.I., Lasaga, A.C. (1994) A coupled model for transport of multiple chemical-species and kinetic precipitation dissolution reactions with application to reactive flow in single-phase hydrothermal systems, American Journal of Science, 294, 529-592.

Steefel, C. I.; Molins, S.; Trebotich, D. Pore Scale Processes Associated with Subsurface CO2 Injection and Sequestration. (2013). Rev. Mineral. Geochem, 77 (1), 259−303.

Steefel C. I., Beckingham L. E. and Landrot G. (2015) Micro continuum approaches for modeling pore-scale geochemical processes. Rev. Mineral. Geochem. 80(1), 217–246.

Stephens, M. A. (1974) EDF Statistics for Goodness of Fit and Some Comparisons. Journal of American Statistical Association, 69, 730-737.

Stevens, S. H., Kuuskraa, V. A., Gale, J. and Beecy, D. (2001). CO2 injection and sequestration in depleted oil and gas fields and deep coal seams: worldwide potential and costs. Environmental Geosciences, 8 (3), 200-209.

SY/T 5163-2018, Analysis method for clay minerals and ordinary non-clay minerals in sedimentary rocks by the X-ray diffraction, released by the National Energy Administration, China.

Tutolo, B. M. , Luhmann, A. J. , Kong, X. Z. , Saar, M. O. , & Seyfried, W. E. . (2015). CO2 sequestration in feldspar-rich sandstone. Agu Fall Meeting. AGU Fall Meeting Abstracts.Van der Zwaan, B. and Smekens, K. (2009). CO2 capture and storage with leakage in an energy-climate model. Environmental Modeling & Assessment, 14 (2), 135-148.

Van Pham, T. H., Aagaard, P. and Hellevang, H. (2012). On the potential for CO2 mineral storage in continental flood basalts-phreeqc batch- and 1d diffusion-reaction simulations. Geochem Trans, 13 (1), 5.

Wang, D. M., Xu, Y. M., He, D. M., Guan, J., Zhang, O. M. (2009) Investigation of mineral composition of oil shale. Asia-Pacific Journal of Chemical Engineering, 4(5): 691-697.

Wang, M. , Wilkins, R. W. T. , Song, G. , Zhang, L. , Xu, X. , & Li, Z. , et al. (2015). Geochemical and geological characteristics of the es3l lacustrine shale in the Bonan Subsag, bohai bay basin, china. International Journal of Coal Geology, 138, 16-29.

Wang, T. Y., Wang, H. Y., Zhang, F. J., Xu, T. F. (2013) Simulation of CO2–water–rock interactions on geologic CO2 sequestration under geological conditions of China. Marine Pollution Bulletin, 76, 307-314.

Wang, Y. Z. (2010). Genetic mechanism and evolution model of secondary pore development zone of Paleogene in the north zone in Dongying Depression. Qingdao: China University of Petroleum (Huadong). (in Chinese with English abstract)

Wang, Y. Z., Zan, N. M., Cao, X., Cao, Y. C., Yuan, G. H., Gluyas, J., Lin, M. R. Geologic CO2 storage in arkosic sandstones with CaCl2-rich formation water, Chemical Geology (2018), https://doi.org/10.1016/j.chemgeo.2020.119867.

Wolff-Boenisch, D. and Galeczka, I. M. (2018). Flow-through reactor experiments on basalt-(sea) water-CO2 reactions at 90℃ and neutral pH. What happens to the basalt pore space under post-injection conditions?. Int. J. Greenh. Gas Control, 68, 176-190.

Wigand, M., Carey, J. W., Schütt, H., Spangenberg, E. and Erzinger, J. (2008). Geochemical effects of CO2 sequestration in sandstones under simulated in situ conditions of deep saline aquifers. Applied Geochemistry, 23 (9), 2735-2745.

Xu, R. N., Li, R., Ma, J., He, D., Jiang, P. X. (2017). Effect of Mineral Dissolution/Precipitation and CO2

Exsolution on CO2 transport in Geological Carbon Storage. Accounts of Chemical Research, 50 (9), 2056-2066.

Xu, T., Apps, J. A. and Pruess, K. (2005). Mineral sequestration of carbon dioxide in a sandstone–shale system. Chemical Geology, 217, 295-318.

Xu, T., Apps, J. A. and Pruess, K. (2004). Numerical simulation of co disposal by mineral trapping in deep aquifers. Applied Geochemistry, 19 (6), 917-936.

Yang, F., Bai, B., Tang, D., Shari, D. N. and David, W. (2010). Characteristics of CO2 sequestration in saline aquifers. Petroleum Science, 7 (1), 83-92.

Yu, Z., Liu, K., Liu, L., Yang, S. and Yang, Y. (2017). An experimental study of CO2-oil-brine-rock interaction under in situ reservoir conditions. Geochemistry, Geophysics, Geosystems, 18 (7), 2526-2542.

Yu, Z., Liu, L., Liu, K., Yang, S. and Yang, Y. (2015). Petrological characterization and reactive transport simulation of a high-water-cut oil reservoir in the Southern Songliao Basin, Eastern China for CO2 sequestration. Int. J. Greenh. Gas Control, 37, 191-212.

Yuan, G. H., Cao, Y. C., Gluyas, J., Li, X., Xi, K. L., Wang, Y. Z. and Oxtoby, N. H. (2015a). Feldspar dissolution, authigenic clays, and quartz cements in open and closed sandstone geochemical systems during diagenesis: Typical examples from two sags in Bohai Bay Basin, East China. AAPG Bulletin, 99 (11), 2121-2154.

Yuan, G. H., Cao, Y. C., Gluyas, J., Cao, X. and Zhang, W. (2017a). Petrography, fluid inclusion, isotope and trace element constraints on the origin of quartz cementation and feldspar dissolution and the associated fluid evolution in arkosic sandstones. AAPG Bulletin, (20, 170,615).

Yuan, G. H., Cao, Y. C., Jia, Z. Z., Gluyas, J., Yang, T., Wang, Y. Z. and Xi, K. L. (2015b). Selective dissolution of feldspars in the presence of carbonates: The way to generate secondary pores in buried sandstones by organic CO2. Marine and Petroleum Geology, 60, 105-119.

Yuan, G. H., Gluyas, J., Cao, Y. C, Oxtoby, N. H., Jia, Z. Z., Wang, Y. Z. and Li, X. (2015c). Diagenesis and reservoir quality evolution of the Eocene sandstones in the northern Dongying Sag, Bohai Bay Basin, East China. Marine and Petroleum Geology, 62, 77-89.

Yuan, Guanghui, Jia, Zhenzhen, Cao, & Yingchang, et al. (2017). Reactive transport modeling of coupled feldspar dissolution and secondary mineral precipitation and its implication for diagenetic interaction in sandstones. Geochimica et Cosmochimica Acta: Journal of the Geochemical Society

and the Meteoritical Society, 207, 232-255.

Zeng, L. , Lyu, W. , Li, J. , Guo, Y. , & Zu, K. . (2019). Variation in the orientation of the maximum horizontal stress in thick channel-fill sandstones with low-permeability: a case of the bonan oilfield in the bohai bay basin, eastern china. Marine and Petroleum Geology, 107, 32-40.

Zhu, C. , & Lu, P. . (2009). Alkali feldspar dissolution and secondary mineral precipitation in batch systems: 3. saturation states of product minerals and reaction paths. Geochimica Et Cosmochimica Acta, 73(11), 3171-3200.